DIPLOMARBEIT

Comparison of Tropospheric Delay Modeling Approaches in VLBI Analysis

zur Erlangung des akademischen Grades

Diplom-Ingenieur

ausgeführt am Department für

Geodäsie und Geoinformation

Forschungsbereich Höhere Geodäsie

der Technischen Universität Wien

unter Anleitung von

Univ.Prof. Dipl.-Ing. Dr.techn. Johannes Böhm

und

Assistant Prof. Dipl.-Ing.in Dr.in techn. Hana Krásná

durch

Leo Baldreich, BSc

Matrikelnummer: 11702330

Wien, im Mai 2024

Unterschrift (Verfasser) Unterschrift (Betreuer/in)

Eidesstattliche Erklärung

Ich erkläre an Eides statt, dass die vorliegende Arbeit nach den anerkannten Grundsätzen für wissenschaftliche Abhandlungen von mir selbstständig erstellt wurde. Alle verwendeten Hilfsmittel, insbesondere die zugrunde gelegte Literatur, sind in dieser Arbeit genannt und aufgelistet. Die aus den Quellen wörtlich entnommenen Stellen, sind als solche kenntlich gemacht.

Das Thema dieser Arbeit wurde von mir bisher weder im In- noch Ausland einer Beurteilerin/einem Beurteiler zur Begutachtung in irgendeiner Form als Prüfungsarbeit vorgelegt. Diese Arbeit stimmt mit der von den Begutachterinnen/Begutachtern beurteilten Arbeit überein.

Wien, im Mai 2024 _____

Abstract

In VLBI analysis, the tropospheric signal delay is modeled using so-called mapping functions and gradients. They relate a delay in zenith direction to the delay at the elevation and azimuth at which an observation takes place. The objective of this thesis is to investigate how different settings for modeling of the tropospheric delays and for the estimation of tropospheric parameters in the Vienna VLBI and Satellite Software (VieVS) affect the results of VLBI analysis. To do this, 3296 legacy S/X sessions from 2000 until 2020 and 36 VGOS sessions from 2017, 2019 and 2020 are analyzed. A main focus of investigation are baseline length repeatabilities (BLRs), which serve as a good measure of the accuracy achievable with a specific setting.

The first part of the thesis deals with testing different choices of mapping functions for the hydrostatic and wet delays. It is found that the differences between any combination of the Vienna Mapping Functions (VMF1 and VMF3) are negligible when comparing baseline length repeatabilities. However, it is further revealed that using VMF3 for the hydrostatic and VMF1 for the wet delay component will introduce a bias to the estimated stations heights of about one to two millimeters height decrease on average, compared to either using VMF1 or VMF3 consistently for both delay components. This result is important because this inconsistent approach was used as default by the Vienna Analysis Center at the start of this investigation. A section of the thesis is then dedicated to the differences between VMF1 and VMF3 which give rise to this bias in a mixed application.

In the second part, the influence of the estimation intervals for zenith wet delays and gradients on baseline length repeatabilities is investigated. A small influence is observed. Here, shorter estimation intervals improved average baseline length repeatabilities for S/X sessions, while longer intervals did so for VGOS sessions.

Kurzfassung

In der VLBI-Analyse werden troposphärische Lauftzeitverzögerungen mit Mappingfunktionen und Gradienten modelliert. Sie stellen den Zusammenhang her zwischen der Verzögerung in Zenitrichtung und der Verzögerung bei der Elevation und dem Azimut bei dem eine Beobachtung stattfindet. Ziel dieser Arbeit ist, zu untersuchen wie sich verschiedene Einstellungen für die Modellierung und Parametrisierung der Troposphäre, die das Program *Vienna VLBI and Satellite Software* (VieVS) zur Verfügung stellt, auf die Ergebnisse der VLBI-Analyse auswirken. Hierzu werden 3296 S/X-Experimente aus den Jahren 2000 bis 2020 und 36 VGOS-Experimente aus 2017, 2019 und 2020 analysiert. Ein besonderes Augenmerk wird dabei auf die Wiederholbarkeiten der Basislinienlängen gelegt, die einen guten Maßstab für die Genauigkeit, die mit einer bestimmten Einstellungswahl erreicht werden kann, bildet.

Der erste Teil der Arbeit behandelt dabei veschiedene Möglichkeiten, Mappinfunktionen für die hydrostatische und die feuchte Lauftzeitverzögerung festzulegen. Es stellt sich heraus, dass bezogen auf die Wiederholbarkeit der Basislinienlängen, zwischen jeder möglichen Kombination der *Vienna Mapping Functions* (VMF1 und VMF3) nur vernachlässigbare Unterschiede bestehen. Jedoch ergab sich auch, dass wenn man für die hydrostatische Lauftzeitverzögerung VMF1 und für die feuchte Verzögerung VMF3 verwendet, Stationshöhen im Durchschnitt um zirka ein bis zwei Millimeter geringer geschätzt werden als in einer Analyse bei der VMF1 oder VMF3 konsistent für beide Laufzeitverzögerungen verwendet werden. Die Bedeutung dieses Ergebnisses ergibt sich daraus, dass diese inkonsistente Anwendung zu Beginn der Untersuchung als Standard am Vienna Analysis Center in Gebrauch war. Ein Abschnitt der Arbeit ist dann den Unterschieden zwischen VMF1 und VMF3 gewidmet, die diese Verzerrung bei gemischter Anwendung verursachen.

Im zweiten Teil wird der Einfluss der Schätzintervalle für die feuchten Lauftzeitverzögerungen in Zenitrichtung und Gradienten auf die Wiederholbarkeiten der Baslinienlängen untersucht. Dabei wird ein kleiner Einfluss beobachtet, der bei S/X-Experimenten zu einer durchschnittlichen Verbesserung der Wiederholbarkeiten bei kürzeren Schätzintervallen führt. Bei VGOS-Experimenten hingegen führen längere Schätzintervalle zu einer Verbesserung.

Contents

1 Introduction

Very Long Baseline Interferometry (VLBI) is one of the four space geodetic techniques, with the others being Global Navigation Satellite Systems (GNSS), Satellite Laser Ranging (SLR) and Doppler Orbitography and Radiopositioning Integrated by Satellite (DORIS). These techniques are used to gain information about the Earth's shape, rotation and gravity, and about the change of these parameters with time, as well as to create global reference frames to assign coordinates to points on Earth. A common feature of all space geodetic techniques is their dependence on electromagnetic radiation traversing the atmosphere, be it optical as in SLR or in the microwave/radio range as for the other techniques. To ensure accuracy, this necessitates understanding and modeling how the atmosphere affects the radiation. Hereby, two parts of the atmosphere show different behaviors: the ionosphere and the neutral atmosphere. The focus of this thesis lies on the modeling and parametrization of the neutral atmosphere's influence. In a slight simplification, the neutral atmosphere will often be referred to as the *troposphere*, which is technically only the name of a part (albeit the most important) of the former.

In the case of VLBI, the radiation is produced by extra-galactic radio sources (which incidentally makes it the only one of these techniques to not use a man-made radiation source), and observed by radio telescopes all over the world. What also sets geodetic VLBI apart from the other techniques is its ability to be used for the realization of the International Celestial Reference Frame (ICRF) as well as for the estimation of the full set of Earth Orientation Parameters (EOP). These parameters represent the transformation between the ICRF and the International Terrestrial Reference Frame (ITRF), whose realization is also one of the most important objectives of geodetic VLBI. Additionally, apart from geodetic or astrometric VLBI, the technique is also an important tool in astronomy.

In geodetic VLBI, two or more telescopes observe the same radio source simultaneously, and the difference of the radiation's arrival time (delay) at the telescopes is the observed quantity. As these delays will be influenced by the troposphere, tropospheric influence must be modeled a priori or introduced as additional parameters to estimate in the analysis. Current VLBI analysis usually does both, as some tropospheric parameters can be modeled with high accuracy, while others cannot. Objective of this thesis was to find out if and how different approaches to model and parameterize the troposphere affect the accuracy of VLBI analysis. Two different topics were in the focus of the investigation. First, the choice of the underlying a priori models themselves (in the form of so-called *mapping functions*), and second the time resolution at which the unmodeled parameters are estimated. This investi-

gation is also important to ensure the quality of the analysis performed at the Vienna Analysis Center for VLBI.

The first two chapters of this thesis are dedicated to giving an overview of VLBI in general, and about the tropospheric effects to consider. Different approaches to create mapping functions are explained, most importantly the *Vienna Mapping Functions* VMF1 and VMF3 developed at TU Wien.

In the next chapter, different choices of these mapping functions to model tropospheric delays in VLBI analysis are compared w. r. t. their influence on baseline length repeatabilities (BLRs) as a measure of the achievable accuracy. Another important focus lies on possible systematic effects on parameter estimation, especially station height coordinates.

Following on that, the same analysis of baseline length repeatabilities is performed to asses different estimation intervals of the three tropospheric parameters customarily estimated per station in VLBI analysis (zenith wet delays, east and north gradients). A similar investigation over a wider range of intervals and constraints, but for VGOS sessions only has been performed by Mikschi et al. (2021). The thesis concludes with an overview of the obtained results and a possible outlook for further research.

2 Very Long Baseline Interferometry

Very Long Baseline Interferometry (VLBI) began in the 1960s as a technique for radio astronomy. By synthesizing a telescope aperture of thousands of kilometers, the imaging of extra-galactic objects could be done with vastly improved angular resolution. Later, applications of VLBI for geodetic and astrometric purposes followed (Nothnagel, 2019). Today, VLBI is an important space geodetic technique for realizing the International Celestial Reference Frame (ICRF) and contributing to the International Terrestrial Reference Frame (ITRF). What sets apart VLBI from other space geodetic techniques, such as Satellite Laser Ranging (SLR) or Global Navigation Satellite Systems (GNSS), is that it is the only technique able to provide all five Earth Orientation Parameters (EOP) (Schuh and Böhm, 2013). These parameters (dUT1, two pole coordinates, two celestial pole offsets) describe the transformation between the terrestrial and the celestial reference systems (Petit and Luzum, 2010).

2.1 Basic principle of VLBI

The basic principle of VLBI is the observation of electromagnetic radiation emitted by extra-galactic radio sources, usually quasars. In the context of VLBI, this radiation is often referred to as the *signal*, although it consists of purely random noise, to distinguish from all the other noise components present. Due to the distance of these radio sources, which can amount to billions of light-years, the radiation arrives on Earth as planar wave-fronts. In the case of the legacy S/X system, observation happens in the S- and X-bands, which lie in the microwave region of the electromagnetic spectrum (Schuh and Böhm, 2013). Assuming that two radio telescopes observe the same source simultaneously, we call the difference between the signal reception times t_1 and t_2 the delay τ. Ignoring any external effects like Earth rotation or atmospheric delays, this delay relates to the vector $\vec{b}$ between the two stations, called the baseline, and the direction to the source $\vec{s_0}$ by the following equation

$$\tau = t_2 - t_1 = -\frac{1}{c}\vec{b} \cdot \vec{s_0} \tag{2.1}$$

with c being the speed of light in vacuum. To determine the delay between the stations, each station records the signal received from the observed source. These digitized and time-tagged signals are then stored on hard drives and transferred over the internet (or physically shipped) to a dedicated correlation center. In the correlation process, the cross-correlation function of the two recordings is determined. The delay τ can then be found as the shift

between the two signals that maximizes this cross-correlation (Nothnagel, 2019).

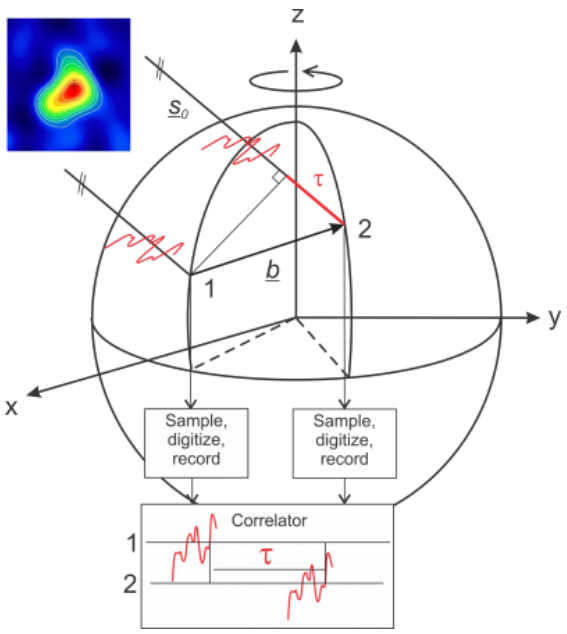

Figure 2.1: Geometric principle of VLBI for two telescopes at the points 1 and 2, with baseline vector $\vec{b}$, direction to the radio $\vec{s_0}$ and delay τ. Figure from Schuh and Böhm (2013).

2.2 Scheduling and observation

Before a VLBI observation session can be undertaken, observation schedules, defining which telescopes observe which sources at which points in time, have to be created. Various considerations must be taken into account in the scheduling process, some of which may depend on the specific purpose of a session for which the schedule is optimized, which makes the creation of a schedule a non-trivial task. The most basic thing to consider is source visibility, so that no telescope is scheduled to observe a source which is below the horizon. Another limitation is the slew speed of the telescope, which places a lower limit on the time between the observation of two different sources. In this context it is also important to consider that due to the cable links (which must be secured from over-twist) between the fixed and the turning parts of a telescope, it is limited in its azimuth rotations. Additionally, the observation duration, which depends on source flux, telescope sensitivity and source elevation, to reach a predefined minimal SNR, must be calculated. One factor usually optimized for in the scheduling is the sky coverage, meaning that at each telescope, the celestial hemisphere above is homogeneously filled with observations, which also ensures a good estimation of the atmospheric refraction parameters (Nothnagel, 2023). For the scheduling process, different software such as *sked* (Vandenberg, 1999) or *VieSched++* (Schartner and Böhm, 2019) exist.

In the case of legacy S/X VLBI systems, observation takes place, as the name implies,

in the S- and X-bands of the radio spectrum (2.2-2.4 GHz and 8.2-9.0 GHz, respectively), while for VGOS (cf. section 2.5) observation takes place in four 1 GHz bands spread over a range of 2 to 14 GHz. At the telescope, the received signals are amplified, down-converted, digitized (usually 1-bit or 2-bit digitization) and time-tagged before being stored on physical media. The transfer of the raw VLBI data from the stations to the correlator is either done by physically shipping the hard disks, or increasingly common via e-transfer over an internet connection. (Nothnagel, 2023)

2.3 Correlation and fringe-fitting

Obtaining the delay between the signals from two different telescopes from the raw data is the purpose of the correlation and fringe-fitting steps (level-0 and level-1 data processing). Simplified, this is done by calculating the cross-correlation function of the two signal streams. This cross-correlation function will then have its maximum at the delay in question. In practice, a Fourier-transformation and multiplication of the signals is performed, yielding the cross-spectrum (FX correlation) (Nothnagel, 2023). A widely used software for VLBI correlation is the Distributed FX (DiFX) correlator (Deller et al., 2011).

Extracting the delay observable from the correlator output is the next step of the process chain. This is referred to as fringe-fitting (Gruber, 2022). In this process, the the most likely values of the delay τ and delay rate $\dot{\tau}$ that maximize the cross-correlation function are found as the peak of the so-called 2D resolution function. To improve this determination, bandwidth synthesis from the narrow frequency channels observed is performed. (Nothnagel, 2023)

2.4 VLBI analysis and products

To estimate the parameters of interest from the delays obtained in the previous processing steps, the most common method is a Gauss-Markov least-squares adjustment, with other methods such as a Kalman filter or least-squares collocation finding use as well. A priori delays are corrected for all known effects that can be modeled with enough accuracy. Some parameters are of comparatively low interest, such as clock offsets or zenith wet delays, but must be estimated due to the unavailability of accurate a priori models. For the analysis of 24 hour sessions (as opposed to one hour intensives), station coordinates, source coordinates and EOP are usually among the estimated parameters. (Nothnagel, 2023)

For the realization of celestial and terrestrial reference frames, or for estimation of parameters such as the Love numbers (Spicakova et al., 2010), where parameters with a validity for all sessions in the observing period are determined with high accuracy, global solutions are employed. To do this, normal equation matrices from single session analysis are reduced to contain only the desired global parameters, and are stacked by adding them together.

Then, the global parameters can be estimated. (Mayer, 2018)

The most important data products provided[1] by the International VLBI Service for Geodesy & Astrometry (IVS) are therefore the Earth Orientation Parameter time series (of which of all space geodetic techniques only VLBI can provide the full set) and the terrestrial and celestial reference frames.

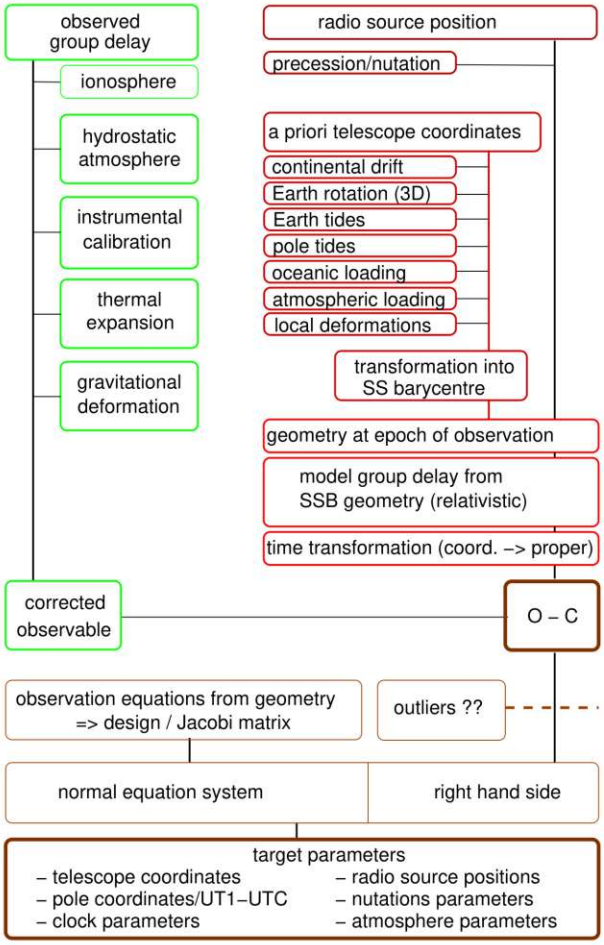

Figure 2.2: Schematic data flow in Gauss-Markov model VLBI analysis. Figure from Nothnagel (2023)

2.5 VLBI Global Observing System (VGOS)

To meet the ever higher demand for accuracy in VLBI, the next generation VLBI system was developed, under the name of *VLBI Global Observing System* (VGOS). The main objectives for this new system are global baseline accuracies of 1 mm, continuous measurements for station coordinate and EOP time series and a turnaround time for initial geodetic results of 24 hours (Niell et al., 2005).

[1] `https://ivscc.gsfc.nasa.gov/products-data/products.html`

Compared to the older S/X systems, VGOS specifications call for smaller telescopes of about 12 m diameter, to allow for faster slew rates. To compensate for the smaller antenna size and allow for short observation times, VGOS uses a different observing frequency setup compared to legacy VLBI. Instead of the S and X band, VGOS observes in four bands, spanning over a frequency range from 2 to 14 GHz. The faster slew rates together with the broadband observation system allow for more observations and better sky coverage, increasing the accuracy and time resolution of estimated tropospheric parameters. Achieving the desired millimeter accuracy for geodetic VLBI hinges primarily on this improved determination of atmospheric influence. (Nothnagel, 2023)

3 Tropospheric effects in VLBI

This chapter deals with the effects the troposphere has on space geodetic techniques, and VLBI in particular, mainly following Nilsson et al. (2013). A main focus lies on the concept of mapping functions, which relate zenith delays to slant delays in a non-zenith direction.

3.1 Propagation of electromagnetic waves in the neutral atmosphere

The troposphere is the lowest layer of the Earth's atmosphere. Its height varies from a minimum of 9 kilometers up to 17 kilometers depending on latitude, and it is characterized by temperature decreasing with height (World Meteorological Organization, 1992). Even though the effects described here are caused by the whole neutral atmosphere, which also includes the stratosphere and lower parts of the mesosphere, the fact that the troposphere contains most of the atmosphere's mass and virtually all its water vapor, justifies the practice of speaking about *tropospheric* delays.

Electromagnetic fields are described by Maxwell's equations. Inside a neutral and non-conducting medium, as is the troposphere, these take the following form:

$$\nabla \cdot (\varepsilon \vec{E}) = 0 \tag{3.1}$$

$$\nabla \cdot \vec{B} = 0 \tag{3.2}$$

$$\nabla \times \vec{E} = -\frac{\partial \vec{B}}{\partial t} \tag{3.3}$$

$$\nabla \times \vec{B} = \mu\varepsilon \frac{\partial \vec{E}}{\partial t} \tag{3.4}$$

Here $\vec{E}$ and $\vec{B}$ represent the field vectors of the electric and the magnetic field, and ε and μ the electric permittivity and magnetic permeability of the medium. From these equations it is possible to derive wave equations for the electric and the magnetic field. For the case of the electric field, this equation is given below.

$$\nabla^2 \vec{E} = \mu\varepsilon \frac{\partial^2 \vec{E}}{\partial t^2} = \frac{n^2}{c^2} \frac{\partial^2 \vec{E}}{\partial t^2} \tag{3.5}$$

Here, $c = \sqrt{\varepsilon_0 \mu_0}$ denotes the speed of light in vacuum, and n is the refractive index of the

medium. For the Earth's troposphere, this refractive index is very close to one, so often the *refractivity* N is used instead, and defined as

$$N = (n-1) \cdot 10^6 \tag{3.6}$$

Generally speaking, refractivity is a complex number consisting of three parts:

$$N = N_0 + N'(\nu) - iN''(\nu) \tag{3.7}$$

In the case of signals observed with space geodetic techniques (optical or microwave range), the effects caused by the real and imaginary parts can be considered separately. The real part with its non-dispersive, or frequency-independent, part N_0 and its dispersive, or frequency-dependent, part $N'(\nu)$ causes refraction and a propagation delay of the signal. The effect of the imaginary part is absorption, which apart from decreased signal-to-noise-ratios is usually not relevant for space geodesy and does not need to be modeled. Looking only at the real part, atmospheric refractivity can be expressed as a function of the densities ρ_i of the constituent gases and temperature.

$$N = \sum_i \left(A_i(\nu)\rho_i + B_i(\nu)\frac{\rho_i}{T} \right) \tag{3.8}$$

A_i and B_i are constants, and the second term inside the bracket is caused by the gas molecules' permanent dipole moment, a phenomenon that for the major atmospheric gases is unique to water vapor. Also assuming that the relative concentrations of all the other gases are constant, we can express refractivity as a function of pressure, temperature and humidity.

$$N = k_1(\nu)\frac{p_d}{T}Z_d^{-1} + k_2(\nu)\frac{p_w}{T}Z_w^{-1} + k_3(\nu)\frac{p_w}{T^2}Z_w^{-1} + k_4(\nu)\rho_{lw} \tag{3.9}$$

The last term describes the contribution of liquid water droplets but can usually be ignored. Z_d and Z_w are compressibility factors describing the deviation of dry air and water vapor from an ideal gas. The compressibility of a constituent gas is given by the equation

$$Z_i = \frac{pM_i}{\rho_i RT} \tag{3.10}$$

with molar mass M_i and universal gas constant R. In the frequency ranges employed by space geodetic techniques and VLBI in particular, refractivity is virtually frequency-independent, which along with neglecting of the liquid water part, gives the equation

$$N = k_1\frac{p_d}{T}Z_d^{-1} + k_2\frac{p_w}{T}Z_w^{-1} + k_3\frac{p_w}{T^2}Z_w^{-1} \tag{3.11}$$

where the coefficients k_i have been determined by laboratory measurements. The first term describes the dry refractivity caused by all constituent gases except water vapor, while the

last two terms describe the wet refractivity caused only by water vapor. However, a different separation is more practical and therefore more often used. For this, equation 3.11 is rewritten using equation 3.10

$$N = k_1 \frac{R}{M_d}\rho + k_2' \frac{p_w}{T} Z_w^{-1} + k_3 \frac{p_w}{T^2} Z_w^{-1} = N_h + N_w \tag{3.12a}$$

$$N_h = k_1 \frac{R}{M_d}\rho \tag{3.12b}$$

$$N_w = k_2' \frac{p_w}{T} Z_w^{-1} + k_3 \frac{p_w}{T^2} Z_w^{-1} \tag{3.12c}$$

with $k_2' = k_2 - k_1 \frac{M_w}{M_d}$. Refractivity is now separated into a hydrostatic part N_h which only depends on the total density of air, while the wet part N_w only depends on the partial pressure of water vapor and temperature. (Nilsson et al., 2013)

3.2 Tropospheric path delays

In VLBI, the difference in travel time of electromagnetic radiation from a quasar to telescopes on Earth is measured. This difference in travel time is converted into a distance by multiplying it with the speed of light in vacuum. An error to this distance is introduced by the atmosphere, because the propagation speed is lower than in vacuum and the signal path is affected. (Nilsson et al., 2013)

As variations of the atmospheric refractivity over the distance of a single wavelength are negligible, propagation of an electromagnetic wave can be described as a ray. For the electric path length L, which is the propagation time divided by the speed of light in vacuum, along the ray path S, we get

$$L = \int_S n(s) ds \tag{3.13}$$

This electric path is longer than the geometric length G of a straight line between the path's endpoints. The first reason is that the propagation velocity in the atmosphere is slower than in vacuum. The second reason is that the path S taken by the ray is differing from a straight line path. According to Fermat's principle, the path S is such that the electric path length L will be minimized. (Nilsson et al., 2013)

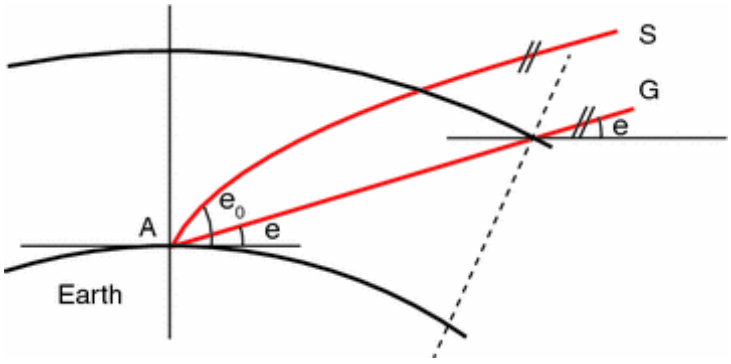

Figure 3.1: Path S taken by an electromagnetic signal in the atmosphere and the straight path G. Figure from Nilsson et al. (2013).

The atmospheric delay ΔL is now defined as the excess path length caused by the atmosphere:

$$\Delta L = L - G = \int_S n(s)ds - G = \int_S (n(s)-1)ds + \int_S ds - G = 10^{-6}\int_S N(s)ds + S - G \quad (3.14)$$

As defined in equations 3.12, we can divide the refractivity into its hydrostatic and wet parts[1], which yields a division of the path delay into a hydrostatic (ΔL_h) and wet delay (ΔL_w):

$$\Delta L = 10^{-6}\int_S N_h(s)ds + \int_S N_w(s)ds + S - G = \Delta L_h + \Delta L_w + S - G \quad (3.15)$$

In space geodesy, slant delays are commonly related to delays in the zenith direction via so-called mapping functions. For the zenith hydrostatic and the zenith wet delays, the corresponding expressions are as follows:

$$\Delta L_h^z = 10^{-6}\int_{h_0}^{\infty} N_h(z)dz \quad (3.16)$$

$$\Delta L_w^z = 10^{-6}\int_{h_0}^{\infty} N_w(z)dz \quad (3.17)$$

(Nilsson et al., 2013)

3.2.1 Hydrostatic delays

As described earlier, the hydrostatic refractivity, and therefore the hydrostatic delay, depend only on the total density of air. The hydrostatic delay can then be determined using the hydrostatic equation

$$\frac{dp}{dz} = -\rho(z)g(z) \quad (3.18)$$

[1]The effect of bending $S - G$ is considered to be part of the hydrostatic delay by convention.

where $g(z)$ is the gravity depending on the vertical coordinate. Integrating yields the pressure at a station height h_0:

$$p_0 = \int_{h_0}^{\infty} \rho(z)g(z)dz = g_{\text{eff}} \int_{h_0}^{\infty} \rho(z)dz \tag{3.19}$$

Instead of the height dependent gravity $g(z)$, the mean effective gravity g_{eff} is used:

$$g_{\text{eff}} = \frac{\int_{h_0}^{\infty} \rho(z)g(z)dz}{\int_{h_0}^{\infty} \rho(z)dz} \tag{3.20}$$

Inversion gives the height h_{eff} which corresponds to the height of the center of mass of the air above the station:

$$h_{\text{eff}} = \frac{\int_{h_0}^{\infty} \rho(z)z dz}{\int_{h_0}^{\infty} \rho(z)dz} \tag{3.21}$$

A globally valid approximation of the effective height was given by Saastamoinen (1972) as:

$$h_{\text{eff}} = (0.9h_0 + 7300\,\text{m}) \pm 400\,\text{m} \tag{3.22}$$

Given the pressure p_0 at the station, the zenith hydrostatic delay ΔL_h^z can be determined (see also equation 3.12b)

$$\Delta L_h^z = 10^{-6} k_1 \frac{R p_0}{M_d g_{\text{eff}}} \tag{3.23}$$

Following the approaches of Saastamoinen (1972) and Davis et al. (1986), the coefficients for this equation are determined. To begin, the effective gravity g_{eff} at height h_{eff} is determined by

$$g_{\text{eff}} = 9.862(1 - 0.00265\cos(2\theta) - 0.31 \cdot 10^{-6} h_{\text{eff}}) \tag{3.24}$$

which allows for a combination with equation 3.22 as

$$g_{\text{eff}} = g_m \cdot f(\theta, h_0) \tag{3.25}$$

where $g_m = 9.7840$ and the function f is defined as

$$f(\theta, h_0) = (1 - 0.00266\cos(2\theta) - 0.28 \cdot 10^{-6} h_0) \tag{3.26}$$

where θ is the latitude and and h_0 the orthometric height of the station. Putting these expressions into equation 3.23 yields

$$\Delta L_h^z = 10^{-6} k_1 \frac{R p_0}{M_d g_m f(\theta, h_0)} \tag{3.27}$$

and after the substitution of all values gives a formula for the zenith hydrostatic delay depending on the surface pressure at the station as

$$\Delta L_h^z = 0.0022768 \frac{p_0}{f(\theta, h_0)} \tag{3.28}$$

For typical weather conditions, the zenith hydrostatic delay takes values of about 2.3 m at sea level. (Nilsson et al., 2013)

To obtain pressure values at the station site, local pressure recordings, numerical weather models (e. g. ECMWF) or empirical models (e. g. GPT, *Global Pressure and Temperature* (Böhm et al., 2007)) can be utilised. (Nilsson et al., 2013)

3.2.2 Wet delays

From equations 3.12c and 3.17 follows the zenith wet delay as

$$\Delta L_w^z = 10^{-6} \left(\int_{h_0}^{\infty} (k_2' \frac{p_w}{T} Z_w^{-1}) dz + \int_{h_0}^{\infty} (k_3 \frac{p_w}{T^2} Z_w^{-1}) dz \right) \tag{3.29}$$

High temporal and spatial variability and unpredictability of the amount of water vapor in the atmosphere makes modeling the zenith wet delay far more difficult. To maintain accuracy in space geodetic techniques such as VLBI, the zenith wet delay is estimated as an additional parameter in the data analysis. Models for the determination of L_w^z are therefore mainly of interest for the determination of approximate initial values for least-square adjustments in the analysis step. (Nilsson et al., 2013)

3.3 Modeling slant delays

As already mentioned in section 3.2.2, atmospheric delays can be handled in two ways when analyzing VLBI, or more generally space geodetic data. The delays can be modeled and corrected for, or be introduced as parameters to be estimated in the analysis. The first approach is suitable for the hydrostatic delay, which can be determined accurately from surface pressure measurements, but for the wet delay, which is impossible to model from surface measurements alone, the second approach is suitable. Usually, these delays are modeled or estimated as zenith delays, and connected to the slant delay via mapping functions. An alternative approach uses estimates for both delays by calculating them from raytracing through a numerical weather model. (Nilsson et al., 2013)

3.3.1 Raytracing

From numerical weather models or radiosonde data, a refractivity field of the atmosphere can be inferred, using equation 3.11, which relates meteorological quantities to the refractivity.

If one were to integrate the refractivity along the path of an electromagnetic signal, the slant atmospheric delay would be determined. Usually, the propagation path of the signal is not known beforehand. The technique to obtain the path is called raytracing. It is based on the so-called Eikonal equations, which represents a solution of the Helmholtz equation for electromagnetic waves in a slowly varying medium. It has the form

$$\|\nabla L(\vec{r})\|^2 = n(\vec{r})^2 \tag{3.30}$$

where the gradient $\nabla L(\vec{r})$ is the direction of the ray, $L(\vec{r})$ is the optical path length and $n(\vec{r})$ the refractive index at the position $\vec{r}$. (Nilsson et al., 2013)

Hobiger et al. (2008) discuss different methods for raytracing through numerical weather models with regards to computational efficiency and accuracy. Assuming the ray does not leave its azimuthal plane, which means simplifying to a horizontally stratified atmosphere, 3D raytracing can be simplified into a 2D problem (Thayer approximation, Thayer (1967)). Böhm (2004) contains an algorithm for 1D raytracing, the geometry of which is schematically shown in figure 3.2.

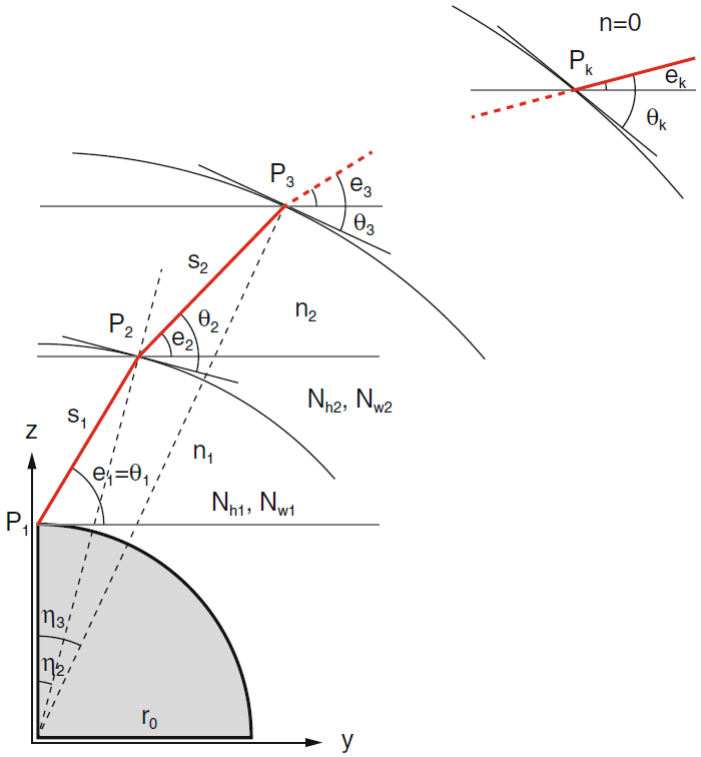

Figure 3.2: Sketch of the geometry of a 1D raytracing method as used for VMF1. Figure from Nilsson et al. (2013).

The atmosphere is divided into k different refractivity layers with heights h_i and refractive indices n_i. Adding the Earth's radius to the height of each layer yields the geocentric distance

r_i. For the point P_1, the position of a site or receiver, we have $z_1 = r_1$ and $y_1 = 0$. The elevation angles e_i are with respect to the horizontal plane at P_1, while the θ_i are the angles between the ray path and the tangential planes of the layer boundaries at the intersection points. Therefore, at the site, $e_1 = \theta_1$ holds. By iteration, the incremental paths S_i between the layer boundaries can be calculated:

$$S_i = \sqrt{r_{i+1}^2 - r_i^2 \cos\theta_i} - r_i \sin\theta_i \tag{3.31a}$$

$$z_{i+1} = z_i + S_i \sin e_i \tag{3.31b}$$

$$y_{i+1} = y_i + S_i \sin e_i \tag{3.31c}$$

$$\eta_{i+1} = \arctan \frac{y_{i+1}}{z_{i+1}} \tag{3.31d}$$

$$\delta_{i+1} = \eta_{i+1} - \eta_i \tag{3.31e}$$

$$\theta_{i+1} = \arccos\left(\frac{n_i}{n_{i+1}} \cos(\theta_i + \delta_{i+1})\right) \tag{3.31f}$$

$$e_{i+1} = \theta_{i+1} - \eta_{i+1} \tag{3.31g}$$

The total slant delay ΔL_d can then be calculated by

$$\Delta L_d = \sum_{i=1}^{n-1} S_i N_i \tag{3.32}$$

By replacing the total refractivity with its hydrostatic or wet component, the hydrostatic or wet delay components can be found. Replaying the S_i with the h_i yields an equation for zenith total delay. The delay component caused by bending is zero in the zenith direction and takes the form

$$\Delta L_b = \sum_{i=1}^{n-1} (S_i - \cos(e_i - e_k) S_i) \tag{3.33}$$

for slant directions. (Nilsson et al., 2013)

3.3.2 Mapping functions

In space geodesy, a tropospheric path delay $\Delta L(e)$ at an elevation angle e is customarily represented as the product of the zenith delay ΔL^z and an elevation dependent mapping function $mf(e)$ as

$$\Delta L(e) = \Delta L^z \cdot mf(e) \tag{3.34}$$

The concept of mapping functions is not only used for determining a priori slant delays, but also for estimating residual zenith delays in a least-squares adjustment, as the mapping function is the partial derivative of the observed delay used in this case. Unlike the partial derivatives of the observed delay w. r. t. to the station heights (which is $\sin e$), or w. r. t.

the station clocks (which is 1), the mapping function is not exactly known, and errors in the mapping function will, by correlation between zenith delays, station heights and clock parameters translate into an error of the estimated station heights and clock parameters. If the mapping function is too large, the estimated zenith delay will be too small and to compensate for the unchanged observed delay, the estimated station height is going to be too high. The reverse holds true for a mapping function with a value too small. A general rule of thumb estimates the station height error as about a fifth of the delay error at an elevation of 5°. (Nilsson et al., 2013)

Under the assumption of azimuthal symmetry of the troposphere around the site, which means that given a constant elevation angle, the path delay is equal for all azimuth angles, the approach is

$$\Delta L(e) = \Delta L_h^z \cdot mf_h(e) + \Delta L_w^z \cdot mf_w(e) \tag{3.35}$$

where $\Delta L(e)$ is the total path delay, ΔL_h^z and ΔL_w^z are the hydrostatic and wet zenith delays, and $mf_h(e)$ and $mf_w(e)$ are the hydrostatic and wet mapping functions. The input to the mapping functions is the vacuum elevation e, and the bending effect is accounted for in the hydrostatic mapping function. (Nilsson et al., 2013)

In essence, the mapping functions are a measure of the thickness of the atmosphere compared to the Earth's radius. Due to the smaller scale height of the wet part, the wet mapping function is larger than the hydrostatic one, except for cases with very low elevation, where the bending effect attributed to the hydrostatic mapping function becomes considerably larger. For a flat and evenly stratified atmosphere, the mapping function would be exactly $1/\sin e$. As described by Marini (1972), the mapping function can be described as a continued fraction of the form

$$mf(e) = \cfrac{1}{\sin(e) + \cfrac{a}{\sin(e) + \cfrac{b}{\sin(e) + \cfrac{c}{\sin(e) + \ldots}}}} \tag{3.36}$$

where the coefficients $a, b, c, \ldots$ are constants. Many approaches to determine mapping function coefficients have been developed, of which some developed at TU Wien will be described in the following. Today, a slightly modified continued fraction expression is widely

used instead,

$$mf(e) = \frac{1 + \cfrac{a}{1 + \cfrac{b}{1+c}}}{\sin(e) + \cfrac{a}{\sin(e) + \cfrac{b}{\sin(e)+c}}} \tag{3.37}$$

where the denominator ensures unity of the mapping function in the zenith direction. (Nilsson et al., 2013)

3.3.2.1 Vienna Mapping Functions 1

The Vienna Mapping Functions 1 (VMF1, Böhm et al. (2006b)) are an updated and improved version of the previously developed Vienna Mapping Functions (VMF) (Böhm and Schuh, 2004). For VMF1, the concept is to have an empirical expression for the coefficients b and c of equation 3.37, while the coefficient a is determined epoch-wise by raytracing through a numerical weather model. For the wet part, the coefficients are taken from the New Mapping Functions (NMF, Niell (1996)) at 45° latitude as

$$b_w = 0.00146 \tag{3.38a}$$

$$c_w = 0.04391 \tag{3.38b}$$

The empirical hydrostatic coefficients were determined by least-squares adjustment to a raytracing through the ERA-40 (ECMWF Re-Analysis 40-years) data for the year 2001. For the raytracing monthly mean profiles for the epochs 0, 6, 12 and 18 UT were downloaded on a global grid with 156 grid points, which amounts to 7488 profiles in total. The profiles consisted of 23 levels from 1000 hPa to 1 hPa, and contained values for height, total pressure, temperature and water vapor pressure at each level. For every profile, the value of the hydrostatic mapping function for an initial elevation angle e of 3.2°, 5°, 7°, 10°, 15°, 20°, 30°, 50°, 70° and 90° was determined. The coefficients a, b and c were then fitted to the ten discrete mapping function values for each profile, residuals of the fit were usually below 0.5 mm. The mean value of all the b coefficients was found to be

$$b_h = 0.0029 \tag{3.39}$$

and was kept fixed at this value for the next analysis steps. Now, the b coefficient was set to the value of b_h, and only the a and c coefficients were fitted to the mapping function values calculated from the numerical weather model. For the c coefficients a clear variability with

latitude and season was found and quantified as

$$c_h = c_0 + \left(\left(\cos\left(\frac{\text{doy}-28}{365.25}\cdot 2\pi + \psi\right)+1\right)\cdot\frac{c_{11}}{2} + c_{10}\right)\cdot(1-\cos\theta) \tag{3.40}$$

The parameters c_0, c_{10}, c_{11} and are dependent on the hemisphere of the site, as c_h is not symmetric with respect to the equator after correcting for the half-year phase offset expressed by the parameter ψ. Values are shown in table 3.1. From figure 3.2 it can be seen that the seasonal variation has a higher amplitude on the southern hemisphere.

Hemisphere	c_0	c_{10}	c_{11}	ψ
Northern	0.062	0.001	0.005	0
Southern	0.062	0.002	0.007	π

Table 3.1: Parameters for determining the c_h coefficient of VMF1, as given in Nilsson et al. (2013).

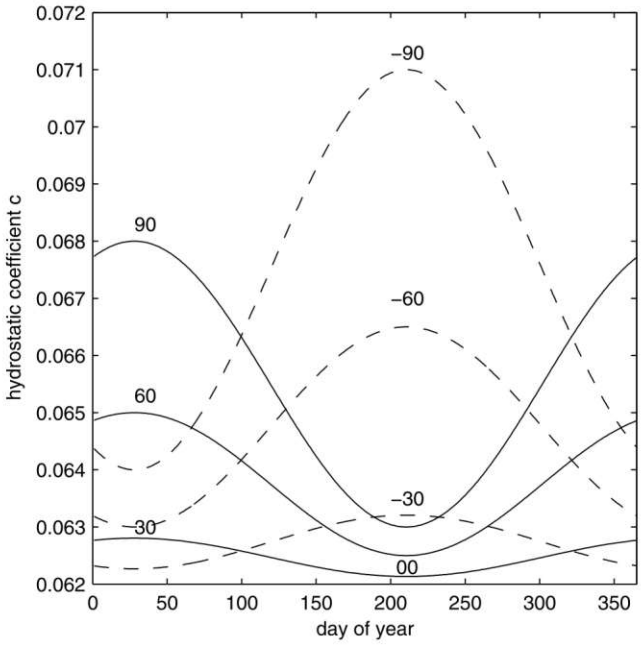

Figure 3.3: Graph of the hydrostatic c coefficient for VMF1 depending on the day of year for different latitudes. Figure from Böhm et al. (2006b).

For a given epoch and site, the a coefficients are determined by calculating the hydrostatic and wet mapping function for an initial elevation of 3.3° by raytracing and then inverting the continued fraction expression (equation 3.37), where b and c are replaced with the empirically found b_h and c_h or b_w and c_w respectively, for a. The difference between a raytraced delay and a delay calculated from VMF1 coefficients is at a maximum for an initial elevation angle of around 5°. (Böhm and Schuh, 2004)

TU Wien provides two sets of a coefficients for VMF1 on the VMF data server (`vmf.geo.`

tuwien.ac.at). One, the *VMF1_OP* is based on ERA-40 NWMs for the years up to and including 2001 and on OPERATIONAL NWMs for the years 2002 and onwards. These become available one day after their day of validity. The other set, *VMF1_FC* is based on FORECAST NWMs and is provided one day prior to the day of its validity. For each day, a coefficients are provided for all the epochs where NMWs are available, namely 00, 06, 12 and 18 UT. A further division exists between the *grid-wise* and the *site-wise* products. The grid-wise values are provided on a $2.0° \times 2.5°$ global grid at zero height, which together with a routine for height correction, can be used to interpolate values at an arbitrary location on Earth. Site-wise values are provided for a list of VLBI, DORIS and GNSS sites listed in separate coordinate files. Before July 1, 2018, the coefficients were calculated from raytracing at these exact locations, but since then are determined by interpolation from the grid-wise product, the difference between these methods being rather small. (Böhm and Boisits, 2018)

3.3.2.2 Vienna Mapping Functions 3

The Vienna Mapping Functions 3 (VMF3, Landskron and Böhm (2018b)) try to improve upon the Vienna Mapping Functions 1 by eliminating shortcomings in the estimation of the empirical b and c coefficients and in the tuning to a specific elevation angle of around 3°. Like VMF1, they are based on raytracing through numerical weather models. The software used for raytracing is the 2D-raytracer *RADIATE* (Hofmeister and Böhm, 2017). Delays were calculated from monthly mean values of the ECMWF ERA Interim Pressure Level Data, ranging from 2001 to 2010 (leading to 120 epochs in total) on a $5° \times 5°$ global grid. At each grid point and for each epoch, delays were determined at elevations of 3.3°, 5°, 15° and 30° and azimuths of 0°, 45°, 90°, 135°, 180°, 225°, 270° and 315°, meaning 32 delays per grid point and epoch. As with VMF1, the a, b and c coefficients were determined by a least square adjustment for each grid point and epoch. To generate an empirical model for the b and c coefficients, parameters of a seasonal fit model (Lagler et al., 2013) of the form

$$\begin{aligned} b_h = A_0 + A_1 \cdot \cos\left(\frac{\text{doy}}{365.25} 2\pi\right) + B_1 \cdot \sin\left(\frac{\text{doy}}{365.25} 2\pi\right) + \\ A_2 \cdot \cos\left(\frac{\text{doy}}{365.25} 4\pi\right) + B_2 \cdot \sin\left(\frac{\text{doy}}{365.25} 4\pi\right) \end{aligned} \tag{3.41}$$

here presented exemplary for the b_h coefficient, were fitted to the mapping function coefficient time series of each grid point. A_0 corresponds to the mean value of the coefficient, while A_1 and B_1 represent the annual amplitudes, and A_2 and B_2 the semi-annual amplitudes. By this, parameters to calculate empirical b and c coefficients for any point in time have been determined. Example grids of the seasonal fit parameters for b_h are shown in figure 3.4. Theoretically, these five parameters could be provided in a global grid file for each of the four empirical mapping function parameters, from which an interpolation for any point on Earth could be made. As the loading of such a grid would take a considerable

amount of time for real-world applications, they are instead represented by a spherical harmonics expansion up to degree and order 12, for which 91 Legendre coefficients had to be estimated by a least-squares fit.

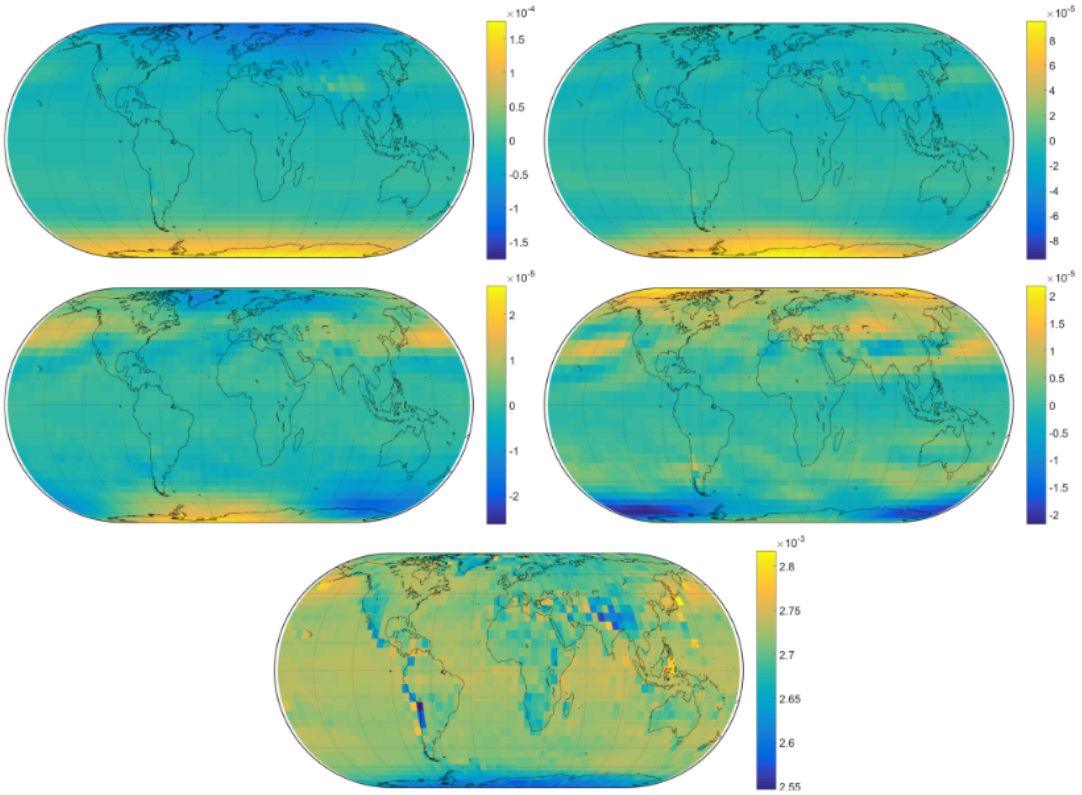

Figure 3.4: Map of the parameters for the seasonal fit model of the mapping function coefficient b_h. Top: annual amplitudes A_1 (left) and B_1 (right). Middle: semi-annual amplitudes A_2 (left) and B_2 (right). Bottom: Mean value A_0. Figure from Landskron and Böhm (2018b)

To calculate the empirical mapping function coefficients for a specific location and time, it is therefore necessary to at first calculate the values of the spherical harmonics expansions at the desired location to get the parameters of the seasonal fit models. The seasonal fit models then yield the b and c coefficients for the desired day of year (doy). (Landskron, 2017) Maps for an example epoch showing the difference between a grid-based and a spherical-harmonics based calculation are shown in figure 3.5.

The a coefficients are provided on the VMF data server and are determined from raytraced delays at 3° elevation and eight equally spaced azimuth angles. For VMF3, three different sets of a coefficients are available: *VMF3_EI* based on ERA-Interim NWMs, starting from 1980, *VMF3_OP* based on OPERATIONAL NWMs starting from 2008 and available one day after the day of their validity, and *VMF3_FC* based on FORECAST NWMs and available one day before their day of validity. As with VMF1, there are site-wise and grid-wise coefficient sets. Site-wise coefficients are provided for a list of DORIS, GNSS and VLBI stations, while

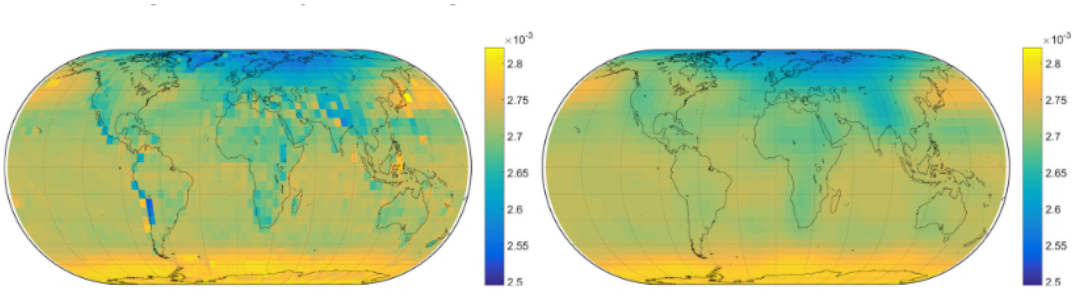

Figure 3.5: Maps of the grid of b_h coefficients at epoch MJD 51924 (January 15, 2001). Calculated directly from a grid of seasonal fit parameters (left), calculated from the spherical harmonics expansion of degree and order 12 (right). Figure from Landskron and Böhm (2018b)

the grid-wise coefficients are provided for points on a $5° \times 5°$ or $1° \times 1°$ global grid at zero height. Epoch availability is again the same as for the NWMs, i. e. 00, 06, 12 and 18 UT. (Böhm and Boisits, 2018)

3.3.2.3 Global Pressure and Temperature 3

The two mapping function approaches described above are so-called *discrete* models, as opposed to fully *empirical* models, as the a_h and a_w coefficients for VMF1 and VMF3 are calculated using external numerical weather models. A different approach would be to use an empirical expression for all coefficients of the continued fraction (equation 3.37). Many empirical mapping functions have been developed, for example the Global Mapping Functions (GMF, Böhm et al. (2006a)).

The empirical model Global Pressure and Temperature 3 (GPT3, Landskron and Böhm (2018b)) discussed here is deeply connected to and consistent with VMF3. It is not only a mapping function model, but provides a range of empirical meteorological quantities, such as gradients explained in the following section. (Landskron and Böhm, 2018b)

For now concerning only the mapping function part, the b and c coefficients used for VMF3 are adopted for GPT3 in their spherical harmonics expression, and new a coefficients based on them were calculated a $5° \times 5°$ grid, utilizing the same NWM data as used in the creation of VMF3. It is to be noted that the hydrostatic a_h coefficients had to be height-corrected to sea-level. Again, the five parameters of the seasonal fit model from equation 3.41 were determined for each time series at each grid point. Unlike with the b and c coefficients, the parameters of the seasonal fit of the a coefficients are stored directly as a grid and not expressed by spherical harmonics. With this, a fully empirical mapping function consistent with the discrete VMF3 has been realized. (Landskron, 2017)

3.3.3 Gradients

Mapping functions as described in the sections above are used to model tropospheric path delays under the assumption of azimuthal symmetry of the (neutral) atmosphere around the station, or in other words, that the vertical refractivity profile above a site is enough to determine the path delay at an arbitrary elevation angle. This assumption usually does not hold due to certain climatic and weather phenomena, making the path delay dependent on azimuth. One example is the fact that due to the troposphere being thicker at equatorial latitudes than at the poles, a path delay towards the south (on the northern hemisphere) will be systematically larger than towards the north, and vice versa for southern latitudes. (Nilsson et al., 2013)

A model of the total delay to account for this azimuthal asymmetry is given by

$$\Delta L(a,e) = \Delta L_0(e) + mf_g(e)(G_n \cos(a) + G_e \sin(a)) \tag{3.42}$$

where mf_g is the gradient mapping function describing the dependence of azimuthal asymmetry on the elevation angle e, given by

$$mf_g(e) = \frac{1}{\sin(e)\tan(e) + C} \tag{3.43}$$

where the coefficient C has the value $C = 3H/R_e$, with H being the scale height of the neutral atmosphere and R_e the mean Earth radius. Assuming a scale height of 6.5 km for the hydrostatic part and of 1.5 km for the wet part of the troposphere, this yields values of $C_h = 0.0031$ and $C_w = 0.0007$ (Chen and Herring, 1997). The azimuthal asymmetry is therefore described by the two parameters G_n, the north gradient, G_e, the east gradient (which both can be expressed as hydrostatic and wet gradients respectively), and the gradient mapping function $mf_g(a)$. (Landskron, 2017)

In the analysis of space geodetic techniques such as VLBI, the estimation of gradients as additional parameters is necessary, especially when dealing with observations at low elevation angles. A priori modeling on the other hand, is not needed as long as no constraints are applied on the estimation. (Nilsson et al., 2013)

4 Modeling and estimation of the troposphere in VieVS

This chapter gives an overview of the Vienna VLBI and Satellite Software (VieVS) in general, and about the options of modeling and estimating tropospheric parameters in particular.

4.1 The Vienna VLBI and Satellite Software

The *Vienna VLBI and Satellite Software* (VieVS, Böhm et al. (2018)) is a Very Long Baseline Interferometry analysis software developed at TU Wien since 2008 and used by the Vienna Analysis Center, jointly run by TU Wien and the Bundesamt für Eich- und Vermessungswesen (Federal Office of Metrology and Surveying, BEV) (Krásná et al., 2023b). It is written mainly in MATLAB and provided to the public as free software under the GNU General Public License.

VieVS is structured into different parts or modules. The most important for ordinary VLBI analysis are VIE_INIT, VIE_MOD and VIE_LSM. VIE_INIT is responsible for reading the data from NGS session files or VGOSDB databases, while VIE_MOD calculates the theoretical delays and the partial derivatives, models are implemented according to the IERS conventions (Petit and Luzum, 2010). VIE_LSM is estimating the various parameters such as EOP, station coordinates or clock offsets by least-squares estimation. A sketch of the different parts of VieVS is provided in figure 4.1.

Parameter estimation in VieVS is done by a Gauss-Markov least squares adjustment. Starting with the observation equation

$$v = \mathbf{A}x - l \tag{4.1}$$

where v is the vector of residuals, $\mathbf{A}$ denotes the design matrix, x the corrections to the a priori values of the parameters to be estimated, and l is the vector of differences between observed and computed observations, the parameters are estimated by

$$x = \mathbf{N}^{-1}\mathbf{A}^T\mathbf{P}l \tag{4.2}$$

where $\mathbf{N}$ is the normal equation matrix $\mathbf{A}^T\mathbf{P}\mathbf{A}$, and $\mathbf{P}$ is the weight matrix. (Böhm et al., 2018) Most of the geodetic parameters such as Earth orientation parameters, and stochastic parameters such as troposphere and clock functions are estimated by VieVS as piecewise linear offsets at integer hours. If certain parameters are to be provided as constant for a given

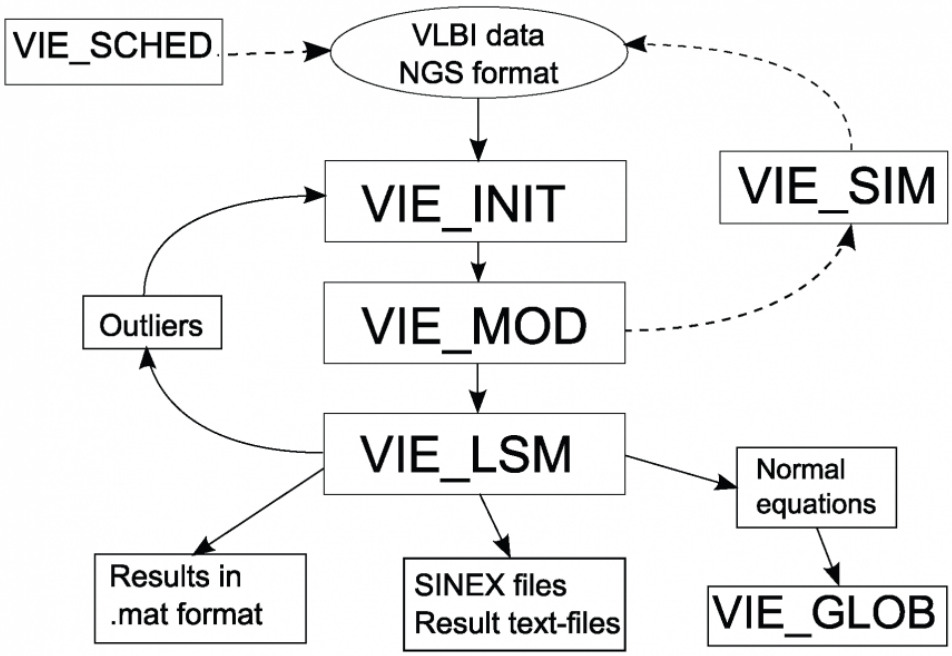

Figure 4.1: Sketch of the different modules of VieVS. Image taken from `vievswiki.geo.tuwien.ac.at/VLBI-Analysis`

session, this is achieved by implementing strong constraints between the hourly estimations. (Böhm et al., 2018)

4.2 Modeling tropospheric delays in VieVS

VieVS offers various options for the a priori modeling of tropospheric delays. It is either possible to use individual modeling or raytracing. For the raytracing approach, external files are provided for every VLBI session, containing raytraced delays for every observation, which were created with the software *RADIATE* (Hofmeister and Böhm, 2017). For individual modeling, different options to calculate zenith delays are provided, which can be set independently for the hydrostatic and wet zenith delays:

- no: no a priori modeling of the zenith delay.
- p (in situ) + Saasatamoinen: Using atmospheric pressure p measured at the site, and equation 3.28 to calculate the zenith hydrostatic delay.
- VMF3: Using the zenith hydrostatic or wet delays provided together with the a coefficients for the Vienna Mapping Functions 3 on the VMF data server.
- VMF1: Using the zenith hydrostatic or wet delays provided together with the a coefficients for the Vienna Mapping Functions 1 on the VMF data server.

- p (GPT3) + Saastamoinen: Using atmospheric pressure p from the empirical Global Pressure and Temperature 3 (GPT3, section 3.3.2.3) model, and equation 3.28 to calculate the zenith hydrostatic delay.
- e (in situ) + Askne: Using water vapor pressure e measured at the site, and equation 22 from Askne and Nordius (1987) to calculate the zenith wet delay.
- e (GPT3) + Askne: Using water vapor pressure e from the empirical Global Pressure and Temperature 3 (GPT3, section 3.3.2.3) model, and equation 22 from Askne and Nordius (1987) to calculate the zenith wet delay.

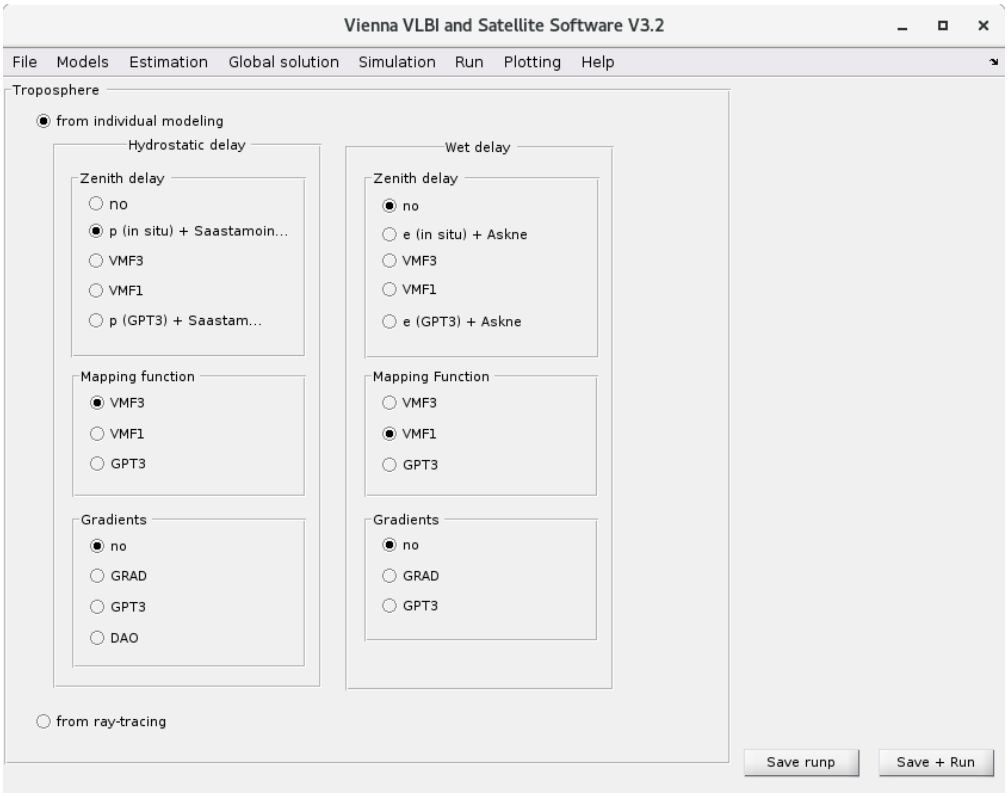

Figure 4.2: Options for tropospheric modeling in the Vienna VLBI and Satellite Software (VieVS) GUI.

The mapping function, which serves the dual purpose of modeling slant delays from a priori zenith delay, and as the partial derivative of the observed delay w. r. t. the zenith delay when estimating zenith delays as additional parameters, can be set independently for the hydrostatic and wet delay components in VieVS. The three options, VMF1, VMF3 and GPT3 correspond to the three mapping functions developed at TU Wien and described in previous sections 3.3.2.1 until 3.3.2.3.

The third option deals with the modeling of a priori gradients. Again, settings are independent for the hydrostatic and wet components. Four options are available for the modeling of gradients.

- no: no a priori modeling of gradients
- GRAD: These are gradients from the discrete GRAD model (Landskron and Böhm, 2018a), which are derived from raytracing through numerical weather models (in a way consistent with VMF3 products). These gradients are provided on the VMF data server.
- GPT3: With this option, empirical gradients from the model Global Pressure and Temperature (GPT3, section 3.3.2.3) are used.
- DAO: These are mean site gradients computed from the GSFC Data Assimilation Office (DAO) model (MacMillan, 1995; MacMillan and Ma, 1997) using meterological data from 1990 to 1995. Unlike the two gradient models above, these are total gradients without a separation into a hydrostatic and wet part.

4.3 Estimating tropospheric parameters in VieVS

For the estimation of tropospheric parameters in VieVS, it is possible to configure, most importantly, the selection of parameters to estimate at all. Three parameters can be selected, the zenith wet delay (ZWD), and the north and east gradients (NGR and EGR), which are estimated as total gradients. An additional setting is the estimation interval. In VieVS, the tropospheric parameters, as well as other parameters like clock offsets, are estimated using continuous piecewise linear offset (CPWLO) functions in the formation of the sub-design matrices. For example, the wet tropospheric slant delay $\Delta\tau^{wet}_{trop}(t)$ at an epoch t is given by

$$\Delta\tau^{wet}_{trop}(t) = m_w(t)x_1 + m_w(t)\frac{t-t_1}{t_2-t_1}(x_2-x_1) \tag{4.3}$$

where x_1 and x_2 are the zenith wet delays at epochs t_1 and t_2, and $m_w(t)$ is the wet mapping function of the observation at epoch t. Estimation of CPWLOs is done at integer hours, integer fractions of integer hours or integer multiples of integer hours. (Teke, 2011)

The third possible configuration option deals with so called constraints. These are realized as pseudo-observations added to the design matrix, which stipulate that the parameter at epoch t_{i+1} is equal to the parameter at epoch t_i. The associated accuracy of this pseudo-observation then defines the strength of this constraint. The main purpose of setting constraints is to ensure numerical stability and avoid singularities if an estimation interval contains only a small number of observations. (Mikschi et al., 2021)

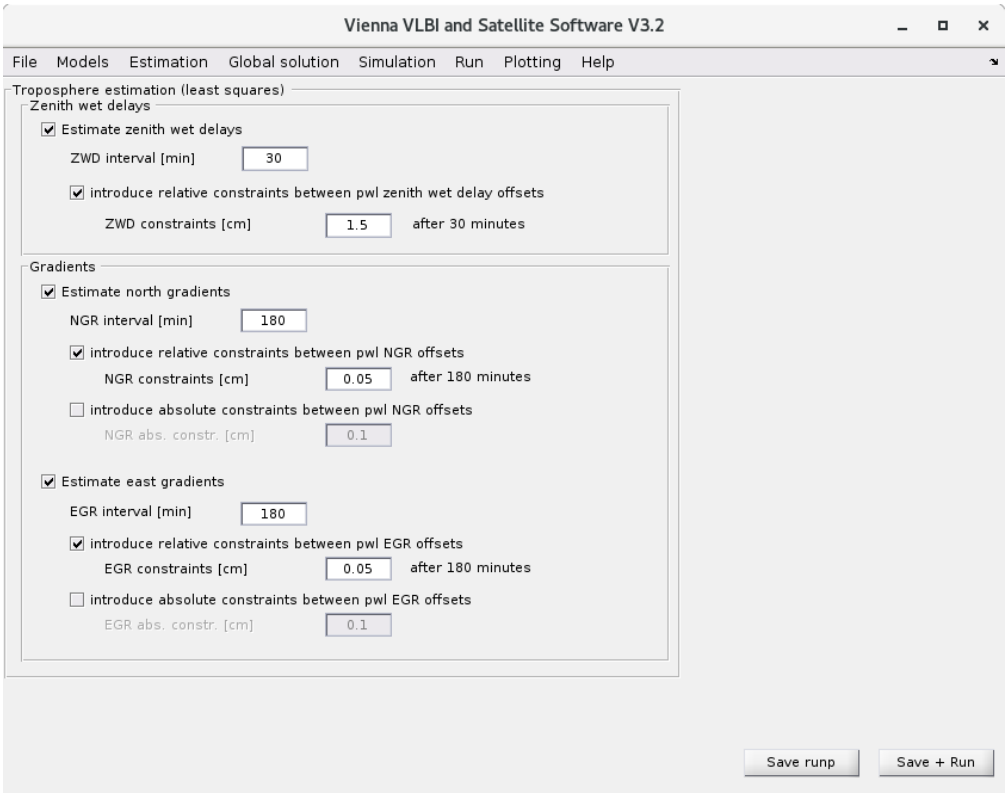

Figure 4.3: Options for the estimation of tropospheric parameters in the Vienna VLBI and Satellite Software (VieVS) GUI.

5 Comparison of mapping function settings

In this chapter, the influence of different mapping function choices on VLBI analysis with the Vienna VLBI and Satellite Software (VieVS) are examined. This was done mainly by observing how different settings for the hydrostatic and wet mapping function affect the baseline length repeatabilites (BLRs) in the analysis of a large number of legacy S/X and VGOS sessions. A systematic effect on the estimation of station heights that does not influence baseline length repeatabilities has been noted and will be discussed in separate sections.

5.1 Preprocessing

A total number of 3296 legacy S/X sessions from 2000 until 2020 as well as 36 VGOS sessions from the years 2017, 2019 and 2020 were used in the analysis. Beforehand, all sessions were analyzed with the parametrization of the solution code vie2022a (also referred to as *default parametrization* throughout this thesis). In the course of this preliminary analysis run, the VieVS internal outlier detection was activatated to detect and remove any erroneous observation. From this run, an output file containing every estimated baseline length was created. Plots of the time series for every baseline with at least ten length estimates (baselines with less than ten length estimates were ignored in the further course of this analysis) underwent visual inspection to remove sessions were the baseline length estimates clearly deviated from the overall trend, or where there were other reasons to believe that certain baseline estimates could interfere with a useful determination of baseline length repeatability. Baseline length repeatability as used in the course of this thesis is simply the standard deviation of the baseline length estimates' residuals w. r. t. a linear fit of the time series. In cases where discontinuities of the baseline length estimates are to be expected, e.g. earthquakes affecting a participating station, separate linear fits must be used for the timespans before and after the event. For this case, the epochs of such breaks are available in the VieVS internal `superstation.mat` file.

Baseline length estimates with a clear deviation from the overall trend, with an example shown in figure 5.1 were collected in a list of outliers and ignored in the further calculation of BLRs. The complete list of single baseline estimates deemed to be outliers is given in appendix A.1.

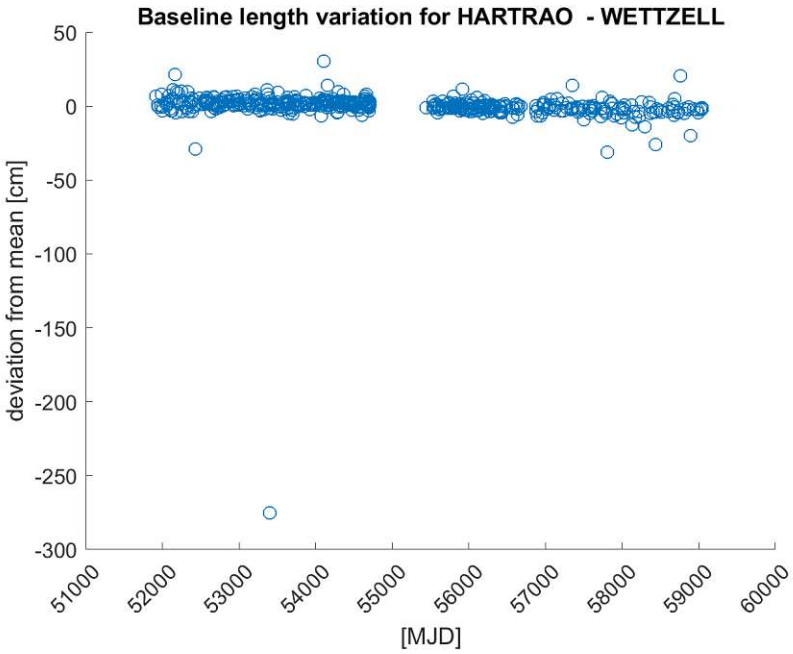

Figure 5.1: Baseline length estimates for HARTRAO–WETTZELL, shown as the difference from the mean value over the whole time series. Some outliers can be seen, the largest for the session 05JAN31XA, where the baseline length estimate is over 250 cm shorter than the mean value. The baseline estimates from those sessions were therefore removed in the later calculation of BLRs.

Also excluded from the further calculation of baseline length repeatabilites were baselines, where the whole time series exhibited noisy behavior and high variability in the baseline length estimates. A plotted example is shown in figure 5.2, with the whole list provided in appendix A.2.

Another group of excluded length estimates are those affected by the March 11, 2011 Tōhoku earthquake. These are baselines containing the station TSUKUB32 near Tsukuba, Japan. For these baselines, the post-seismic effects cause a clearly nonlinear evolution of baseline length for almost two years after the earthquake. As the baseline length repeatability, as defined and calculated for the purpose of this thesis, works with the residuals of a linear fit, a systematic nonlinearity in the baseline length time series would lead to a worse estimation of repeatability than warranted by the actual variability. The timespan of excluded length estimates ranges from March 10, 2011 (MJD 55629) until January 7, 2013 (MJD 56299). An example plot showing the time series of baseline estimates for KOKEE–TSUKUB32 is given in figure 5.3.

With the 36 VGOS session, visual inspection of the baseline length time series revealed no obvious problems such as the ones described above.

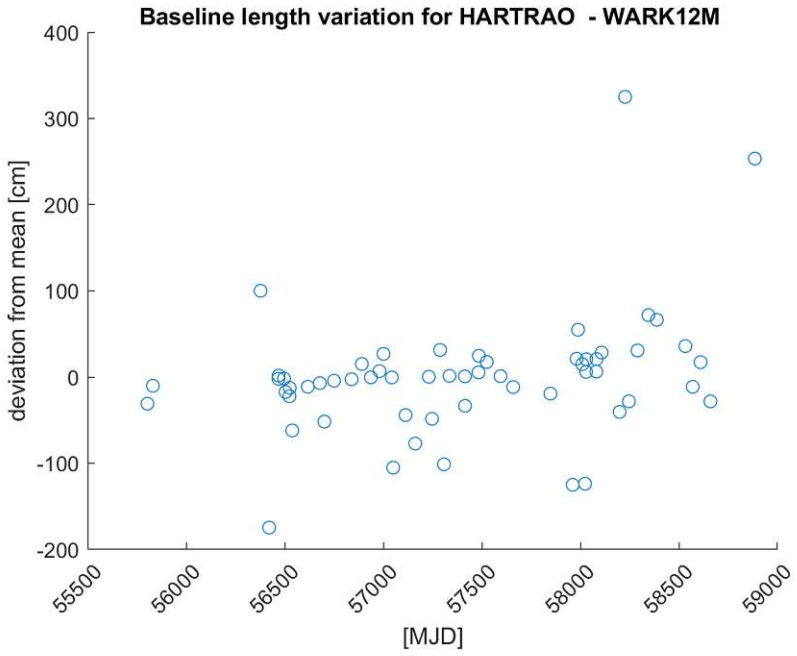

Figure 5.2: Baseline length estimates for HARTRAO–WARK12M. This baseline shows a general high variability in its length estimates, in the order of decimeters and meters. It was not included in the analysis of how the choice of mapping functions affect baseline length repeatabilities.

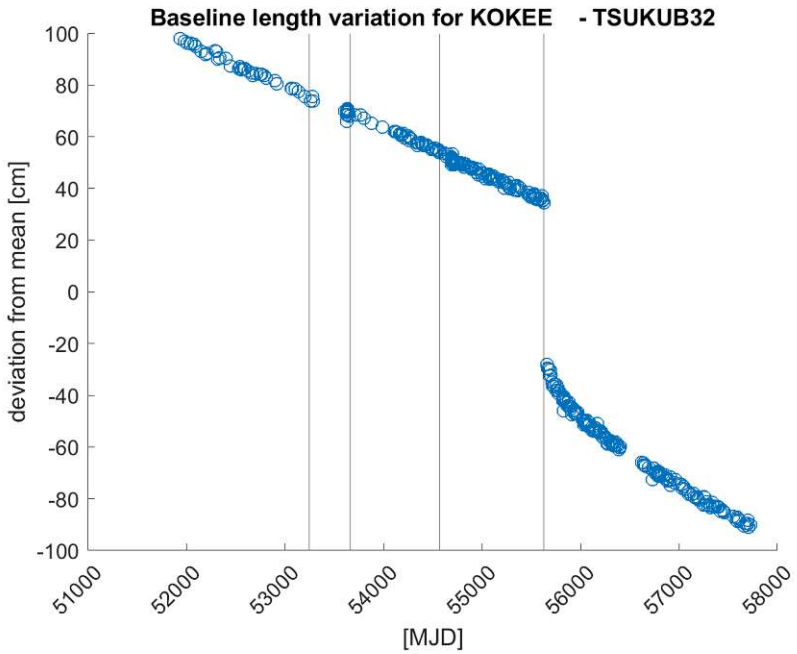

Figure 5.3: Baseline length estimates for KOKEE–TSUKUB32. A clear break and a temporarely nonlinear trend are visible after the March 11, 2011 Tōhoku earthquake. The nonlinear section was removed to avoid a biased estimation of baseline length repeatability.

5.2 Mapping function setups

For this part of the thesis, five different settings for the mapping functions in VieVS were compared to each other. The parametrization used at that time for analysis at the Vienna VLBI Analysis Center is specified in the solution code 2022a, and was used in the following investigation, apart from the settings concerning the chosen mapping functions. For the modeling of the troposphere, the settings referred to as *default* or *VMF3/1* in the course of this chapter are as follows (cf. figure 4.2):

- zenith hydrostatic delay: In situ pressure values and the formula from Saastamoinen (equation 3.28). If no pressure values measured at a site are available, VieVS uses values from GPT3 as a fallback option instead.
- zenith wet delay: No a priori modeling, the zenith wet delay is only estimated in the least squares adjustment.
- hydrostatic mapping functions: Vienna Mapping Functions 3
- wet mapping functions: Vienna Mapping Functions 1
- gradients: no a priori modeling, gradients are only estimated in the least squares adjustment (this is another difference to the 2022a solution code, which uses a priori DAO gradients).

The decision to use hydrostatic VMF3 was done to avoid the discontinuities in the VMF1 stemming from the switch from direct site-wise calculation to grid interpolation (cf. section 3.3.2.1), while wet VMF1 was preferred due to its calculation, which is only based on the vertical delay profile above a station, in comparison to VMF3, which is calculated from raytraced slant delays at eight different azimuths. (Böhm, J., personal communication)

Regarding the estimation of zenith wet delays and gradients, the following settings were made, and unchanged for all setups (cf. figure 4.3):

- zenith wet delays: estimated every 30 minutes, relative constraints of 1.5 cm between estimates
- north and east gradients: estimated every 180 minutes, relative constraints of 0.05 cm between estimates

Four additional setups regarding the selected mapping function were then used to process the same process lists of sessions. Two setups use the Vienna Mapping Functions 1 and 3 in a consistent way, i. e. the same mapping function is used for both the hydrostatic and wet delay, unlike the mixing done in the default setup. These setups will be referred to as *VMF1/1* and *VMF3/3* respectively. A third setup switches the choice from the default setup and uses the VMF1 for the hydrostatic delay and VMF3 for the wet delay. This setup was

named *VMF1/3* for the purpose of this thesis. The last tested setup (GPT3) uses the empirical mapping functions from GPT3 for the hydrostatic and wet delays.

5.3 Comparing baseline length repeatabilities

To assess the model quality of the different mapping functions available in VieVS, baseline length repeatabilities (BLRs) are examined. Baseline length has the advantage of being independent of any rotations, which makes it a good measure of the accuracy achieved in VLBI. (Niell, 2007)

As described above, baseline length repeatbilities are calculated by subtracting a linear fit from a time series of baseline length estimates and calculating the standard deviation of the obtained residuals. In the case of discontinuities, separate linear fits are employed before and after. If the residuals are weighted with the inverse of their formal errors of the baseline length estimates, weighted baseline length repeatabilites (WBLRs) are obtained.

In a first step, the calculated BLRs and WBLRs were plotted against baseline length (see figures 5.4–5.7). An additional quadratic fit of baseline length repeatability w. r. t. baseline length has been performed and is also plotted.

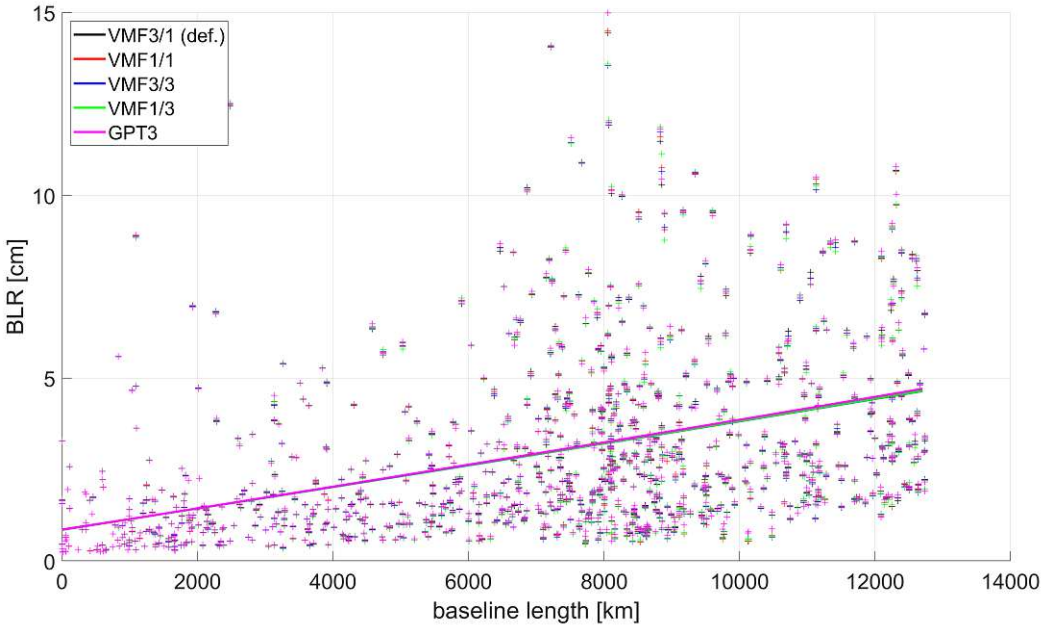

Figure 5.4: Plot of baseline length repeatabilities against baseline length from the session analyses with the five different mapping function setups (legacy S/X sessions). The lines indicate the best-fitting quadratic polynomials.

From the plots alone, it seems that the influence of the chosen mapping functions on baseline length repeatability is not significant. The fitted second degree polynomials indicate

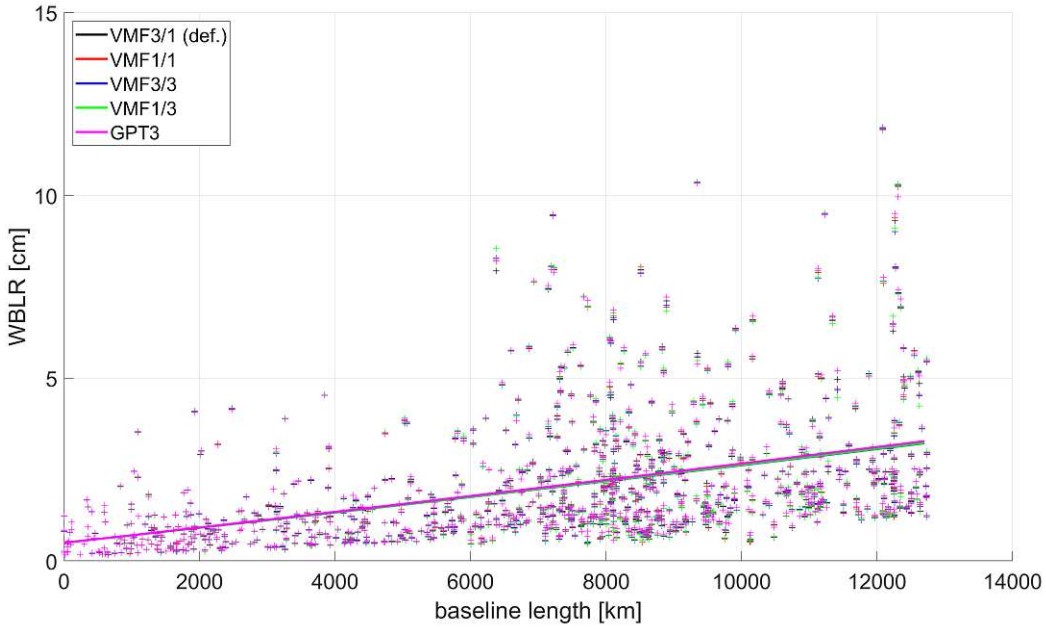

Figure 5.5: Plot of weighted baseline length repeatabilities against baseline length from the session analyses with the five different mapping function setups (legacy S/X sessions). The lines indicate the best-fitting quadratic polynomials.

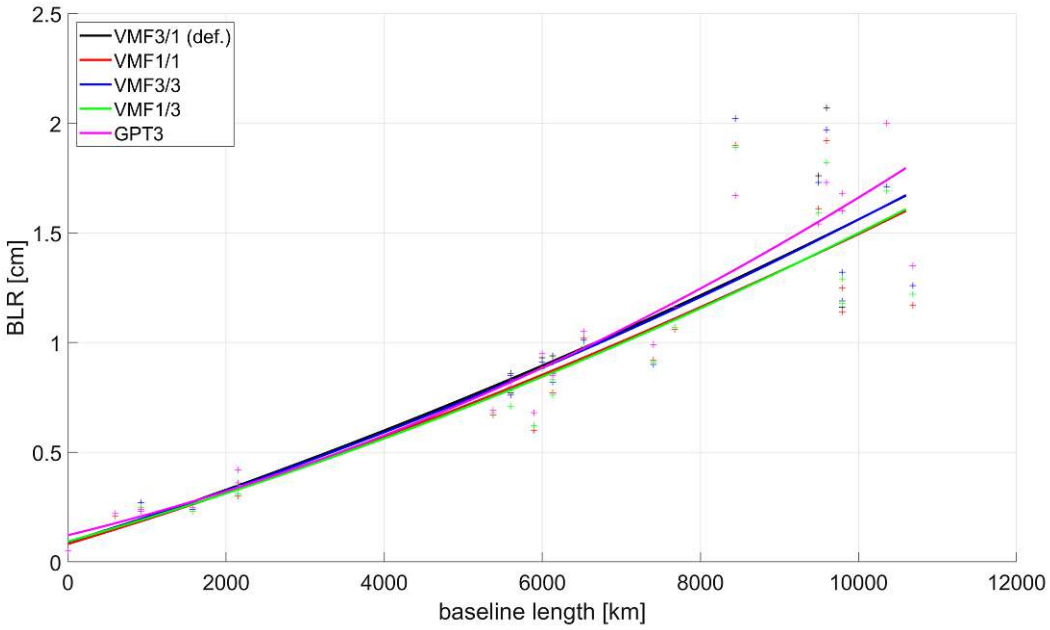

Figure 5.6: Plot of baseline length repeatabilities against baseline length from the session analyses with the five different mapping function setups (VGOS sessions). The lines indicate the best-fitting quadratic polynomials.

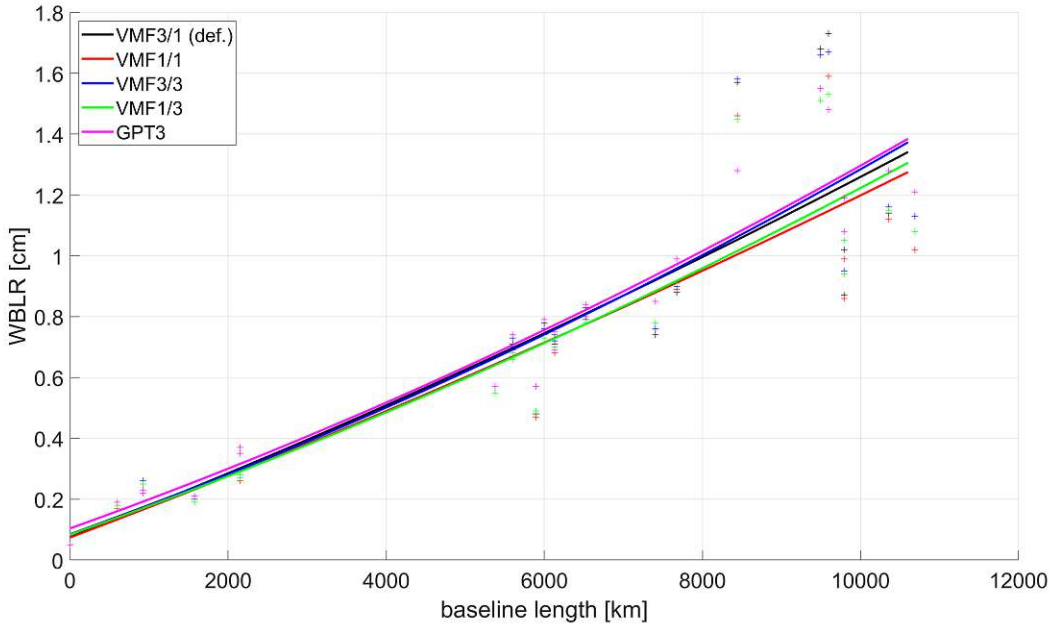

Figure 5.7: Plot of weighted baseline length repeatabilities against baseline length from the session analyses with the five different mapping function setups (VGOS sessions). The lines indicate the best-fitting quadratic polynomials.

a slightly worse performance when choosing GPT3, which was expected for an empirical model, as opposed to the discrete Vienna Mapping Functions.

As a first analysis, for each of the five mapping function setups, the number of baselines for which that setup yielded the best results was counted. Repeatabilites of 948 different baselines were calculated (after removing noisy baselines or those participating in less than ten sessions) from the analyses of S/X sessions, and 24 from the VGOS sessions. The results from this comparison are provided in table 5.1. Note that the numbers add up to more than 948 and 24 respectively, as baselines for which multiple setups provided an equally best repeatability (within a tenth of a millimeter) are counted more than once. Table 5.2 contains the same count with the weighted baseline length repeatabilities instead.

	VMF3/1	VMF1/1	VMF3/3	VMF1/3	GPT3
S/X	372	237	326	359	262
VGOS	3	14	2	10	5

Table 5.1: Number of baselines for which each mapping function setup provided the smallest repeatability.

The number of baselines for which each mapping function provides the best repeatability is alone not guaranteed to indicate the best tropospheric model. It could well be conceived that one model does merely spread out the resulting repeatabilities, therefore resulting in many baselines with a better repeatability than compared to a different model, but a comparatively

	VMF3/1	VMF1/1	VMF3/3	VMF1/3	GPT3
S/X	370	266	391	370	229
VGOS	5	14	1	9	6

Table 5.2: Number of baselines for which each mapping function setup provided the smallest weighted repeatability.

equal number of baselines for which repeatability is degraded, with no improvement on average. Therefore, it was also counted for how many baselines each setup yielded the worst repeatabilties. These numbers are provided in tables 5.3, and 5.4 for the weighted repeatabilities. Again, the numbers add up to more than 948 and 24, due to baselines with equally worst results for more than one setup being counted more than once.

	VMF3/1	VMF1/1	VMF3/3	VMF1/3	GPT3
S/X	282	130	120	266	538
VGOS	10	1	6	2	18

Table 5.3: Number of baselines for which each mapping function setup provided the largest repeatability.

	VMF3/1	VMF1/1	VMF3/3	VMF1/3	GPT3
S/X	246	116	118	241	611
VGOS	8	1	6	1	18

Table 5.4: Number of baselines for which each mapping function setup provided the largest weighted repeatability.

Concerning the numbers of best results, the mapping function setups which mix VMF1 and VMF3 (VMF3/1 and VMF1/3) seem to perform well for S/X sessions, as does the VMF3/3 setup, when considering weighted baseline length repeatabilities. For most baselines, the GPT3 setup yields the worst BLRs and WBLRs, for both VGOS and legacy S/X sessions. As mentioned earlier, this can be expected for an empirical model in contrast to the discrete Vienna Mapping Functions, whose coefficients are determined from numerical weather models. For VGOS sessions, VMF1/1 appears to perform best, both in terms of baselines where it yields the best repeatability, as well as in the fact that only one baseline has its worst repeatability with this setup. It has to be mentioned that the number of VGOS sessions as well as the size of the VGOS network are smaller compared to legacy S/X VLBI, which means that results cannot be expected to be as robust.

A factor not yet discussed is the magnitude of the difference in baseline length repeatability for the different settings. For this comparison, the (W)BLRs obtained with the VMF3/1 setup were, for each baseline, subtracted from the repetabilities obtained with the other setups. Diagrams and histograms of these differences are shown in figures 5.8 and 5.9. Histograms are only provided for the baselines from legacy S/X sessions, as the small number

of VGOS baselines makes this visualization less useful. In the tables 5.5 and 5.6 the means of the differences w. r. t. VMF3/1 are given. Tables 5.7 and 5.8 contain the average relative improvement or degradation w. r. t. VMF3/1, expressed in percent.

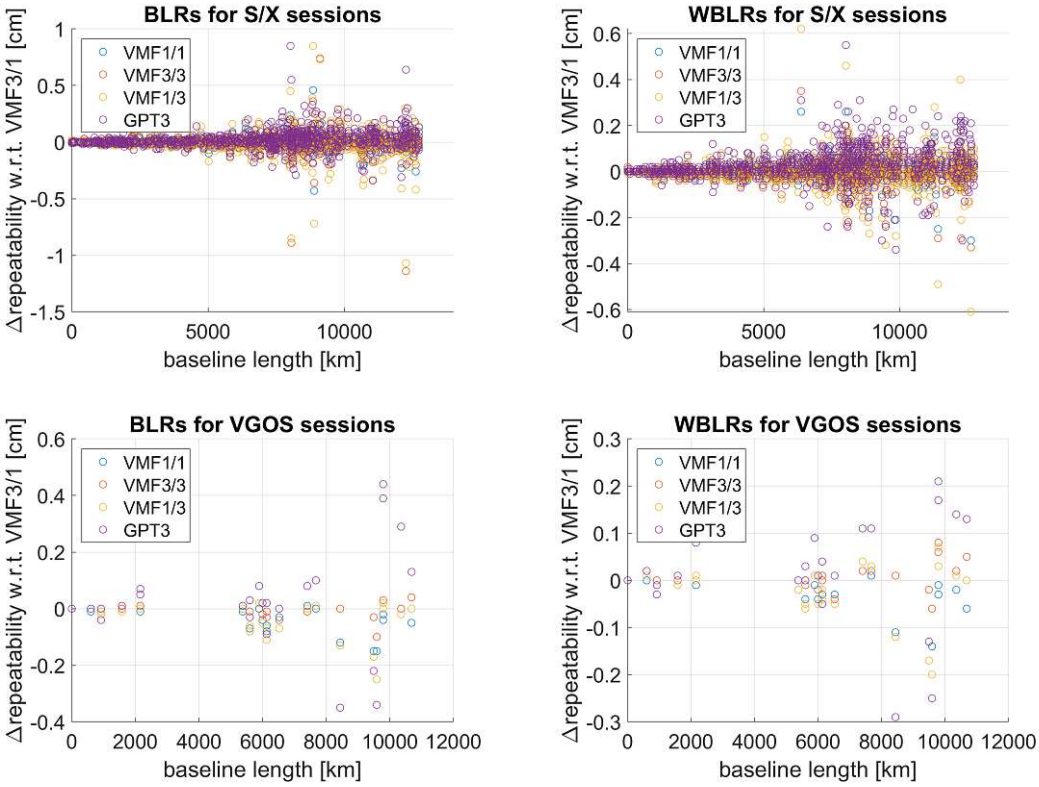

Figure 5.8: BLRs (left) and WBLRs (right) from the legacy S/X (top) and VGOS (bottom) sessions, expressed as the differences between those obtained with the VMF1/1, VMF3/3, VMF1/3 or GPT3 setups and the VMF3/1 setup.

	VMF1/1	VMF3/3	VMF1/3	GPT3
S/X	0.000 (0.040)	−0.005 (0.070)	−0.000 (0.093)	0.021 (0.081)
VGOS	−0.040 (0.046)	−0.005 (0.028)	−0.042 (0.067)	0.027 (0.182)

Table 5.5: Average difference in baseline length repeatabilities from four of the setups w. r. t. the VMF3/1 setup. Values in centimeters, negative numbers indicate an improvement. Standard deviations in parentheses.

	VMF1/1	VMF3/3	VMF1/3	GPT3
S/X	−0.000 (0.032)	−0.004 (0.040)	0.001 (0.064)	0.027 (0.073)
VGOS	−0.033 (0.042)	0.006 (0.029)	−0.025 (0.063)	0.021 (0.118)

Table 5.6: Average difference in weighted baseline length repeatabilities from four of the setups w. r. t. the VMF3/1 setup. Values in centimeters, negative numbers indicate an improvement. Standard deviations in parentheses.

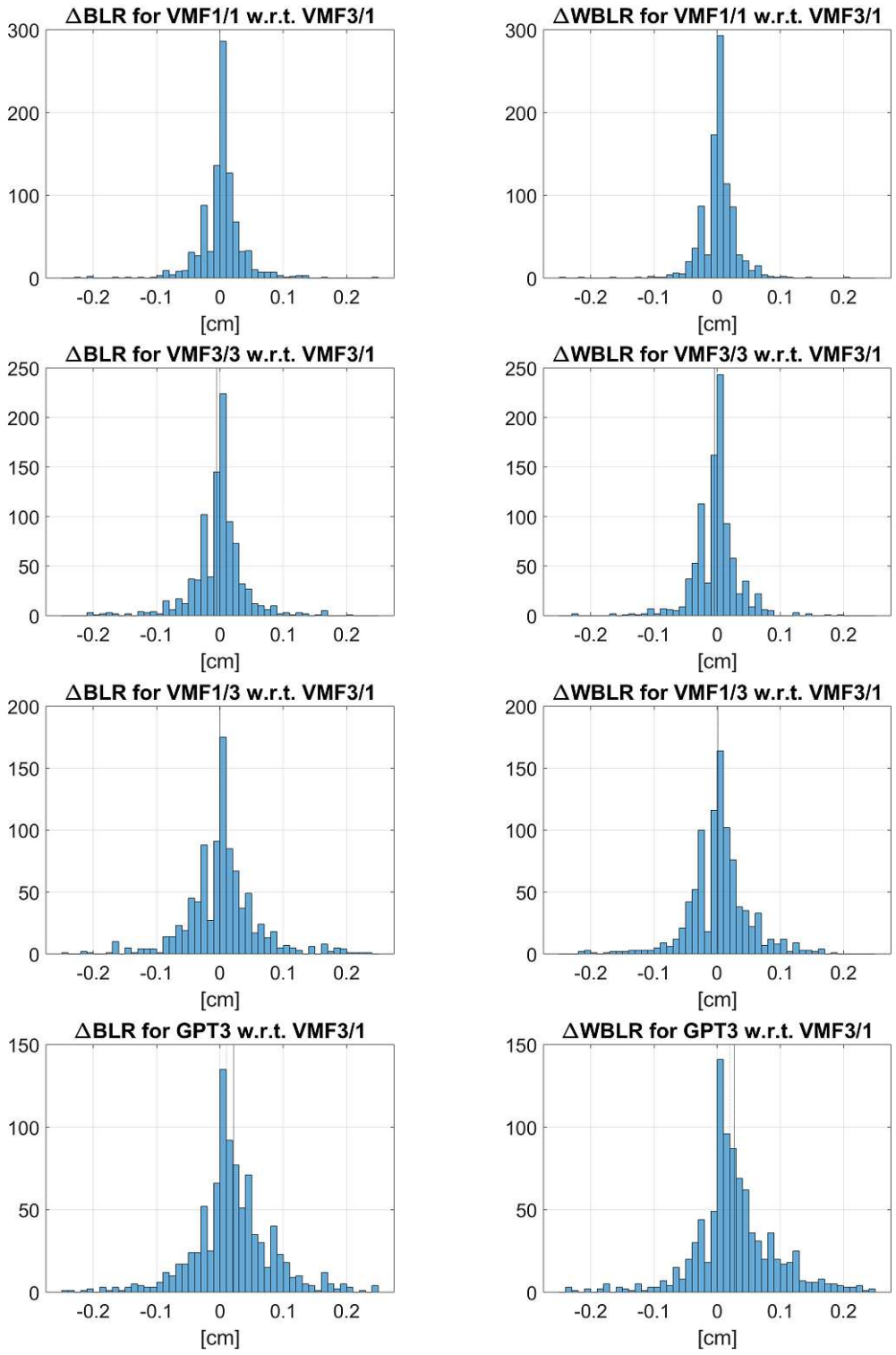

Figure 5.9: Histograms of differences in repeatabilities (left) and weighted repeatabilities (right) for each baseline from the analysis of legacy S/X session. From top to bottom: VMF1/1, VMF3/3, VMF1/3 and GPT3. Negative values correspond to baselines with improved repeatabilities. Solid and dashed lines indicate mean and median respectively.

	VMF1/1	VMF3/3	VMF1/3	GPT3
S/X	−0.07 %	−0.22 %	0.05 %	1.46 %
VGOS	−4.06 %	−0.15 %	−3.68 %	4.31 %

Table 5.7: Average relative difference in baseline length repeatabilities from four of the setups w. r. t. the VMF3/1 setup. Negative numbers indicate an improvement.

	VMF1/1	VMF3/3	VMF1/3	GPT3
S/X	−0.17 %	−0.43 %	−0.03 %	2.33 %
VGOS	−3.54 %	1.06 %	−2.06 %	5.99 %

Table 5.8: Average relative difference in weighted baseline length repeatabilities from four of the setups w. r. t. the VMF3/1 setup. Negative numbers indicate an improvement.

It can be seen that on average the differences between the different mapping function setups are very small. This is consistent with the finding from Landskron (2017), which indicates that in VLBI analysis, baseline length repeatability is not much influenced by the modeling of the troposphere, as long as the zenith wet delays are estimated as parameters, which is virtually always done. While a certain trend in the direction of degradation can be inferred from the large number of baselines for which the consistent use of the mapping functions from GPT3 yields the worst repeatabilities, the difference between the discrete mapping functions and their consistent or mixed application is rather small with respect to effects on baseline length repeatability. For VGOS, the changes in the average relative difference of the BLRs is larger, but there are also much less VGOS sessions observed, which naturally makes these averages more prone to variation. It is still noteworthy, that for VGOS the setups which use VMF1 for the hydrostatic delay (VMF1/1 and VMF1/3) perform best, with VMF1/1 showing the best overall performance, while the analysis of the legacy S/X sessions favors VMF3/3. A later investigation, after more VGOS sessions will be available, hopefully reveals if this discrepancy is real or just resulting from the small sample size.

5.4 Comparing absolute baseline lengths

When looking at the estimated baseline lengths, a small but systematic difference is visible when comparing the results from analyses with consistent (i. e. VMF1/1 and VMF3/3) or mixed (i. e. VMF3/1 and VMF1/3) application of the discrete mapping functions. This effect of the size of approximately two millimeters was also noted in Krásná et al. (2023a), and named as an explanation for the difference of the scale parameter of the Vienna contribution to ITRF2020 (0.2 ppb compared to ITRF2014) compared to the ITRF2020 contributions from other analysis centers (scale parameters between 0.3 and 0.5 ppb compared to ITRF2014) as shown in Hellmers et al. (2022).

To visualize this finding, the baseline length estimates obtained with the VMF1/1 setup

were subtracted from the length estimates obtained with VMF3/3, VMF3/1 and VMF1/3. Length estimates considered to be outliers and those from noisy baselines as described in section 5.1 were ignored for this analysis. The obtained differences are plotted into histograms (figures 5.10 until 5.12). Means and medians of these differences are provided in tables 5.9 and 5.10.

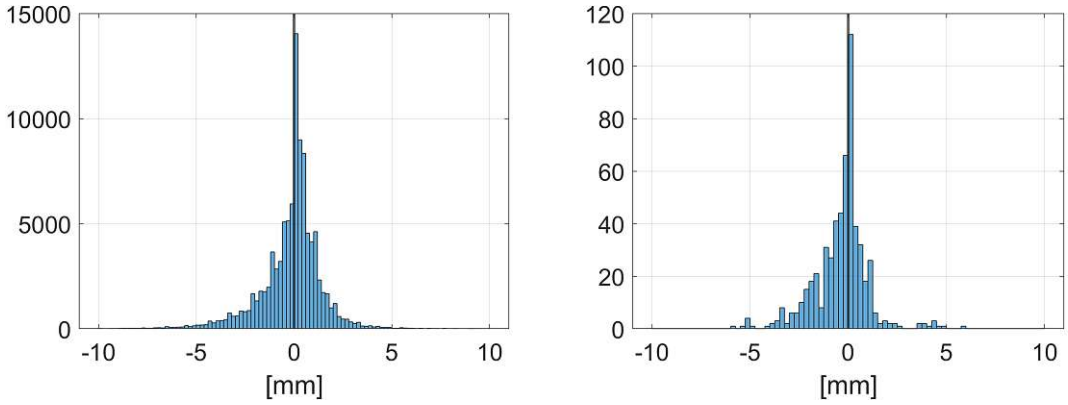

Figure 5.10: Histograms of the differences of the baseline length estimates from the analyses with VMF3/3 minus VMF1/1. The distributions are centered around zero, indicating that there is no systematic difference between the baseline length estimates. Results from S/X sessions left, from VGOS sessions right.

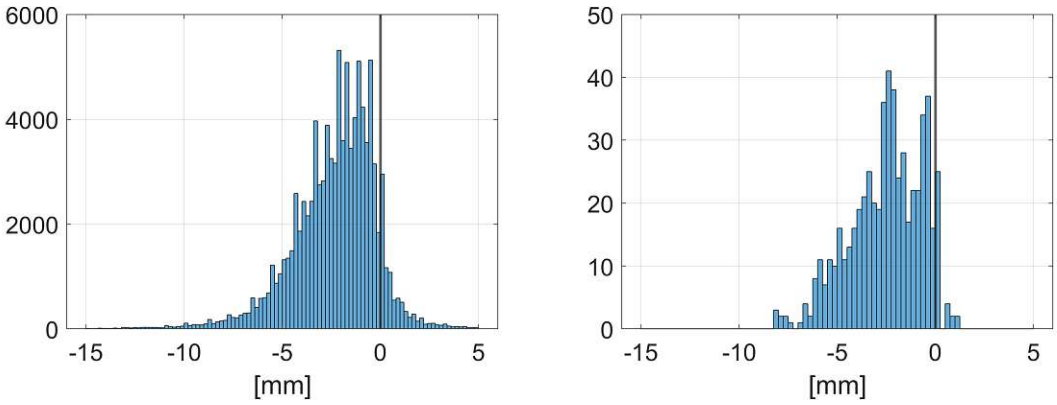

Figure 5.11: Histograms of the differences of the baseline length estimates from the analyses with VMF3/1 minus VMF1/1. The distributions are not centered around zero and skew left, indicating that baselines are on average shorter when the analysis is performed with the VMF3/1 setting, as compared to VMF1/1. Results from S/X sessions left, from VGOS sessions right.

For the histograms in figures 5.13 until 5.15, the difference in baseline length was divided by the baseline estimate obtained with the VMF1/1 setup. Values are plotted in parts per billion (ppb), equivalent to millimeters per 1000 kilometers. In tables 5.11 and 5.12, means and medians of these relative length differences are tabulated. Mean values are calculated

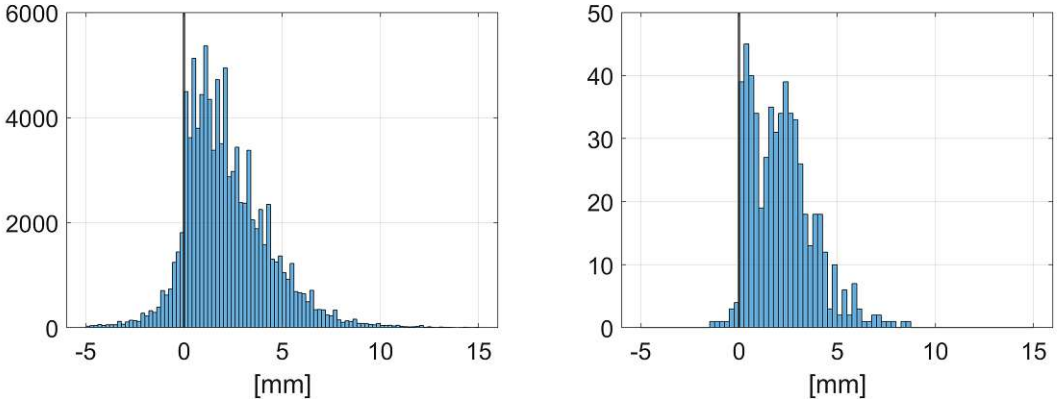

Figure 5.12: Histograms of the differences of the baseline length estimates from the analyses with VMF1/3 minus VMF1/1. The distributions are not centered around zero and skew right, indicating that baselines are on average longer when the analysis is performed with the VMF1/3 setting, as compared to VMF1/1. Results from S/X sessions left, from VGOS sessions right.

	VMF3/3	VMF3/1	VMF1/3
S/X	−0.13	−2.30	2.17
VGOS	−0.36	−2.52	2.16

Table 5.9: Average difference of baseline length estimates w. r. t. estimates obtained with VMF1/1. Values in millimeters.

	VMF3/3	VMF3/1	VMF1/3
S/X	0.1	−2.0	1.8
VGOS	−0.1	−2.3	2.0

Table 5.10: Median difference of baseline length estimates w. r. t. estimates obtained with VMF1/1. Values in millimeters.

as 5 % trimmed means to remove comparatively very large relative differences on the order of parts per million (ppm) occurring at extremely short baselines, these are also cut out from the histograms.

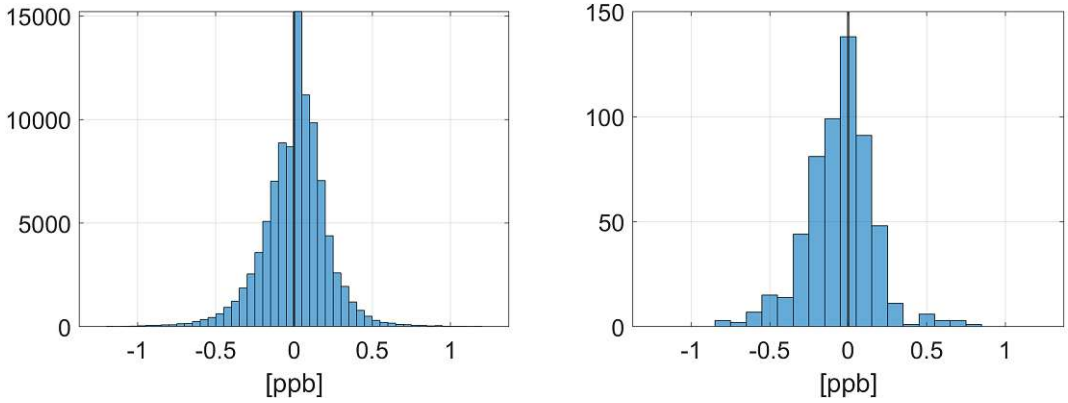

Figure 5.13: Histograms of the differences of the baseline length estimates from the analyses with VMF3/3 minus VMF1/1, divided by the respective baseline length estimate obtained with VMF1/1. The distributions are centered around zero, indicating that there is no systematic difference between the baseline length estimates. Results from S/X sessions left, from VGOS sessions right.

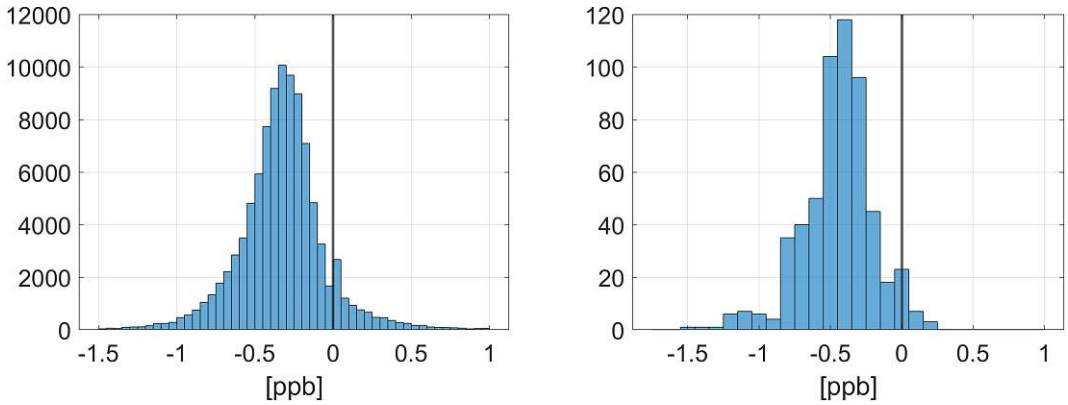

Figure 5.14: Histograms of the differences of the baseline length estimates from the analyses with VMF3/1 minus VMF1/1, divided by the respective baseline length estimate obtained with VMF1/1. The distributions are not centered around zero, indicating that baselines are on average shorter when the analysis is performed with the VMF3/1 setting, as compared to VMF1/1. Results from S/X sessions left, from VGOS sessions right.

A systematic lengthening or shortening of estimated baselines means that the whole network of VLBI stations is scaled. Such a scaling corresponds to a systematic effect on the estimated station heights, and station height errors can be introduced by incorrect tropospheric modeling.

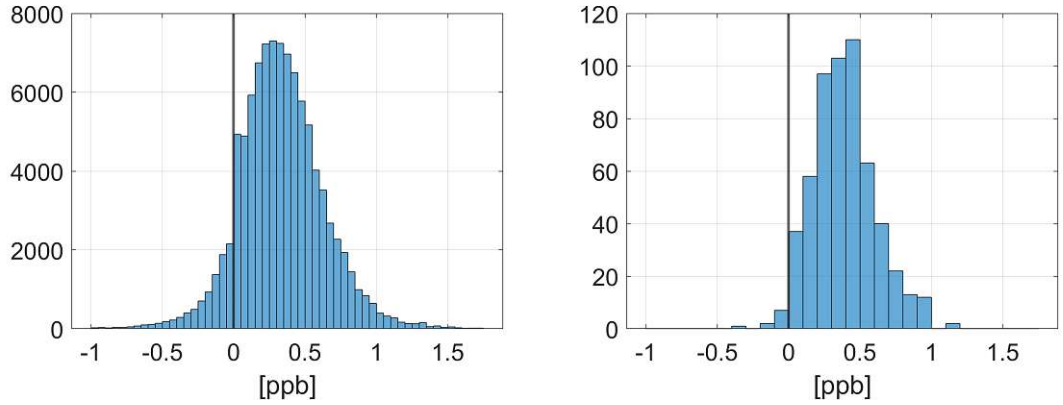

Figure 5.15: Histograms of the differences of the baseline length estimates from the analyses with VMF1/3 minus VMF1/1, divided by the respective baseline length estimate obtained with VMF1/1. The distributions are not centered around zero, indicating that baselines are on average longer when the analysis is performed with the VMF1/3 setting, as compared to VMF1/1. Results from S/X sessions left, from VGOS sessions right.

	VMF3/3	VMF3/1	VMF1/3
S/X	0.01	−0.33	0.33
VGOS	−0.06	−0.44	0.39

Table 5.11: 5 % trimmed means of the relative difference of baseline length estimates w. r. t. estimates obtained with VMF1/1. Values in parts per billion (ppb).

	VMF3/3	VMF3/1	VMF1/3
S/X	0.01	−0.32	0.32
VGOS	−0.03	−0.43	0.38

Table 5.12: Median relative difference of baseline length estimates w. r. t. estimates obtained with VMF1/1. Values in parts per billion (ppb).

5.5 Comparing estimated station heights and zenith wet delays

To further investigate the issue at hand, estimated zenith wet delays and station coordinates for a number of selected stations were exported to text files using a function provided by VieVS. The station coordinates were estimated as offsets (in X, Y and Z coordinates) to the a priori ITRF2020 coordinates. These offset vectors were then rotated into topocentric East, North and Up (ENU) coordinates. The Up-component of the rotated offset vector is then the offset in ellipsoidal height. Station coordinates for the transformation were taken from the `vlbi.ell` file on the VMF Data Server.[1]

With φ and λ being the station's latitude and longitude, the rotation takes the form

$$\begin{pmatrix} \Delta E \\ \Delta N \\ \Delta U \end{pmatrix} = \begin{pmatrix} -\sin\lambda & \cos\lambda & 0 \\ -\cos\lambda\sin\varphi & -\sin\lambda\sin\varphi & \cos\varphi \\ \cos\lambda\cos\varphi & \sin\lambda\cos\varphi & \sin\varphi \end{pmatrix} \begin{pmatrix} \Delta X \\ \Delta Y \\ \Delta Z \end{pmatrix} \tag{5.1}$$

as described in Subirana et al. (2011).

Figure 5.16 shows the difference of the offset vectors' Up-components w. r. t. the results obtained from the analysis of the legacy S/X sessions with the VMF1/1 setting for the station WETTZELL. It can be seen that with VMF3/3, the station is on average estimated at the same height, while the estimates with VMF3/1 place the station a few millimeters lower, and conversely the estimates with VMF1/3 place the station a few millimeters higher. This fits with the observation that baseline lengths from VMF1/1 and VMF_3 agree on average, while they are systematically shorter with VMF3/1 and longer with VMF1/3. The same plots for some additional stations (FORTLEZA, KOKEE, NYALES20, TSUKUB32, WESTFORD and YARRA12M) are provided in appendix B.1. These plots also support the observation that station heights are in general estimated lower when using VMF3/1, and estimated higher when using VMF1/3, while the results from VMF3/3 agree with those obtained with VMF1/1. In table 5.13, the mean differences of the Up-Offsets w. r. t. VMF1/1 are tabulated for the same seven stations.

To further investigate the relationship with the settings for tropospheric modeling in VieVS, the estimated zenith wet delays for the selected stations where exported as well and then plotted. As the ZWD was estimated every 30 minutes, this yields 48 estimates per station per session. To get cleaner plots, these were represented by a single session-wise average instead. In table 5.14, the means over all sessions of the differences of the zenith wet delays w. r. t. VMF1/1 are tabulated.

For the estimated zenith wet delays, the situation appears analogous. The differences between the estimates from VMF3/3 and VMF1/1 lie around zero, indicating a general agreement between the estimates. For VMF3/1, zenith wet delays are systematically estimated

[1] To find at `https://vmf.geo.tuwien.ac.at/station_coord_files/vlbi.ell`

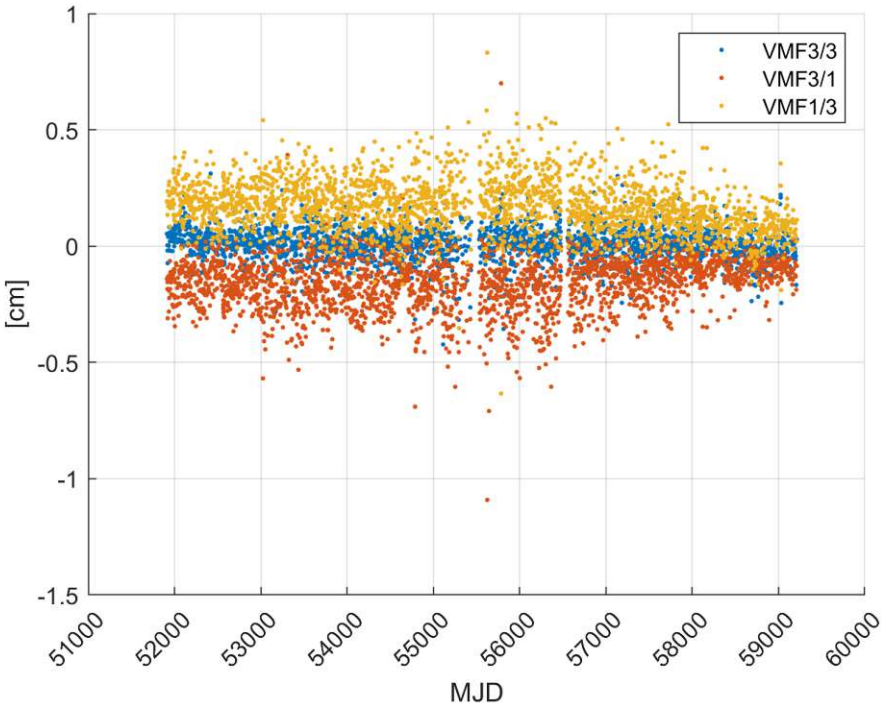

Figure 5.16: Difference in the estimated Up-offsets for WETTZELL w. r. t. the analyses with the VMF1/1 mapping function setup (legacy S/X sessions).

	VMF3/3	VMF3/1	VMF1/3
FORTLEZA	−1.01 (1.21)	−1.26 (1.17)	0.25 (1.38)
KOKEE	−1.23 (1.28)	−2.37 (1.74)	1.13 (1.36)
NYALES20	0.01 (0.35)	0.05 (0.68)	−0.04 (0.78)
TSUKUB32	−0.68 (1.92)	−2.89 (1.43)	2.20 (2.26)
WESTFORD	−0.02 (0.08)	−0.12 (0.12)	0.11 (0.13)
WETTZELL	0.09 (0.70)	−1.59 (1.08)	1.67 (1.11)
YARRA12M	−0.02 (0.59)	−0.59 (0.53)	0.56 (0.65)

Table 5.13: Mean differences of the Up-offsets w. r. t. the analysis with the mapping function setup VMF_c. Standard deviations in parentheses. Only legacy S/X sessions considered, values in millimeters.

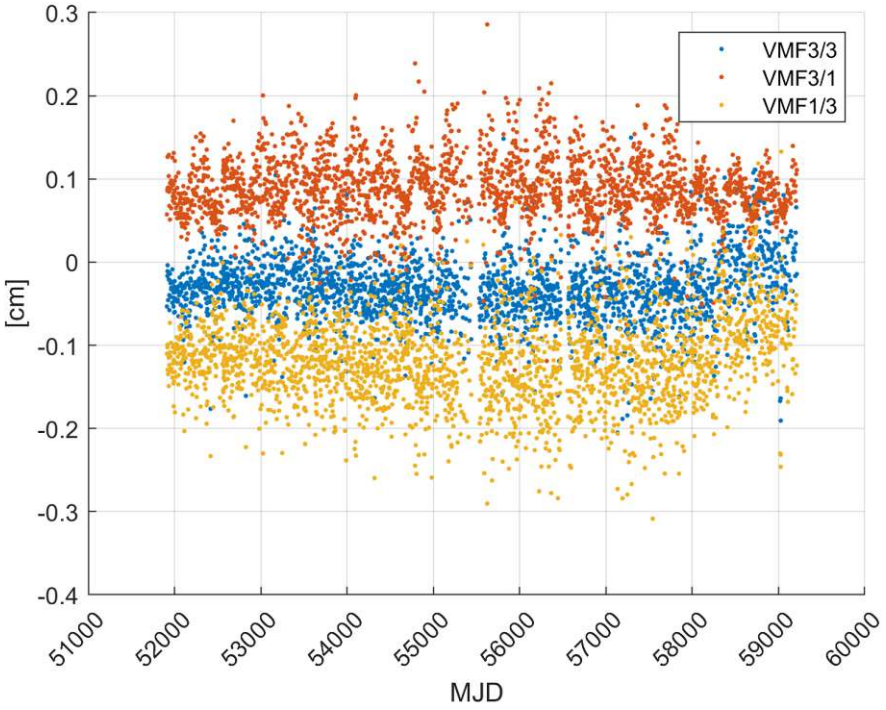

Figure 5.17: Difference in the estimated zenith wet delay for WETTZELL w. r. t. the analyses with the VMF1/1 mapping function setup (legacy S/X sessions). The small jump for the VMF3/3 and VMF1/3 time series (which use VMF3 for the wet mapping function) at around MJD 58300 coincides with the date where the calculation of site-wise VMF1 coefficients was changed to interpolation from grid-wise values (cf. section 3.3.2.1). The change in the estimated ZWDs caused by this cancels out in the difference between VMF3/1 and VMF1/1, which both use the wet VMF1, but becomes visible for the other two differences.

	VMF3/3	VMF3/1	VMF1/3
FORTLEZA	0.23 (0.52)	0.48 (0.48)	−0.25 (0.61)
KOKEE	0.59 (0.59)	0.65 (0.51)	−0.06 (0.48)
NYALES20	−0.50 (0.48)	0.80 (0.55)	−1.29 (0.70)
TSUKUB32	0.24 (1.12)	0.76 (0.47)	−0.52 (1.02)
WESTFORD	−0.28 (0.35)	0.75 (0.36)	−1.02 (0.46)
WETTZELL	−0.31 (0.49)	0.88 (0.50)	−1.19 (0.64)
YARRA12M	−0.05 (4.80)	0.57 (0.78)	−0.60 (4.43)

Table 5.14: Mean differences of the estimated zenith wet delays w. r. t. the analysis with the mapping function setup VMF_c. Standard deviations in parentheses. Only legacy S/X sessions considered, values in millimeters.

higher, and with VMF1/3 they are estimated lower. An obvious conclusion is to assume that the inconsistent mapping function setups cause a systematic difference in the estimated zenith wet delays, which are then, due to correlation, compensated by an opposite effect on estimated station heights.

In the case that zenith wet delays were not estimated but only modeled apriori, one would then expect that station height will still be systematically affected by inconsistent mapping function setups, but in the other direction compared to analyses where ZWDs are estimated. This is because the effect that causes zenith wet delays to be estimated higher (or lower) compared to the consistent setups is going to be absorbed into the other parameters, and station height is especially highly correlated with the zenith wet delay.

To test this assumption, the process list of S/X sessions used in this analysis was analyzed again with the four different mapping function setups, but zenith wet delays were not estimated as parameters, but only modeled using the ZWDs provided together with the *a* coefficients for VMF1 on the VMF data server (i. e. the option VMF1 on the *Wet delay – Zenith delay* submenu in figure 4.2). Again, for the seven stations investigated above, the Up-offsets obtained from the analysis with VMF1/1 were subtracted from those obtained with VMF3/3, VMF3/1 and VMF1/3. Timelines of the Up-offset differences were again plotted, as shown in figure 5.18 and appendix B.3. Tabulated mean differences are provided in table 5.15. As expected, the difference in the Up-offsets have in general a flipped sign, when compared to the values in table 5.13.

For the last analysis of this kind, zenith wet delays were again estimated, but station coordinates were fixed to their a priori values. Again, the estimated zenith wet delays for the seven stations were exported and plotted in figure 5.19 and appendix B.4. Mean values of the differences are tabulated in table 5.16. Compared to table 5.14, the absolute values of the differences in the estimated ZWDs become smaller when station coordinates are fixed. This behavior is explained by the fact that in the case when zenith wet delays and station coordinates are both estimated, the difference of the estimated zenith wet delays was accompanied by an inverse effect on station heights. Without this compensation, the effect on zenith wet delays cannot become as large, under the constraint of minimizing the sum of squared residual delays.

5.6 Differences between VMF1 and VMF3

As has been shown in the previous section, the choice of the hydrostatic and wet mapping functions used for modeling and estimating tropospheric parameters in VLBI analysis affects the resulting station heights and zenith wet delays. This happens in such a way that the results obtained with a consistent use of VMF1 agree with those obtained with a consistent use of VMF3, i. e. differences in the estimated parameters are close to and centered around zero. On the other hand, the differences between the parameters obtained with an incon-

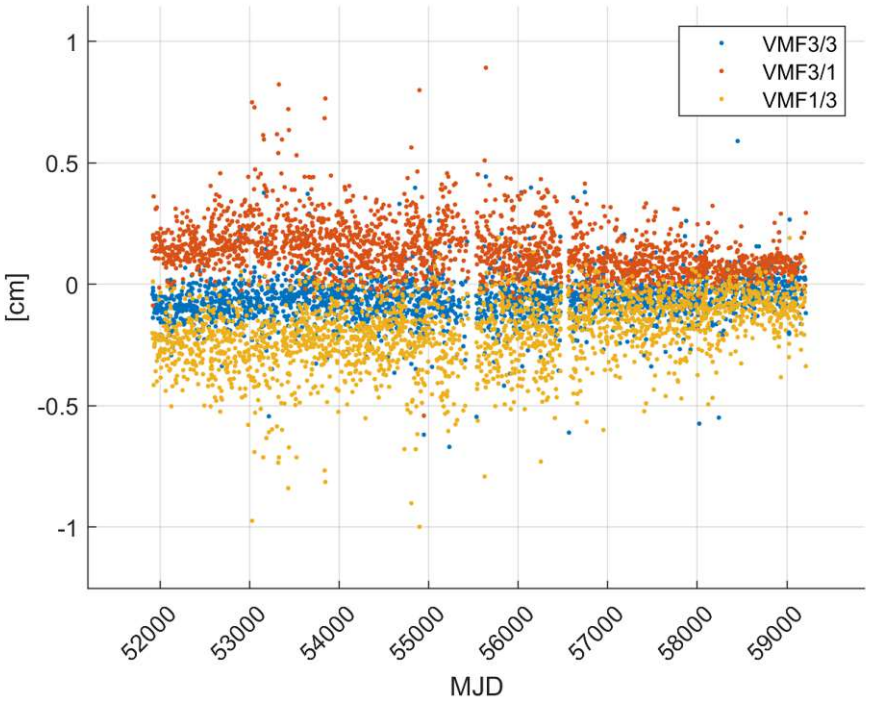

Figure 5.18: Difference in the estimated Up-offsets for WETTZELL w. r. t. the analyses with the VMF1/1 mapping function setup (legacy S/X sessions). Zenith wet delays were not estimated but modeled with the values provided on the VMF server together with the a coefficients of VMF1. Compared to figure 5.16, the differences between VMF3/1 and VMF1/1, and VMF1/3 and VMF1/1, flip sign.

	VMF3/3	VMF3/1	VMF1/3
FORTLEZA	0.26 (4.53)	0.76 (1.30)	−0.63 (1.63)
KOKEE	−0.18 (2.98)	1.37 (1.41)	−1.69 (1.77)
NYALES20	0.14 (0.93)	0.51 (0.93)	−0.67 (1.11)
TSUKUB32	−0.45 (2.05)	2.55 (1.75)	−3.04 (2.62)
WESTFORD	−0.06 (0.55)	0.12 (0.14)	−0.17 (0.17)
WETTZELL	−0.60 (1.68)	1.37 (1.12)	−1.97 (1.39)
YARRA12M	−0.10 (1.46)	0.39 (0.48)	−0.56 (0.74)

Table 5.15: Mean differences of the Up-offsets w. r. t. the analysis with the mapping function setup VMF_c. Standard deviations in parentheses. Zenith wet delays were modeled a priori instead of estimated as parameters. Only legacy S/X sessions considered, values in millimeters. Compared to table 5.13, the differences between VMF3/1 and VMF1/1, and VMF1/3 and VMF1/1, flip sign.

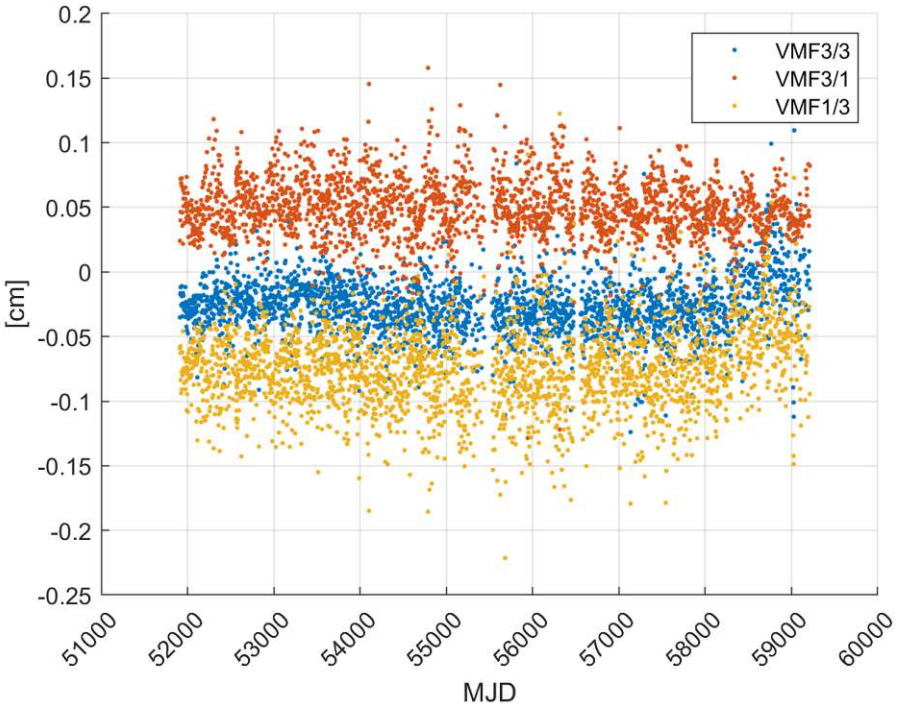

Figure 5.19: Difference in the estimated zenith wet delay for WETTZELL w. r. t. the analyses with the VMF1/1 mapping function setup (legacy S/X sessions). Station coordinates were not estimated and fixed to their a priori values.

	VMF3/3	VMF3/1	VMF1/3
FORTLEZA	0.04 (0.42)	0.21 (0.41)	−0.17 (0.49)
KOKEE	0.20 (0.50)	0.25 (0.44)	−0.05 (0.42)
NYALES20	−0.36 (0.38)	0.56 (0.46)	−0.91 (0.59)
TSUKUB32	0.07 (0.80)	0.42 (0.54)	−0.35 (0.74)
WESTFORD	−0.22 (0.27)	0.45 (0.34)	−0.67 (0.40)
WETTZELL	−0.26 (0.38)	0.49 (0.44)	−0.75 (0.53)
YARRA12M	−0.05 (0.60)	0.20 (0.49)	−0.25 (0.61)

Table 5.16: Mean differences of estimated zenith wet delays w. r. t. the analysis with the mapping function setup VMF_c. Standard deviations in parentheses. Station coordinates were not estimated and fixed to their a priori values. Only legacy S/X sessions considered, values in millimeters.

sistent use (e. g. VMF3 for the hydrostatic and VMF1 for the wet delay, which was used by the Vienna Analysis Center, called the *VMF3/1* setup above) differ from those obtained with a consistent application. This happens in such a way, that compared to using the mapping functions consistently, the inconsistent usage done by the Vienna Analysis center results in higher zenith wet delays and lower station heights in the order of around one to two millimeters on average. As noted in Krásná et al. (2023a), the difference of the scale parameter of the Vienna Analysis Center's contribution to ITRF2020 compared to the contributions by other VLBI analysis centers, can be traced to this inconsistent application of VMF1 and VMF3 done by the Vienna Analysis Center.

In an attempt to find how these differences between the parameters estimated from consistent and inconsistent usage arise, the values of the VMF1 and VMF3 were calculated for different elevation angles (5°, 10° and 30°) for the seven VLBI stations investigated in the previous section. Time series were created for the timespans from 2008 up to 2017 and 2019 up to 2023, to avoid the discontinuity in the VMF1 time series caused by the change in calculation made in 2018. From them, time series of the difference between the mapping functions were then calculated, together with their overall mean differences. Tables of the mean differences (VMF3 minus VMF1) at the three elevation angles are provided in tables 5.17 and 5.18 for the hydrostatic, and in tables 5.19 and 5.20 for the wet mapping functions.

What is directly visible from these tables is that means of the differences between the wet mapping functions are dwarfed by their standard deviations. This is not the case for the hydrostatic mapping functions. Here the average of the differences is of about the same size as their variability. To visualize this, figure 5.20 contains plots of the differences for the station WETTZELL. From there, it is also visible that the difference between the hydrostatic VMF1 and VMF3 has a seasonal component. If any seasonal influence on the difference between the wet VMF1 and VMF3 exists, it is buried under an orders of magnitude larger noise-like variation.[2]

How the bias on estimated station heights is caused by inconsistent application is not obviously clear from these data. The difference between the hydrostatic VMF3 and VMF1 is positive for some stations, and negative for others. The portion of stations for which the difference is positive tends to increase when the calculation is made for a higher elevation angle. While most VLBI observations are at higher elevation angles (Landskron (2017) provides an average elevation angle of 37.2° for 1999 until 2014), observations at low elevation angles are most important for separating station heights and zenith wet delays, and a rule of thumb as mentioned in section 3.3.2 relates station height errors and mapping function errors at the lowest elevations observed (Böhm, 2004).

To obtain a more complete picture, values of the Vienna Mapping Functions for different elevation angles were calculated for the years 2014 and 2020 for all VLBI stations for which

[2]For some stations a yearly period in the difference between the wet mapping functions can be inferred from the time series' autocorrelation function.

	5°	10°	30°
FORTLEZA	$-3.35 \cdot 10^{-3}$ $(0.69 \cdot 10^{-3})$	$-0.17 \cdot 10^{-3}$ $(0.12 \cdot 10^{-3})$	$0.01 \cdot 10^{-3}$ $(0.04 \cdot 10^{-4})$
KOKEE	$-4.59 \cdot 10^{-3}$ $(0.92 \cdot 10^{-3})$	$-0.40 \cdot 10^{-3}$ $(0.16 \cdot 10^{-3})$	$-0.00 \cdot 10^{-3}$ $(0.01 \cdot 10^{-3})$
NYALES20	$1.82 \cdot 10^{-3}$ $(1.77 \cdot 10^{-3})$	$0.75 \cdot 10^{-3}$ $(0.27 \cdot 10^{-3})$	$0.04 \cdot 10^{-3}$ $(0.01 \cdot 10^{-3})$
TSUKUB32	$-1.94 \cdot 10^{-3}$ $(1.47 \cdot 10^{-3})$	$0.04 \cdot 10^{-3}$ $(0.31 \cdot 10^{-3})$	$0.01 \cdot 10^{-3}$ $(0.01 \cdot 10^{-3})$
WESTFORD	$0.27 \cdot 10^{-3}$ $(1.31 \cdot 10^{-3})$	$0.49 \cdot 10^{-3}$ $(0.23 \cdot 10^{-3})$	$0.03 \cdot 10^{-3}$ $(0.01 \cdot 10^{-3})$
WETTZELL	$0.90 \cdot 10^{-3}$ $(1.32 \cdot 10^{-3})$	$0.70 \cdot 10^{-3}$ $(0.21 \cdot 10^{-3})$	$0.04 \cdot 10^{-3}$ $(0.01 \cdot 10^{-3})$
YARRA12M	$3.17 \cdot 10^{-3}$ $(1.39 \cdot 10^{-3})$	$0.93 \cdot 10^{-3}$ $(0.26 \cdot 10^{-3})$	$0.04 \cdot 10^{-3}$ $(0.01 \cdot 10^{-3})$

Table 5.17: Mean differences between the hydrostatic VMF3 and VMF1 at different elevation angles. Standard deviation of the differences in parentheses. For comparison, the absolute values of the mapping functions are approximately 10, 5.5 and 2 at these elevations. Calculated from the time series going from 2008 up to and including 2017, except for YARRA12M, for which only 2008 until 2014 were used, as the difference between the hydrostatic VMF1 and VMF3 has a discontinuity in 2015.

	5°	10°	30°
FORTLEZA	$-3.08 \cdot 10^{-3}$ $(0.70 \cdot 10^{-3})$	$-0.12 \cdot 10^{-3}$ $(0.13 \cdot 10^{-3})$	$0.01 \cdot 10^{-3}$ $(0.05 \cdot 10^{-4})$
KOKEE	$-5.72 \cdot 10^{-3}$ $(1.30 \cdot 10^{-3})$	$-0.59 \cdot 10^{-3}$ $(0.024 \cdot 10^{-3})$	$-0.01 \cdot 10^{-3}$ $(0.01 \cdot 10^{-3})$
NYALES20	$1.71 \cdot 10^{-3}$ $(2.14 \cdot 10^{-3})$	$0.73 \cdot 10^{-3}$ $(0.33 \cdot 10^{-3})$	$0.04 \cdot 10^{-3}$ $(0.01 \cdot 10^{-3})$
TSUKUB32	$-2.89 \cdot 10^{-3}$ $(1.32 \cdot 10^{-3})$	$-0.12 \cdot 10^{-3}$ $(0.28 \cdot 10^{-3})$	$0.01 \cdot 10^{-3}$ $(0.01 \cdot 10^{-3})$
WESTFORD	$1.62 \cdot 10^{-3}$ $(1.64 \cdot 10^{-3})$	$0.72 \cdot 10^{-3}$ $(0.29 \cdot 10^{-3})$	$0.04 \cdot 10^{-3}$ $(0.01 \cdot 10^{-3})$
WETTZELL	$-1.74 \cdot 10^{-3}$ $(1.73 \cdot 10^{-3})$	$0.26 \cdot 10^{-3}$ $(0.27 \cdot 10^{-3})$	$0.03 \cdot 10^{-3}$ $(0.01 \cdot 10^{-3})$
YARRA12M	$-3.65 \cdot 10^{-3}$ $(1.33 \cdot 10^{-3})$	$-0.22 \cdot 10^{-3}$ $(0.25 \cdot 10^{-3})$	$0.01 \cdot 10^{-3}$ $(0.01 \cdot 10^{-3})$

Table 5.18: Mean differences between the hydrostatic VMF3 and VMF1 at different elevation angles. Standard deviation of the differences in parentheses. For comparison, the absolute values of the mapping functions are approximately 10, 5.5 and 2 at these elevations. Calculated from the time series going from 2019 up to and including 2023.

	5°	10°	30°
FORTLEZA	$0.21 \cdot 10^{-3}(3.70 \cdot 10^{-2})$	$0.20 \cdot 10^{-3}$ $(5.45 \cdot 10^{-3})$	$0.01 \cdot 10^{-3}$ $(0.19 \cdot 10^{-3})$
KOKEE	$2.10 \cdot 10^{-3}$ $(5.05 \cdot 10^{-2})$	$0.38 \cdot 10^{-3}$ $(7.35 \cdot 10^{-3})$	$0.02 \cdot 10^{-3}$ $(0.25 \cdot 10^{-3})$
NYALES20	$14.35 \cdot 10^{-3}$ $(11.93 \cdot 10^{-2})$	$2.24 \cdot 10^{-3}$ $(17.30 \cdot 10^{-3})$	$0.08 \cdot 10^{-3}$ $(0.59 \cdot 10^{-3})$
TSUKUB32	$11.87 \cdot 10^{-3}$ $(11.12 \cdot 10^{-2})$	$1.62 \cdot 10^{-3}$ $(16.26 \cdot 10^{-3})$	$0.06 \cdot 10^{-3}$ $(0.56 \cdot 10^{-3})$
WESTFORD	$1.84 \cdot 10^{-3}$ $(3.81 \cdot 10^{-2})$	$0.49 \cdot 10^{-3}$ $(5.59 \cdot 10^{-3})$	$0.22 \cdot 10^{-3}$ $(0.19 \cdot 10^{-3})$
WETTZELL	$5.89 \cdot 10^{-3}$ $(9.66 \cdot 10^{-2})$	$1.03 \cdot 10^{-3}$ $(13.98 \cdot 10^{-3})$	$0.04 \cdot 10^{-3}$ $(0.48 \cdot 10^{-3})$
YARRA12M	$13.99 \cdot 10^{-3}$ $(8.87 \cdot 10^{-2})$	$2.07 \cdot 10^{-3}$ $(12.88 \cdot 10^{-3})$	$0.07 \cdot 10^{-3}$ $(0.44 \cdot 10^{-3})$

Table 5.19: Mean differences between the wet VMF3 and VMF1 at different elevation angles. Standard deviation of the differences in parentheses. For comparison, the absolute values of the mapping functions are approximately 11, 5.7 and 2 at these elevations. Calculated from the time series going from 2008 up to and including 2017.

	5°	10°	30°
FORTLEZA	$-5.34 \cdot 10^{-3}$ $(4.16 \cdot 10^{-2})$	$-0.62 \cdot 10^{-3}$ $(6.12 \cdot 10^{-3})$	$-0.02 \cdot 10^{-3}$ $(0.21 \cdot 10^{-3})$
KOKEE	$8.09 \cdot 10^{-3}$ $(6.01 \cdot 10^{-2})$	$1.23 \cdot 10^{-3}$ $(8.76 \cdot 10^{-3})$	$0.04 \cdot 10^{-3}$ $(0.30 \cdot 10^{-3})$
NYALES20	$-2.90 \cdot 10^{-3}$ $(13.54 \cdot 10^{-2})$	$-0.30 \cdot 10^{-3}$ $(19.68 \cdot 10^{-3})$	$-0.01 \cdot 10^{-3}$ $(0.68 \cdot 10^{-3})$
TSUKUB32	$10.42 \cdot 10^{-3}$ $(12.10 \cdot 10^{-2})$	$1.38 \cdot 10^{-3}$ $(17.73 \cdot 10^{-3})$	$0.05 \cdot 10^{-3}$ $(0.61 \cdot 10^{-3})$
WESTFORD	$0.05 \cdot 10^{-3}$ $(5.51 \cdot 10^{-2})$	$0.23 \cdot 10^{-3}$ $(8.11 \cdot 10^{-3})$	$0.01 \cdot 10^{-3}$ $(0.28 \cdot 10^{-3})$
WETTZELL	$1.77 \cdot 10^{-3}$ $(12.17 \cdot 10^{-2})$	$0.40 \cdot 10^{-3}$ $(17.69 \cdot 10^{-3})$	$0.02 \cdot 10^{-3}$ $(0.61 \cdot 10^{-3})$
YARRA12M	$3.45 \cdot 10^{-3}$ $(10.48 \cdot 10^{-2})$	$0.52 \cdot 10^{-3}$ $(15.30 \cdot 10^{-3})$	$0.02 \cdot 10^{-3}$ $(0.53 \cdot 10^{-3})$

Table 5.20: Mean differences between the wet VMF3 and VMF1 at different elevation angles. Standard deviation of the differences in parentheses. For comparison, the absolute values of the mapping functions are approximately 11, 5.7 and 2 at these elevations. Calculated from the time series going from 2019 up to and including 2023.

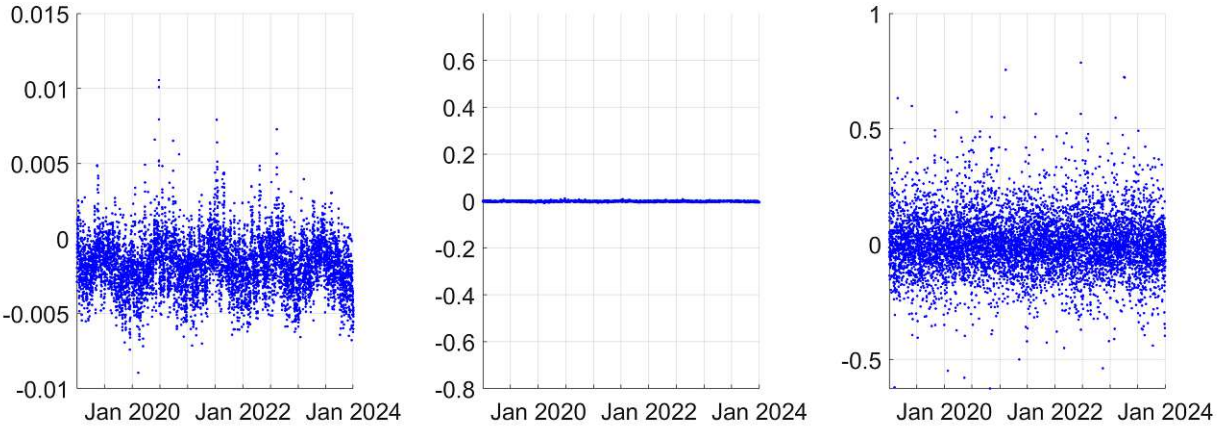

Figure 5.20: Time series of differences between the hydrostatic (left and middle) and wet (right) VMF3 and VMF1 at WETTZELL for an elevation angle of 5°. The middle graph has the same data as the left one, but with the same scaling as the rightmost one, to emphasize the difference between the orders of magnitude larger variability of the wet difference compared to the hydrostatic difference.

site-wise coefficients are provided on the VMF data server. Again, the values for VMF1 were subtracted from those for VMF3 and a yearly average difference over all epochs was calculated. These differences were then plotted onto world maps and are presented in figures 5.22 and 5.23, to see if any obvious geographical pattern in the differences exists, which does not seem to be the case. Plotting the hydrostatic difference for 2020 against latitude (figure 5.21), a possible dependence on latitude is seen, but it does not look strong compared to the overall variation and is hard to discern due to the uneven distribution of stations.[3] Scatter plots of the mean hydrostatic difference against the mean wet difference are shown in figure 5.24.

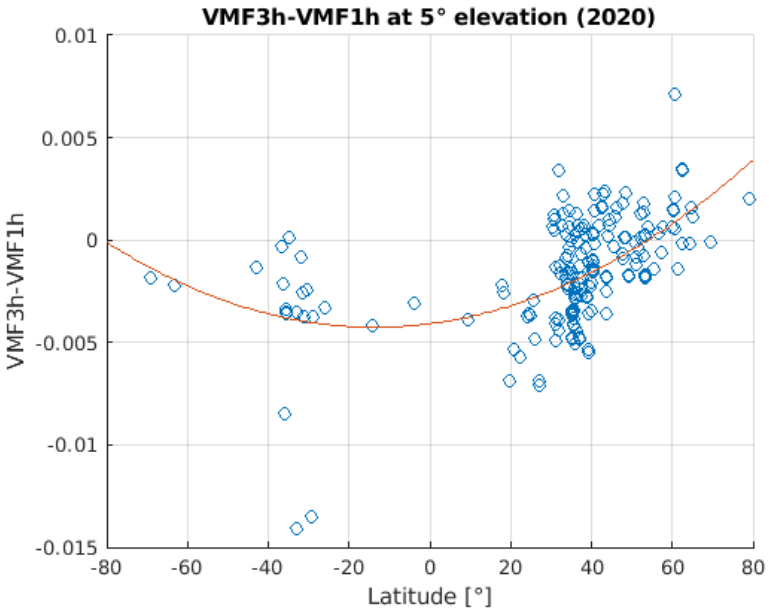

Figure 5.21: Mean difference between the hydrostatic VMF3 and VMF1 at 5° elevation depending on latitude. Best-fitting quadratic polynomial in red. Multiplying these numbers with 2000 mm and dividing by 5 would give a rough estimate of the accompanied station height error according to the rule of thumb. Calculated for 2020.

Again, the scatter plots in figure 5.24 confirm that for higher elevation angle, the value of the hydrostatic VMF3 minus VMF1 tends to be positive more often than at lower elevation angles, but with the absolute values of these differences shrinking about a hundredfold when going from 5° elevation to 30°. Assuming a difference of $0.5 \cdot 10^{-4}$ for the difference at 30° elevation and a modeled zenith hydrostatic delay of 2000 mm, this translates to a difference in the modeled slant hydrostatic delays of just a tenth of a millimeter, which is for all intents and purposes negligible. At 5° elevation, a difference of 0.005 would result in a difference of 10 mm in the slant hydrostatic delay. Concerning the wet mapping functions, the same

[3] The dependence of the hydrostatic difference on latitude becomes more visible when calculating a global grid of the difference at sea level from the grid-wise a_h coefficients.

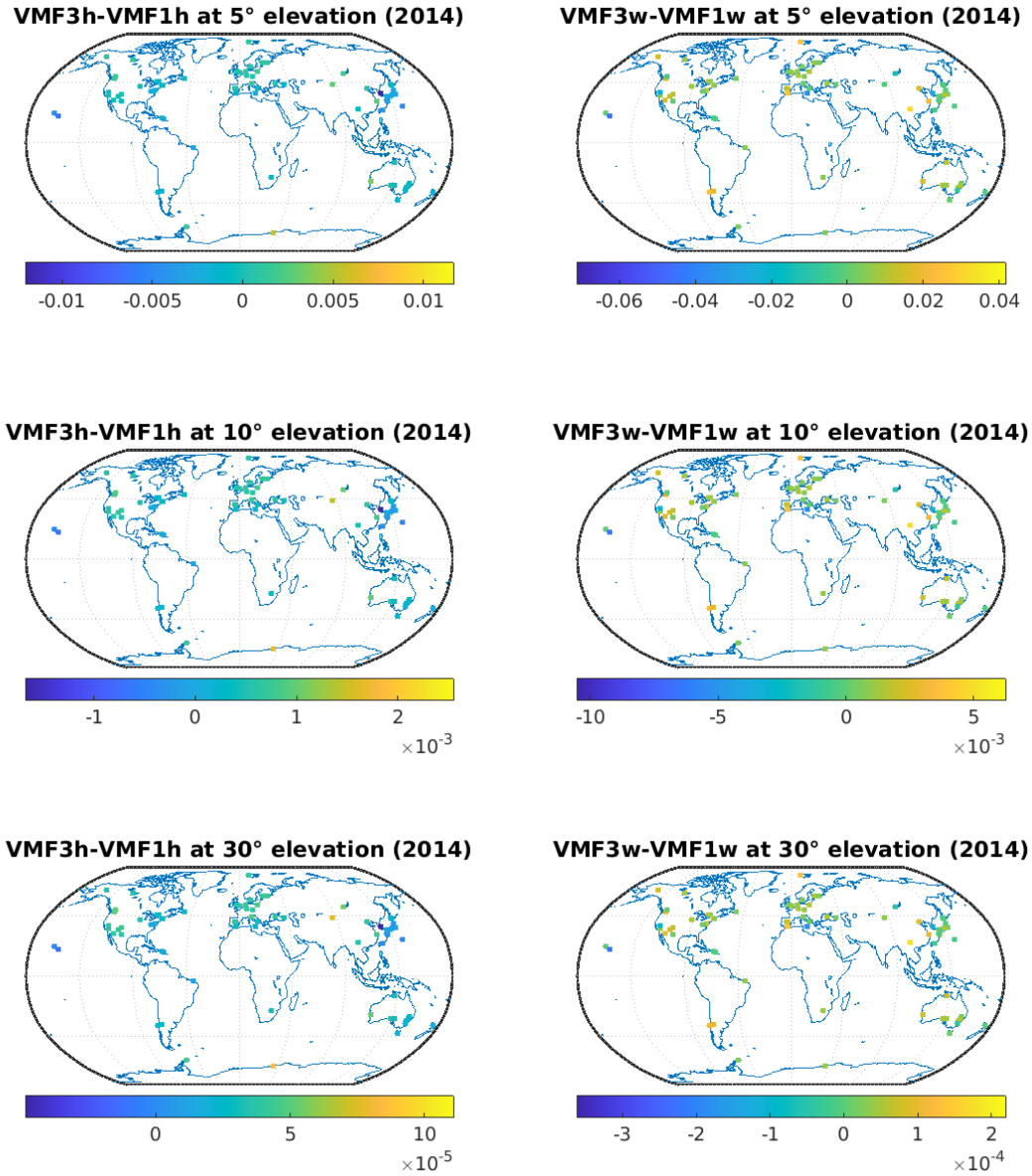

Figure 5.22: Maps of the mean difference between VMF1 and VMF3 for different VLBI stations in 2014. Left hydrostatic difference, right wet difference. From top to bottom: elevation angles of 5°, 10° and 30°.

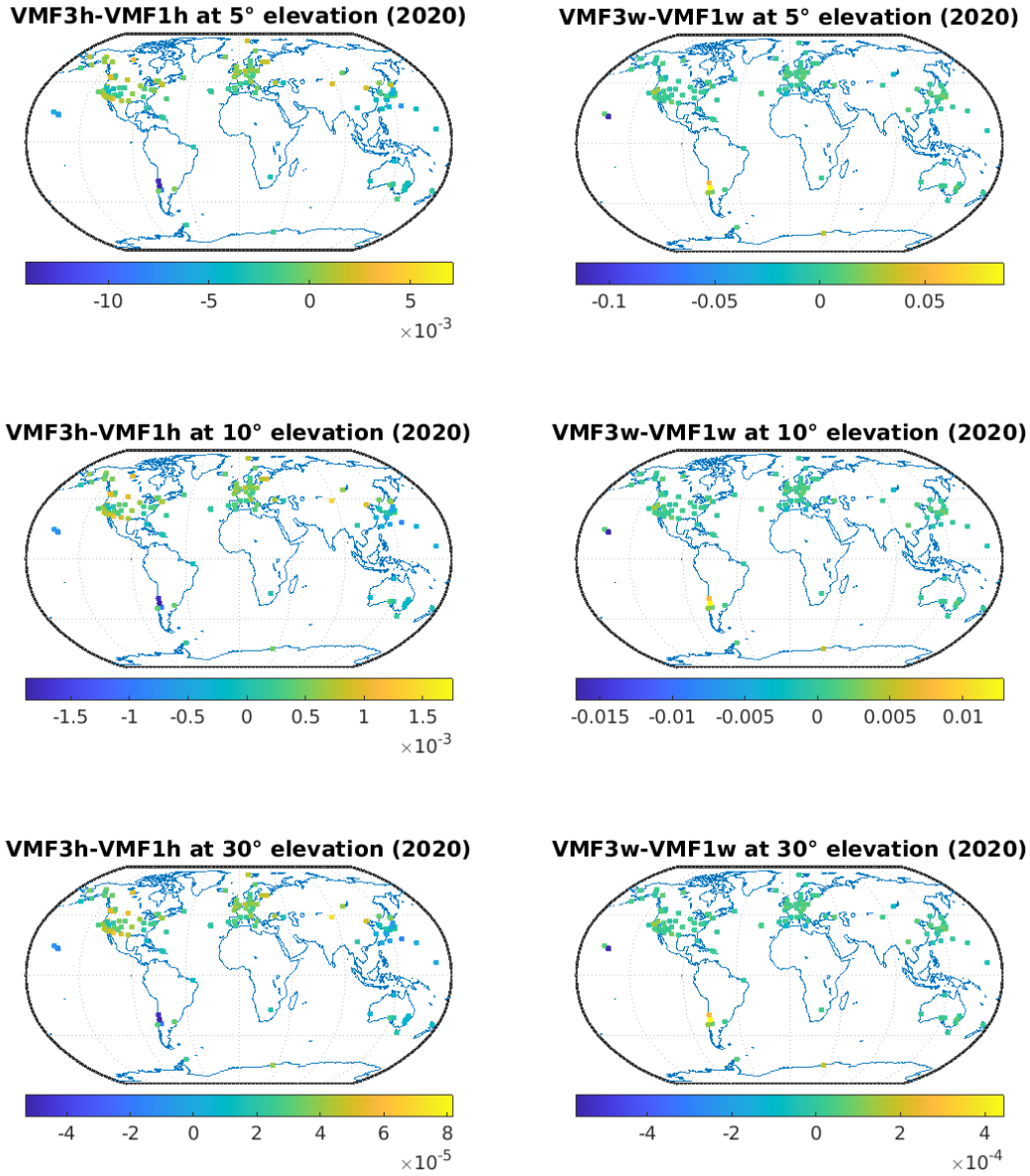

Figure 5.23: Maps of the mean difference between VMF1 and VMF3 for different VLBI stations in 2020. Left hydrostatic difference, right wet difference. From top to bottom: elevation angles of 5°, 10° and 30°.

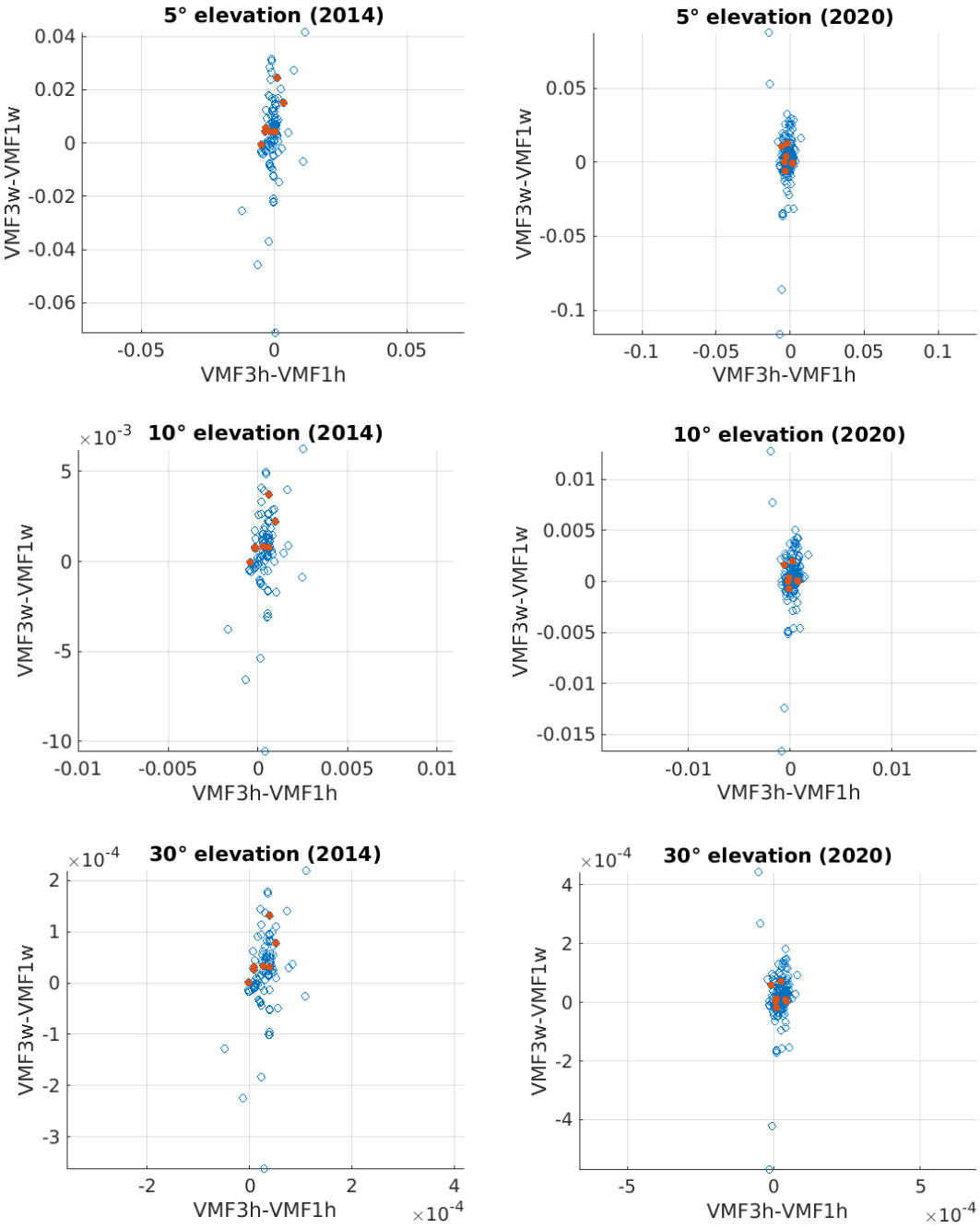

Figure 5.24: Scatterplots of the mean hydrostatic difference of VMF1 and VMF3 against the mean wet difference. Left for 2014, right for 2020. From top to bottom: elevation angles of 5°, 10° and 30°. The seven stations with tabulated values are marked in orange.

expected shrinking of the differences is seen in the plots, but the proportion of positive to negative differences is roughly equal for all three elevations, with the range of values also being spread out more than for the hydrostatic differences. Assuming a zenith wet delay of 100 mm, differences of 0.005 for an elevation of 5° and $0.5 \cdot 10^{-4}$ at 30° would translate to a difference in the slant delays of half a millimeter and a two-hundredth of a millimeter respectively.

Now relating the found station height differences to the differences of VMF3 w. r. t. VMF1 at an elevation of 5°, one would expect the hydrostatic and the wet difference to cancel out, in account of the consistent application of VMF3 introducing no station height bias w. r. t. the consistent application of VMF1, while using one for the wet and the other for the hydrostatic delay introduces this bias. In general, this canceling does not seem to exist. Taking WETTZELL as an example, it was found that for the timespan from 2008 to 2017, the mean difference of the hydrostatic VMFs was $0.90 \cdot 10^{-3}$, while the mean difference of the wet VMFs was $-1.74 \cdot 10^{-3}$. Assuming a mean zenith hydrostatic delay of 2000 mm and a mean zenith wet delay of 100 mm (closest round number to the values provided on the VMF server for this station), this results in a difference of the mean hydrostatic slant delays of 1.80 mm, and of the mean zenith wet delays of −0.17 mm. Added together, the slant delay difference at an elevation of 5° when using VMF3 instead of VMF1 would be 1.63 mm. A fifth of that, 0.33 mm, would be, according to the rule of thumb, the accompanied mean station height difference. The actual mean height difference obatined from the analysis of the legacy S/X sessions as provided in table 5.13 is 0.09 mm. When using VMF3 only for the hydrostatic delay, but keeping the VMF1 for the wet delay (this is the setup referred to as *VMF3/1*) the hydrostatic slant delay difference of 1.80 mm is the total slant delay difference, because the wet slant delays are equal. A fifth of 1.80 mm is 0.36 mm, but the mean estimated station height difference in table 5.13 is −1.59 mm. Applying the mapping functions the other way around, the slant delay difference is −0.17 mm, a fifth of that being −0.03 mm, while the height difference from table 5.13 is 1.67 mm.

For TSUKUB32, as a second example, the average difference between the hydrostatic VMF1 and VMF3 at 5° elevation was $-1.94 \cdot 10^{-3}$ from 2008 until 2017, while the average wet difference was $11.87 \cdot 10^{-3}$. Using 2000 mm for the average zenith hydrostatic delay and 150 mm for the average zenith wet delay (again closest round number to the values provided on the VMF server for this station), this leads to slant delay differences of −3.88 mm (hydrostatic) and 1.78 mm (wet). Added together these amount to a slant delay difference of −2.10 mm for VMF3 compared to VMF1. A fifth of that is −0.42 mm, with the height difference from table 5.13 being −0.68 mm. For the VMF3/1 setup, the average height difference was −2.89 mm, while a fifth of the hydrostatic delay difference is −0.78 mm. The height difference from the VMF1/3 setup is 2.20 mm, compared to the fifth of the wet delay difference, which is 0.36 mm.

With the amount of parameters estimated in the routine analysis performed at the Vienna

Analysis Center, and the correlations between them, an absorption of any effect caused by mapping function differences by many parameters is to be expected, making it harder to find a direct link between the average differences between VMF1 and VMF3 at a specific site and the average station height differences. However, it has been shown that this effect exists, and that the inconistent usage of the Vienna Mapping Functions as done at the Vienna Analysis Center introduces a bias regarding the estimated station height coordinates. The size of this bias of about one or two millimeters makes it hard to notice in the context of single session analysis, but it becomes clearly noticeable when looking at the results from many sessions simultaneously.

6 Comparison of estimation interval settings

The second comparison of settings in VieVS related to the troposphere deals with the estimation intervals. Again, the comparison mostly focuses on baseline length repeatabilities. It was originally planned to use the modeling settings where the Vienna Mapping Functions 3 are used for the hydrostatic delay and Vienna Mapping Functions 1 for the wet delay, but as it turned out that applying the two versions of the VMF in an inconsistent way introduces a bias on station heights, it was decided to use the VMF3 consistently for VLBI analysis at the Vienna Analysis Center. Therefore, the modeling settings used in this investigation apply VMF3 for the hydrostatic and wet delays. As laid out in chapter 4.3, tropospheric parameters are estimated as continuous piecewise linear offsets (CPWLOs), with defined estimation intervals and the option of setting constraints. The purpose of this test was to find out if the results of VLBI analysis can be improved by changing the estimation intervals of these offsets. Having intervals too long means that the estimated tropospheric parameters cannot follow the actual temporal variation of the troposphere, while shorter intervals mean an increased number of estimated parameters and a reduction in the over-determination of the adjustment.

6.1 Estimation interval setups

Three different estimation interval choices were investigated. The default settings as used for the vie2022a solution code are as follows (cf. figure 4.3):

- zenith wet delays: Estimated every 30 minutes, relative constraints of 1.5 cm between two offsets
- north and east gradients: Estimated every 180 minutes, relative constraints of 0.05 cm between two offsets, no absolute constraints

The other two setups are referred to as *zwd15grad90*, where all estimation intervals were divided by two (i. e. 15 minutes for zenith wet delays and 90 minutes for gradients), and *zwd60grad180*, which doubles the estimation intervals of the zenith wet delay but leaves the estimation intervals of the gradients unchanged. In each case, the applied relative constraints were scaled according to the scaling of the offset intervals.

For the calculation of baseline length repeatabilities, the list of ignored baselines and of estimates removed from the calculation is the same as described in section 5.1.

6.2 Comparing baseline length repeatabilites

Again, after the calculation of baseline length repeatabilites and weighted baseline length repeatabilites as described in chapter 5, these were plotted against baseline length together with a quadratic fit (figures 6.2 until 6.5). From these plots, it is already visible that the fit lines for the zwd60grad180 setup deviate for the legacy S/X sessions. This is because of a handful of baselines for which zwd60grad180 degrades the (W)BLRs massively. These data points lie outside of the plots to preserve their readability. How this degradation arises is not fully clear. One baseline for which it happens is HARTRAO–KOGANEI, where it is caused by a baseline length outlier for the session 18AUG01XN. When changing the estimation interval of the zenith wet delays from 30 minutes to 60 minutes, the estimated zenith wet delays at KOGANEI become negative for this session (about minus 400 centimeters, cf. figure 6.1), with station height increasing simultaneously. This does not seem to stem from an inability of the estimated ZWDs to follow a high temporal variation, but is nevertheless caused by changing the estimation interval setting.

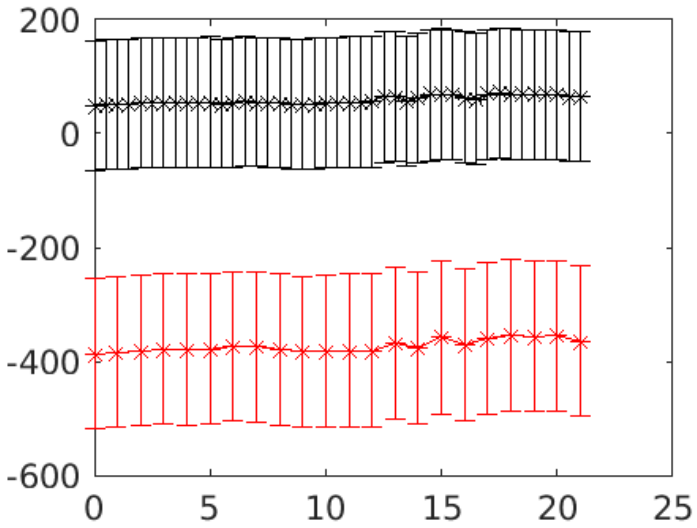

Figure 6.1: Estimated zenith wet delays at KOGANEI for session 01AUG18XN, in black with an estimation interval of 30 minutes, in red 60 minutes. X-axis in hours since session start, y-axis in centimeters.

In a first analysis, the number of baselines for which each setup provided the best BLR and weighted BLR was counted. These numbers are shown in tables 6.1 and 6.2. Like in chapter 5, these numbers do not have to add up to 948 and 24 respectively. As baseline length repeatabilities were calculated up to a tenth of a millimeter, baselines which performed best

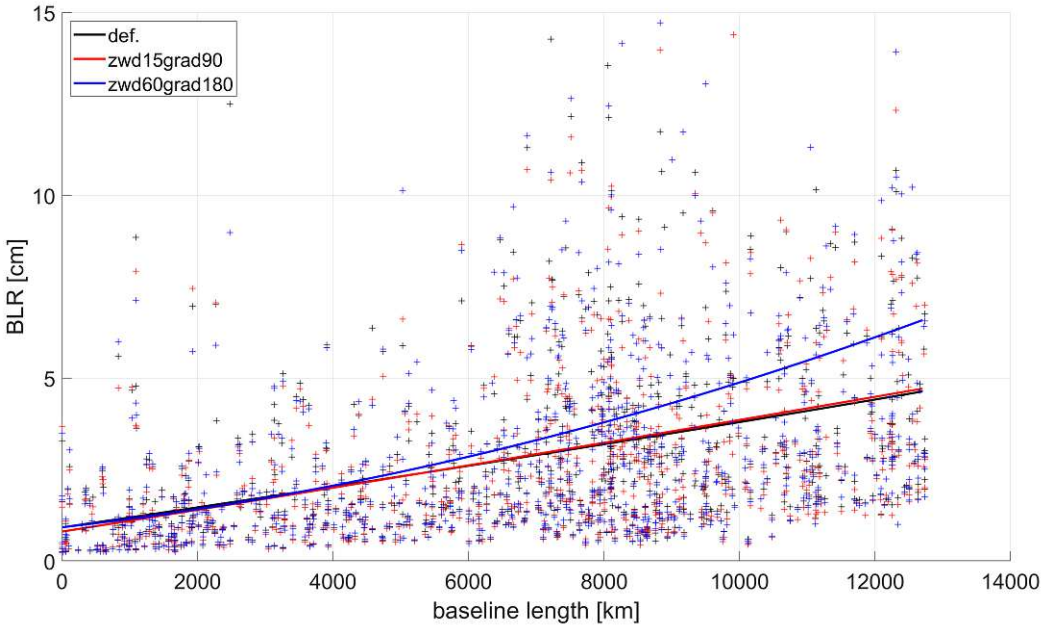

Figure 6.2: Plot of baseline length repeatabilities against baseline length from the session analyses with the three different estimation interval settings (legacy S/X sessions). The lines indicate the best-fitting quadratic polynomials.

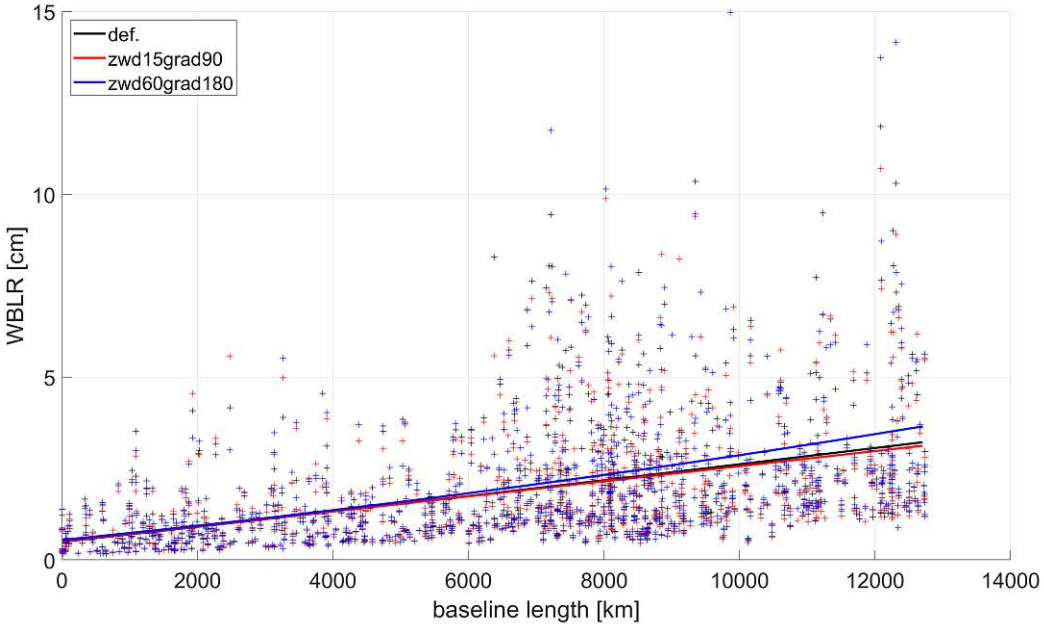

Figure 6.3: Plot of weighted baseline length repeatabilities against baseline length from the session analyses with the three different estimation interval settings (legacy S/X sessions). The lines indicate the best-fitting quadratic polynomials.

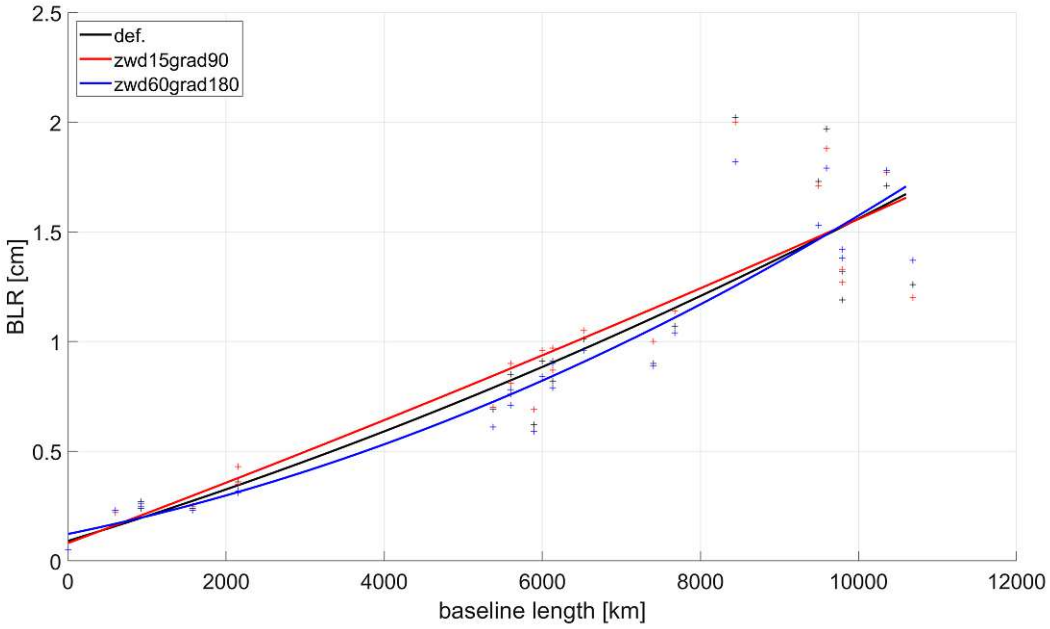

Figure 6.4: Plot of baseline length repeatabilities against baseline length from the session analyses with the three different estimation interval settings (VGOS sessions). The lines indicate the best-fitting quadratic polynomials.

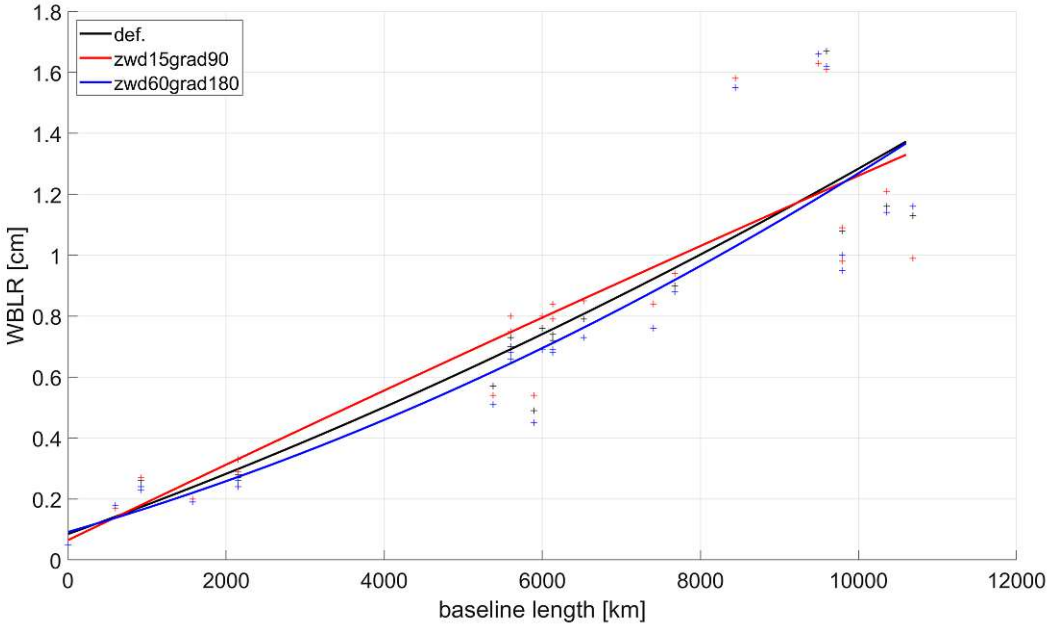

Figure 6.5: Plot of weighted baseline length repeatabilities against baseline length from the session analyses with the three different estimation interval settings (VGOS sessions). The lines indicate the best-fitting quadratic polynomials.

for more than one setup are counted multiple times.

As was done in the previous chapter, to avoid the possibility of attributing good performance to a setup that just spreads out the repeatabilities instead of improving them on average, the number of baselines for which each setup yielded the worst repeatability is also counted. These are provided in tables 6.3 and 6.4.

	default	zwd15grad90	zwd60grad180
S/X	231	487	269
VGOS	7	4	18

Table 6.1: Number of baselines for which each estimation interval setup provided the smallest repeatability.

	default	zwd15grad90	zwd60grad180
S/X	289	460	271
VGOS	4	5	20

Table 6.2: Number of baselines for which each estimation interval setup provided the smallest weighted repeatability.

	default	zwd15grad90	zwd60grad180
S/X	315	206	458
VGOS	5	15	7

Table 6.3: Number of baselines for which each estimation interval setup provided the largest repeatability.

	default	zwd15grad90	zwd60grad180
S/X	279	250	499
VGOS	7	19	4

Table 6.4: Number of baselines for which each estimation interval setup provided the largest weighted repeatability.

As in the previous chapter, differences of the repeatabilites w. r. t. default were calculated and tabulated in tables 6.5 and 6.6 for the average of the absolute differences, and in tables 6.7 and 6.8 for the relative differences expressed in percent. For the legacy S/X sessions, averages were additionally calculated as 2 % trimmed means, to remove baselines such as HARTRAO–KOGANEI where single sessions massively influence baseline length repeatability differences between the estimation interval settings.

From these obtained numbers, it appears that on average, baseline length repeatability is improved by shortening the estimation intervals for legacy S/X sessions. This improvement however is not large, only in the order of a few percent. Lengthening the estimation

	zwd15grad90	zwd60grad180
S/X	0.013 (1.453) [−0.066]	0.589 (7.430) [0.147]
VGOS	0.026 (0.046)	−0.024 (0.093)

Table 6.5: Average difference in baseline length repeatabilities from two of the setups w. r. t. the default setup. Values in centimeters, negative numbers indicate an improvement. Standard deviations in parentheses. 2 % trimmed means for S/X sessions in brackets.

	zwd15grad90	zwd60grad180
S/X	−0.031 (0.664) [−0.043]	0.146 (1.677) [0.056]
VGOS	0.020 (0.051)	−0.028 (0.028)

Table 6.6: Average difference in weighted baseline length repeatabilities from two of the setups w. r. t. the default setup. Values in centimeters, negative numbers indicate an improvement. Standard deviations in parentheses. 2 % trimmed means for S/X sessions in brackets.

	zwd15grad90	zwd60grad180
S/X	−0.83 % [−2.11 %]	11.50 % [5.38 %]
VGOS	4.23 %	−2.36 %

Table 6.7: Average relative difference in baseline length repeatabilities from two of the setups w. r. t. the default setup. Negative numbers indicate an improvement. 2 % trimmed means for S/X sessions in brackets.

	zwd15grad90	zwd60grad180
S/X	−0.61 % [−1.11 %]	6.11 % [2.36 %]
VGOS	3.80 %	−4.36 %

Table 6.8: Average relative difference in weighted baseline length repeatabilities from two of the setups w. r. t. the default setup. Negative numbers indicate an improvement. 2 % trimmed means for S/X sessions in brackets.

intervals of the zenith wet delays degrades repeatabilities, but partly does so by introducing large changes to the estimated station coordinates of single stations for single sessions. The mechanism behind this effect does not appear to come from high temporal variation in the troposphere that cannot be accounted for in the adjustment, but looks like an offset to station heights and zenith wet delays that is somehow introduced by changing the estimation interval. To answer how and why changing the estimation interval causes these offsets only at specific stations, and only for specific sessions, further research will be needed.

Regarding the VGOS sessions, the situation appears reversed. Here, baseline length repeatability is on average improved when using longer estimation intervals, and degraded when using shorter ones. This result might appear unintuitive, as the increased number of observations achievable with VGOS allows for the estimation of more parameters before over-estimation is reduced too far. A possible explanation could be an inhomogeneous sky coverage at some VGOS stations, which does not allow short intervals for gradient estimation without degrading results (Krásná, H., personal communication). As was already said in the previous chapter, the smaller number of VGOS sessions compared to the legacy S/X sessions makes these differences less reliable, and additional analyses with a higher number of VGOS sessions, and an increased number of VGOS stations in the future, will reveal if these are more than just a result of the small sample size.

7 Summary and Outlook

Investigating how the modeling and the parametrization of the troposphere affect the results of Very Long Baseline Interferometry analysis is an important task to ensure the quality of VLBI related data products. Taking the mapping functions as an example, the precision and accuracy of the model influences the precision and accuracy of the estimated parameters. For station coordinate precision specifically, this can be quantified by the baseline length repeatability, which has the advantage of being independent of rotations. For the investigation, 3296 legacy S/X sessions and 36 VGOS sessions were analyzed, with length repeatabilities calculated for 948 S/X baselines and 24 VGOS baselines. Here, it was revealed that regarding the two discrete mapping functions developed at TU Wien, VMF1 and VMF3, the choice between these two does not affect repeatabilities much, while the empirical model GPT3 showed a slightly worse performance. For legacy S/X session, the largest average improvement w. r. t. to the default setting of using VMF3 for the hydrostatic and VMF1 for the wet delay component was only 0.22 %. Whether the 4 % improvement of BLRs with VMF1 observed for VGOS sessions is significant or a result of the small sample size will be revealed by future analyses.

It was however also shown that the approach used for routine VLBI analysis at the Vienna Analysis Center (solution code 2022a), where VMF3 was used to model the hydrostatic delay, and VMF1 for the wet delay, leads to a biased estimation of station heights compared to the consistent application of either VMF1 or VMF3 for both delay components. Between the consistent use of VMF1 and the consistent use of VMF3, no bias in estimated station heights was observed. This result underlines the fact that a model must not only be assessed regarding the precision of the estimated parameters, but also regarding any parameter biases it might introduce. Furthermore, the reason for the different scale parameter of the Vienna Analysis Center's ITRF2020 contribution w. r. t. the contributions of other VLBI analysis centers has been found to be this peculiar setup of modeling the tropospheric delay. For further analyses at the Vienna Analysis Center (solution codes 2022b and onwards), VMF3 is used consistently for both the hydrostatic and wet tropospheric delay components. Relating the observed station height biases to the differences between VMF1 and VMF3 is not as straightforward as the rule of thumb relating height errors to delay errors at 5° elevation would suggest, possibly due to correlations with other estimated parameters.

For the estimation intervals of the zenith wet delays and the gradients, the setting of 30 minutes with a constraint of 1.5 cm (ZWDs) and 180 minutes with constraints of 0.05 cm (gradients) remained unchanged at the Vienna Analysis Center, also because the trend of

better performance with shorter intervals for S/X appears to be at odds with the trend of better performance with longer estimation intervals for VGOS sessions. A future investigation covering more VGOS sessions will probably shed light on whether this divergence is more than an artifact of the smaller sample size, and lead to a reevaluation of the optimal estimation interval for tropospheric parameters.

List of Figures

List of Tables

List of Abbreviations

BLR Baseline Length Repeatability

CPWLO Continuous Piecewise Linear Offset

EGR East Gradient

EOP Earth Orientation Parameters

GNSS Global Navigation Satellite Systems

GPT3 Global Pressure and Temperature 3

ITRF International Terrestrial Reference Frame

MJD Modified Julian Date

NGR North Gradient

NWM Numerical Weather Model

SNR Signal-to-Noise Ratio

VieVS Vienna VLBI and Satellite Software

VGOS VLBI Global Observing System

VLBI Very Long Baseline Interferometry

UT Universal Time

VMF1 Vienna Mapping Functions 1

VMF3 Vienna Mapping Functions 3

WBLR Weighted Baseline Length Repeatability

ZWD Zenith Wet Delay

A Baselines removed in preprocessing

A.1 List of single baseline length estimates removed from the calculation of BLRs

Chronological list of sessions for which all or some of the estimated baseline lengths were considered to be outliers as described in 5.1 and not used in the calculation of baseline length repeatabilities.

- 00MAY31XC
  - all baselines
- 02FEB04XB
  - FORTLEZA–HOBART26
  - FORTLEZA–KOKEE
  - FORTLEZA–OHIGGINS
  - HARTRAO–KOKEE
- 02MAR19XN
  - DSS45–KOKEE
  - HOBART26–KOKEE
  - KOKEE–PARKES
- JUN05XC
  - all baselines including HARTRAO
- 02OCT15XH
  - CRIMEA–HOBART26
- 03OCT27XC
  - HARTRAO–MEDICINA
- 04JAN13XH
  - HARTRAO–TIGOCONC
  - NOTO–TIGOCONC
- 04NOV09XA
  - FORTLEZA–TIGOCONC
  - HOBART26–TIGOCONC
- 05JAN26XA
  - FORTLEZA–HARTRAO
  - FORTLEZA–SYOWA
- 05JAN31XA
  - all baselines
- 06FEB14XV
  - all baselines
- 06FEB16XV
  - all baselines
- 06FEB23XV
  - all baselines
- 06NOV07XA
  - HARTRAO–SYOWA
- 08JAN23XA
  - all baselines including NYALES20
- 09JUN04XE
  - all baselines including BADARY
- 10FEB02XH
  - all baselines including OHIGGINS
- 10FEB17XA
  - MEDICINA–TIGOCONC
  - NYALES20–TIGOCONC
- 10NOV08XA
  - all baselines including HOBART12
- 10DEC09XE
  - all baselines including MEDICINA
- 11JAN13XE
  - TIGOCONC–YEBES40M
- 11AUG11XE
  - all baselines including YARRA12M
- 11AUG29XA
  - ONSALA60–WARK12M
- 12FEBV09XE
  - FORTLEZA–HOBART12
  - HOBART12–MATERA
  - MATERA–WARK12M
- 12MAR29XE
  - HOBART12–MATERA
  - HOBART12–WETTZELL
  - HOBART12–ZELENCHK
- 12JUN05XA
  - FORTLEZA–TSUKUB32
- 13MAY21XA
  - KATH12M–NYALES20
  - KATH12M–WETTZELL

- 13JUN25XH
  - ONSALA60–VERAMZSW
- 13AUG19XN
  - HARTRAO–KOKEE
- 13NOV19XH
  - FORTLEZA–ONSALA60
  - CHICHI10–ONSALA60
  - HARTRAO–VERAISGK
  - KOGANEI–ONSALA60
  - KOKEE–ONSALA60
  - NYALES20–VERAISGK
  - URUMQI–VERAISGK
  - VERAISGK–WETTZELL
- 14OCT09XE
  - FORTLEZA–HOBART12
  - FORTLEZA–KATH12M
  - FORTLEZA–YARRA12M
- 15APR30XA
  - all baselines including SEJONG
- 15MAY10XA
  - PARKES–YARRA12M
- 15MAY14XE
  - HART15M–HOBART12
- 15JUN30XH
  - all baselines including CRIMEA
- 15SEP29XN
  - FORTLEZA–HARTRAO
- 15NOV10XH
  - HART15M–KASHIM34
  - ISHIOKA–KASHIM34
- 15NOV25XB
  - all baselines including HOBART26
- 16JUL12XA
  - all baselines including URUMQI
- 17FEB20XA
  - HARTRAO–MEDICINA
- 17APR05XN
  - all baselines including KOGANEI
- 17MAY16XN
  - HOBART26–NOTO
- 17AUG08XA
  - ISHIOKA–KASHIM34
  - ISHIOKA–WARK12M
  - KATH12M–KUNMING
  - KUNMING–WARK12M
  - SEJONG–WARK12M
  - SESHAN25–WARK12M
  - URUMQI–WARK12M
- 18FEB13XH
  - DSS13–METSAHOV
  - HART15M–OHIGGINS
  - KATH12M–OHIGGINS
- 18FEB14XB
  - all baselines inculding AGGO
- 18FEB20XA
  - all baselines including OV-VLBA
- 18FEB20XN
  - HART15M–KOKEE
- 18MAR07XA
  - HART15M–HOBART26
- 18MAR20XA
  - all baselines including URUMQI
- 18MAY08XA
  - all baselines including SEJONG
- 18MAY09XA
  - HART15M–HOBART26
- 18JUN06XA
  - HART15M–HOBART26
- 18JUN27XA
  - KOKEE–WESTFORD
- 18AUG01XN
  - HOBART26–KOGANEI
- 18SEP04XH
  - all baselines including OHIGGINS
  - all baselines including SEJONG
- 18SEP17XA
  - all baselines including SEJONG
- 18NOV13XH
  - HARTRAO–ZELENCHK
- 18NOV22XA
  - HOBART26–ISHIOKA
  - ISHIOKA–KATH12M
  - ISHIOKA–WARK12M
  - ISHIOKA–YARRA12M
  - KASHIM34–KATH12M
  - KASHIM34–WARK12M
  - KATH12M–KUNMING
  - KATH12M–TIANMA65
  - KATH12M–YARRA12M
  - KUNMING–WARK12M
  - TIANMA65–YARRA12M
  - TIANMA65–WARK12M
  - URUMQI–WARK12M
- 19MAR12XA
  - HART15M–HOBART26
- 19MAR20XA
  - ISHIOKA–WARK12M
  - KUNMING–WARK12M
  - URUMQI–WARK12M
- 19APR14XA
  - HART15M–HOBART26
- 19MAY21XH
  - all baselines including VERAMZSW

- 19JUN25XN
  - OHIGGINS–YARRA12M
- 19JUL16XN
  - HARTRAO–ISHIOKA
- 19AUG06XN
  - KATH12M–OHIGGINS
  - OHIGGINS–YARRA12M
- 19SEP24XH
  - KATH12M–OHIGGINS
- 19NOV28XN
  - HARTRAO–ZELENCHK
- 19DEC10XH
  - all baselines including KOGANEI
  - ONSALA60–SEJONG
  - SEJONG–WETTZ13N
- 19DEC11XN
  - HOBART26–KOGANEI
- 19DEC23XA
  - MATERA–SEJONG
  - SEJONG–WETTZ13N
- 20JAN20XN
  - HARTRAO–ZELENCHK
- 20JAN21XA
  - HOBART26–SEJONG
  - KOKEE–SEJONG
- 20FEB03XA
  - SEJONG–WARK12M
- 20FEB05XN
  - all baselines including OHIGGINS
- 20MAR02XA
  - NYALE13S–SEJONG
  - SEJONG–WETTZ13N
- 20MAR24XN
  - HARTRAO–ZELENCHK
  - YARRA12M–ZELENCHK
- 20APR15XN
  - all baselines
- 20MAY20XA
  - KOGANEI–URUMQI
  - KOGANEI–YARRA12M
- 20JUN30XN
  - HARTRAO–KUNMING
- 20JUL15XA
  - HART15M–HOBART26
- 20SEP07XN
  - HARTRAO–MATERA
  - KUNMING–YARRA12M
  - MATERA–YARRA12M
- 20OCT12XN
  - HOBART26–KUNMING
  - KUNMING–YARRA12M
  - URUMQI–YARRA12M
- 20OCT19XA
  - SEJONG–WETTZ13N
- 20DEC10XE
  - AGGO–KOKEE

A.2 List of baselines completely removed from the analysis

A number of baselines showed a general very high variability in their length estimate time series. For these baselines, calculated length repeatablities were not considered in the comparison of mapping function or estimation interval settings.

- ALGOPARK–TIGOCONC
- BADARY–OHIGGINS
- CTVASTJ–TIGOCONC
- DSS15–HOBART26
- FORTLEZA–GGAO7108
- FORTLEZA–SEJONG
- FORTLEZA–WARK12M
- GGAO7108–HARTRAO
- GGAO7108–TIGOCONC
- GILCREEK–TIGOCONC
- HART15M–KATH12M
- HART15M–VERAMZSW
- HART15M–WARK12M
- HART15M–YARRA12M
- HARTRAO–HOBART12
- HARTRAO–HOBART26
- HARTRAO–KASHIM34
- HARTRAO–PARKES
- HARTRAO–KATH12M
- HARTRAO–WARK12M
- HARTRAO–YARRA12M
- HOBART12–KATH12M
- HOBART12–NOTO
- HOBART12–WARK12M
- HOBART12–YARRA12M
- HOBART26–KATH12M
- HOBART26–TIANMA65

- HOBART26–WARK12M
- HOBART26–YARRA12M
- ISHIOKA–OHIGGINS
- KASHIM11–OHIGGINS
- KASHIM34–OHIGGINS
- KATH12M–PARKES
- KATH12M–WARK12M
- KATH12M–YARRA12M
- KOKEE–NOTO
- KOKEE–OHIGGINS
- KOKEE–SYOWA
- MEDICINA–TIGOCONC
- NOTO–OHIGGINS
- NYALES20–OHIGGINS
- NYALES20–WARK12M
- OHIGGINS–ONSALA60
- OHIGGINs–SEJONG
- OHIGGINS–SVETLOE
- OHIGGINS–VERAMZSW
- OHIGGINS–WETTZELL
- OHIGGINS–ZELENCHK
- SEJONG–YARRA12M
- SEJONG–ZELENCHK
- TIGOCONC–VERAISGK
- TIGOCONC–YLOW7296
- WARK12M–WETTZELL
- WARK12M–YARRA12M

B Additional plots

B.1 Differences in the estimated Up-offsets for selected stations

The differences in the estimated Up-offsets w. r. t. VMF1/1, as plotted in figure 5.16 for WETTZELL, are presented here for the other six investigated stations.

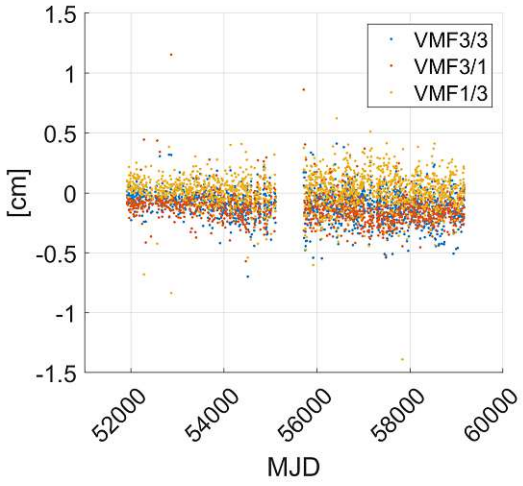

(a) FORTLEZA

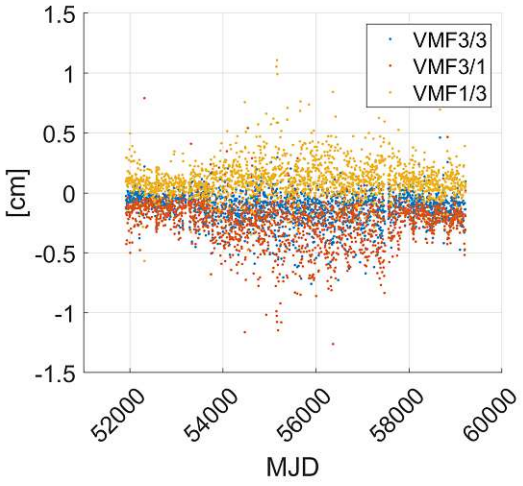

(b) KOKEE

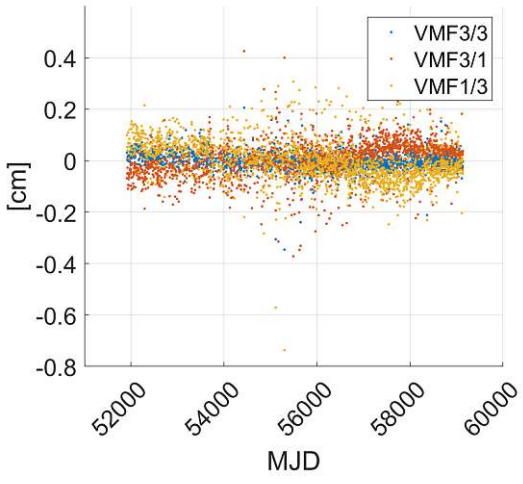

(c) NYALES20

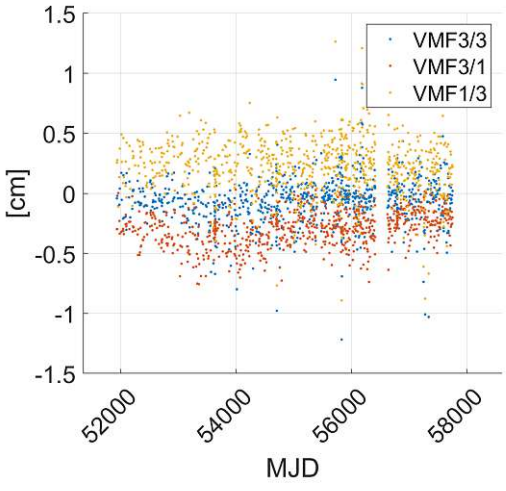

(d) TSUKUB32

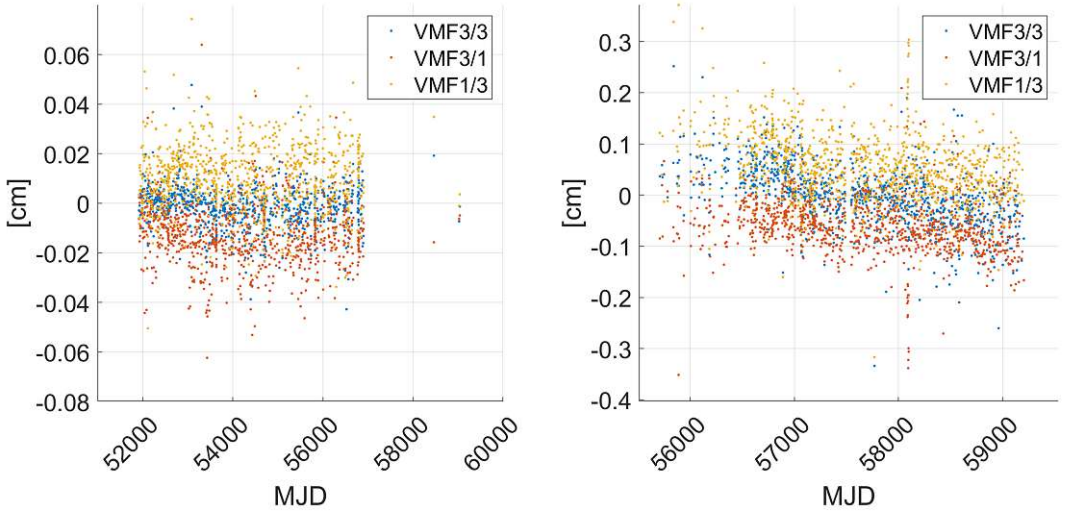

(e) WESTFORD (f) YARRA12M

Figure B.1: Differences in the estimated Up-offset from the analyses of legacy S/X sessions w. r. t. the analysis with the mapping function setup VMF1/1. In general, estimated station heights from the analyses with VMF1/1 and VMF3/3 are consistent, while they are lower when VMF3/1 is used, and higher when VMF1/3 is used. Peculiarly, for NYALES20 there exists a time span when this relationship is reversed, and estimated station heights are higher with VMF3/1 and lower with VMF1/3.

B.2 Differences in the estimated ZWDs for selected stations

The differences in the estimated zenith wet delays w. r. t. VMF1/1, as plotted in figure 5.17 for WETTZELL, are presented here for the other six investigated stations.

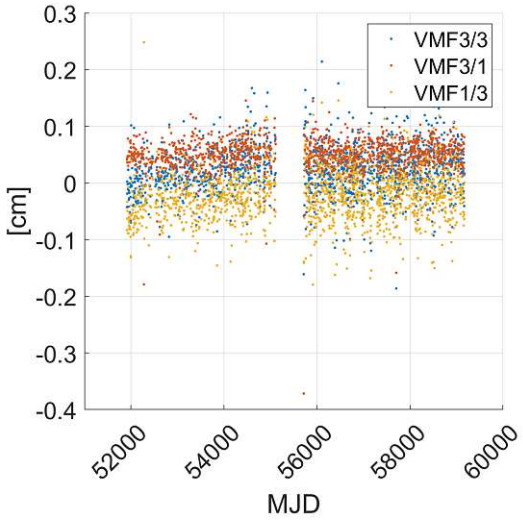

(a) FORTLEZA

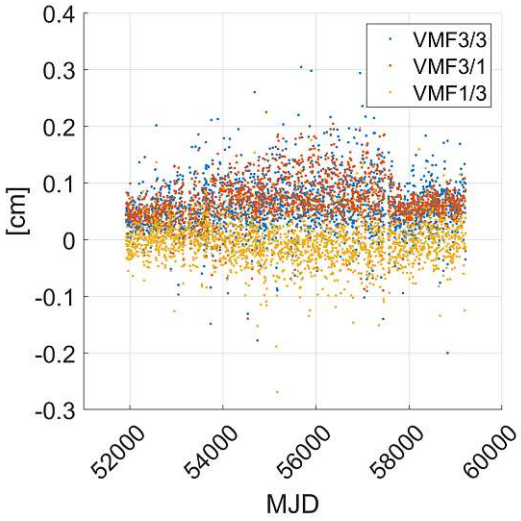

(b) KOKEE

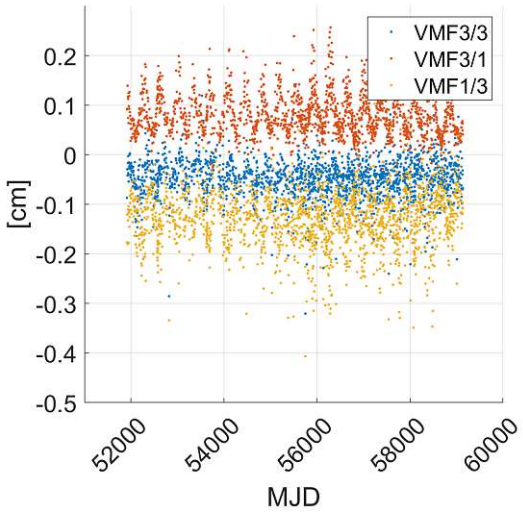

(c) NYALES20

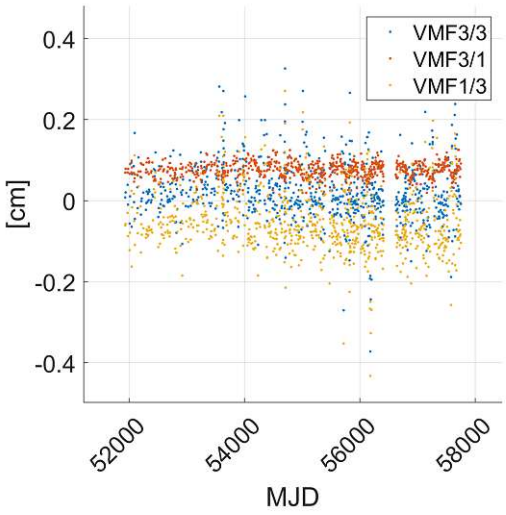

(d) TSUKUB32

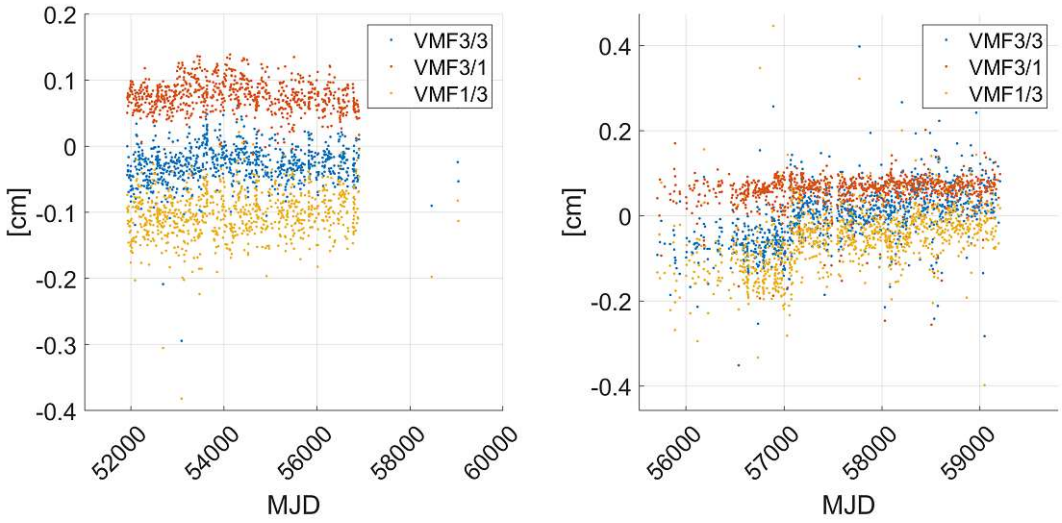

(e) WESTFORD (f) YARRA12M

Figure B.2: Differences in the estimated zenith wet delays from the analyses of legacy S/X sessions w. r. t. the analysis with the mapping function setup VMF1/1.

B.3 Differences in the estimated Up-offsets for selected stations (ZWDs not estimated)

The differences in the estimated Up-offsets when zenith wet delays are modeled and not estimated, as plotted in figure 5.18 for WETTZELL, are presented here for the other six investigated stations.

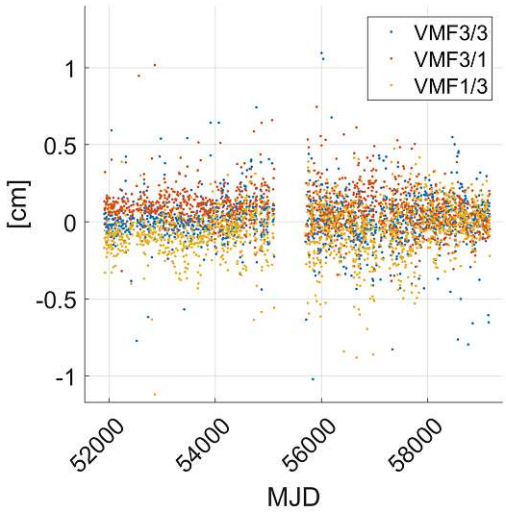

(a) FORTLEZA

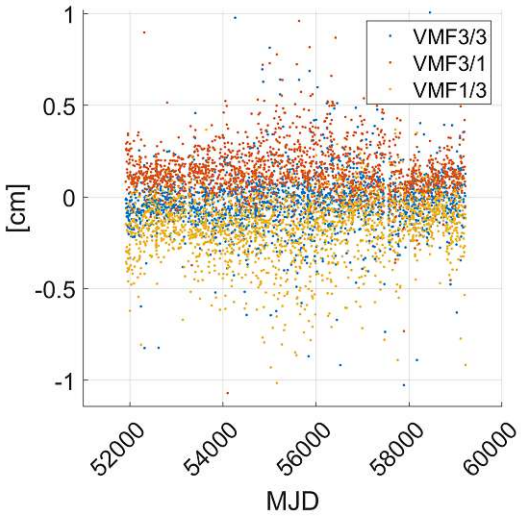

(b) KOKEE

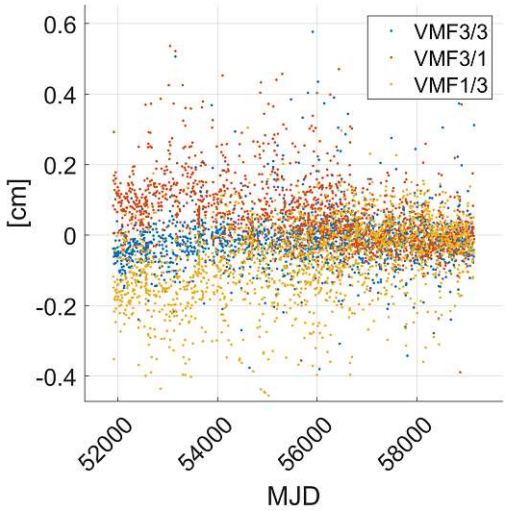

(c) NYALES20

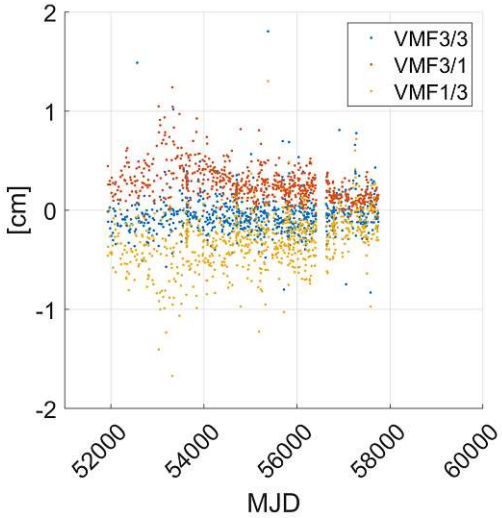

(d) TSUKUB32

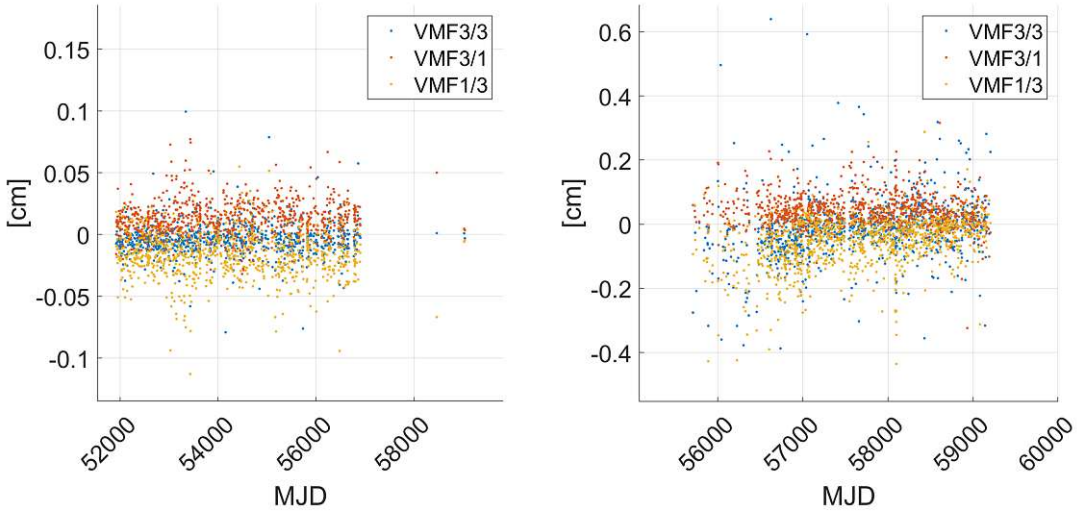

(e) WESTFORD (f) YARRA12M

Figure B.3: Differences in the estimated Up-offsets from the analyses of legacy S/X sessions w. r. t. the analysis with the mapping function setup VMF1/1. Zenith wet delays only modeled but not estimated. Compared to figure B.1 the differences from the analyses with inconsistent application of the mapping functions tend to flip sign.

B.4 Differences in the estimated ZWDs for selected stations (station coordinates not estimated)

The differences in the estimated zenith wet delays when station coordinates were fixed to their a priori values and not estimated, as plotted in figure 5.19 for WETTZELL, are presented here for the other six investigated stations.

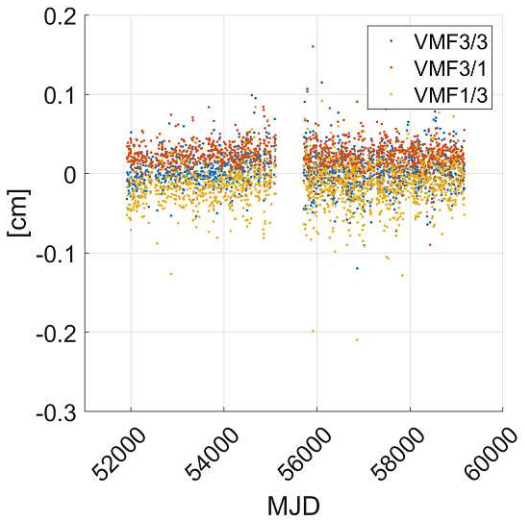

(a) FORTLEZA

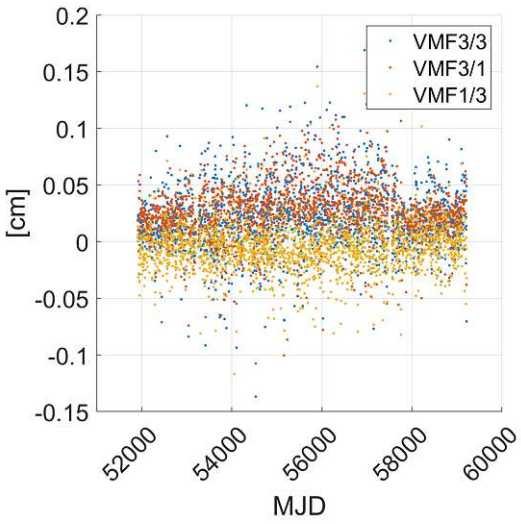

(b) KOKEE

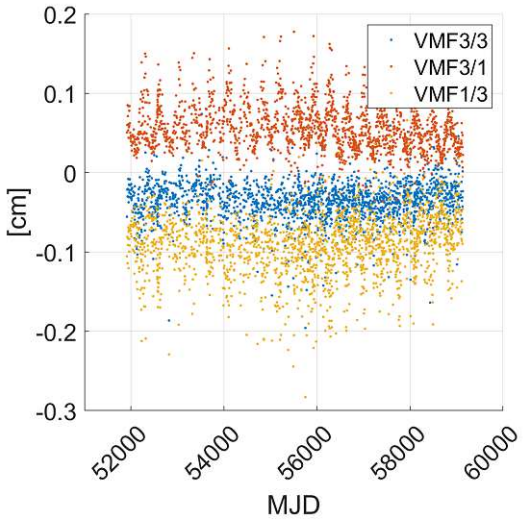

(c) NYALES20

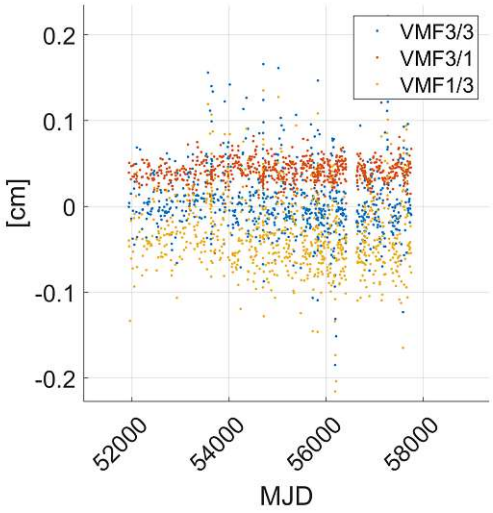

(d) TSUKUB32

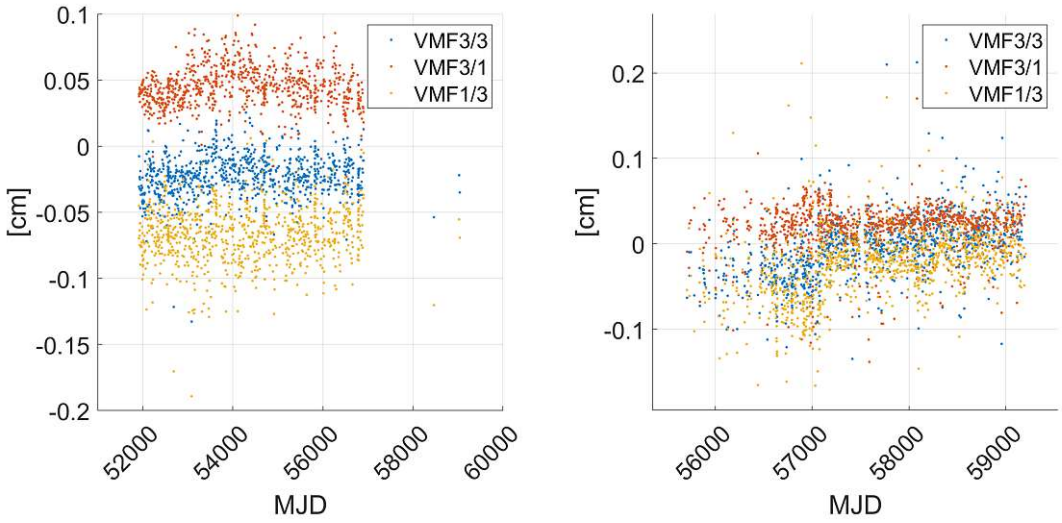

(e) WESTFORD (f) YARRA12M

Figure B.4: Differences in the estimated zenith wet delays from the analyses of legacy S/X sessions w. r. t. the analysis with the mapping function setup VMF1/1. Station coordinates not estimated but fixed to a priori values. Compared to figure B.2, the differences are of the same sign but tend to be smaller.

References

Askne, J., & Nordius, H. (1987). Estimation of tropospheric delay for microwaves from surface weather data. *Radio Science*, *22*(3), 379–386. https://doi.org/10.1029/RS022i003p00379

Böhm, J. (2004). *Troposphärische Laufzeitverzögerungen in der VLBI* [Doctoral dissertation, Technische Universität Wien]. https://repositum.tuwien.at/handle/20.500.12708/14250

Böhm, J., Böhm, S., Boisits, J., Girdiuk, A., Gruber, J., Hellerschmied, A., Krásná, H., Landskron, D., Madzak, M., Mayer, D., McCallum, J., McCallum, L., Schartner, M., & Teke, K. (2018). Vienna VLBI and Satellite Software (VieVS) for Geodesy and Astrometry. *Publications of the Astronomical Society of the Pacific*, *130*, 044503. https://doi.org/10.1088/1538-3873/aaa22b

Böhm, J., & Boisits, J. (2018). *VMF Data Server*. Retrieved November 14, 2023, from https://vmf.geo.tuwien.ac.at/index.html

Böhm, J., Heinkelmann, R., & Schuh, H. (2007). Short Note: A Global Model of Pressure and Temperature for Geodetic Applications. *Journal of Geodesy*, *81*, 679–683. https://doi.org/10.1007/s00190-007-0135-3

Böhm, J., Niell, A., Tregoning, P., & Schuh, H. (2006a). Global mapping function (gmf): A new empirical mapping function based on numerical weather model data. *Geophysical Research Letters*, *33*(7). https://doi.org/10.1029/2005GL025546

Böhm, J., & Schuh, H. (2004). Vienna mapping functions in VLBI analyses. *Geophysical Research Letters*, *31*(1). https://doi.org/10.1029/2003GL018984

Böhm, J., Werl, B., & Schuh, H. (2006b). Troposphere mapping functions for GPS and very long baseline interferometry from European Centre for Medium-Range Weather Forecasts operational analysis data. *Journal of Geophysical Research: Solid Earth*, *111*(B2). https://doi.org/10.1029/2005JB003629

Chen, G., & Herring, T. A. (1997). Effects of atmospheric azimuthal asymmetry on the analysis of space geodetic data. *Journal of Geophysical Research: Solid Earth*, *102*(B9), 20489–20502. https://doi.org/10.1029/97JB01739

Davis, J., Herring, T., Shapiro, I., & Elgered, G. (1986). Geodesy by Radio Interferometry: Effects of Atmospheric Modeling Errors on Estimates of Baseline Length. *Radio Science*, *20*, 1593–1607. https://doi.org/10.1029/RS020i006p01593

Deller, A. T., Brisken, W. F., Phillips, C. J., Morgan, J., Alef, W., Cappallo, R., Middelberg, E., Romney, J., Rottmann, H., Tingay, S. J., & Wayth, R. (2011). DiFX-2: A More Flexible,

Efficient, Robust, and Powerful Software Correlator. *Publications of the Astronomical Society of the Pacific*, *123*(901), 275–287. https://doi.org/10.1086/658907

Gruber, J. F. (2022). *The Vienna VLBI raw data simulator and correlator in the VGOS era* [Doctoral dissertation, Technische Universität Wien]. https://repositum.tuwien.at/handle/20.500.12708/20682

Hellmers, H., Modiri, S., Bachmann, S., Thaller, D., Bloßfeld, M., Seitz, M., & Gipson, J. (2022). Combined IVS Contribution to the ITRF2020. In J. T. Freymueller & L. Sánchez (Eds.), *Geodesy for a Sustainable Earth* (pp. 3–13). Springer International Publishing.

Hobiger, T., Ichikawa, R., Koyama, Y., & Kondo, T. (2008). Fast and accurate ray-tracing algorithms for real-time space geodetic applications using numerical weather models. *Journal of Geophysical Research: Atmospheres*, *113*(D20). https://doi.org/10.1029/2008JD010503

Hofmeister, A., & Böhm, J. (2017). Application of ray-traced tropospheric slant delays to geodetic VLBI analysis. *Journal of Geodesy*, *91*(8), 945–964. https://doi.org/10.1007/s00190-017-1000-7

Krásná, H., Baldreich, L., Böhm, J., Böhm, S., Gruber, J., Hellerschmied, A., Jaron, F., Kern, L., Mayer, D., Nothnagel, A., Panzenböck, O., & Wolf, H. (2023a). VLBI celestial and terrestrial reference frames VIE2022b. *Astronomy and Astrophysics*, *679*, A53. https://doi.org/10.1051/0004-6361/202245434

Krásná, H., Baldreich, L., Böhm, J., Böhm, S., Gruber, J., Hellerschmied, A., Jaron, F., Kern, L., Mayer, D., Nothnagel, A., Panzenböck, O., & Wolf, H. (2023b). *Vienna Analysis Center Report 2021–2022*. Retrieved December 2, 2023, from https://ivscc.gsfc.nasa.gov/publications/br2021+2022/acvie.pdf

Lagler, K., Schindelegger, M., Böhm, J., Krásná, H., & Nilsson, T. (2013). GPT2: Empirical slant delay model for radio space geodetic techniques. *Geophysical Research Letters*, *40*(6), 1069–1073. https://doi.org/10.1002/grl.50288

Landskron, D. (2017). *Modeling tropospheric delays for space geodetic techniques* [Doctoral dissertation, Technische Universität Wien]. https://repositum.tuwien.at/handle/20.500.12708/6797

Landskron, D., & Böhm, J. (2018a). Refined discrete and empirical horizontal gradients in VLBI analysis. *Journal of Geodesy*, *92*(12), 1387–1399. https://doi.org/10.1007/s00190-018-1127-1

Landskron, D., & Böhm, J. (2018b). VMF3/GPT3: refined discrete and empirical troposphere mapping functions. *Journal of Geodesy*, *92*(4), 349–360. https://doi.org/10.1007/s00190-017-1066-2

MacMillan, D. S. (1995). Atmospheric gradients from very long baseline interferometry observations. *Geophysical Research Letters*, *22*(9), 1041–1044. https://doi.org/10.1029/95GL00887

MacMillan, D. S., & Ma, C. (1997). Atmospheric gradients and the VLBI terrestrial and celestial reference frames. *Geophysical Research Letters*, *24*(4), 453–456. https://doi.org/10.1029/97GL00143

Marini, J. W. (1972). Correction of Satellite Tracking Data for an Arbitrary Tropospheric Profile. *Radio Science*, *7*(2), 223–231. https://doi.org/10.1029/RS007i002p00223

Mayer, D. (2018). *VLBI celestial reference frames and assessment with Gaia* [Doctoral dissertation, Technische Universität Wien]. https://repositum.tuwien.at/handle/20.500.12708/2002

Mikschi, M., Böhm, J., & Schartner, M. (2021). Unconstrained Estimation of VLBI Global Observing System Station Coordinates. *Advances in Geosciences*, *55*, 23–31. https://doi.org/10.5194/adgeo-55-23-2021

Niell, A. (1996). Global mapping functions for the atmosphere delay at radio wavelengths. *Journal of Geophysical Research: Solid Earth*, *101*(B2), 3227–3246. https://doi.org/10.1029/95JB03048

Niell, A. (2007). *Baseline Length Repeatability*. Retrieved January 30, 2024, from https://ivscc.gsfc.nasa.gov/publications/memos/ivs-2007-003v01.pdf

Niell, A., Whithney, A., Petrachenko, B., Schluter, W., Vandenberg, N., Hase, H., Koyama, Y., Ma, C., Schuh, H., & Tuccari, G. (2005). *VLBI2010: current and future requirements for geodetic VLBI systems* (tech. rep.). https://ivscc.gsfc.nasa.gov/publications/ar2005/spcl-vlbi2010.pdf

Nilsson, T., Böhm, J., Wijaya, D. D., Tresch, A., Nafisi, V., & Schuh, H. (2013). Path Delays in the Neutral Atmosphere. In J. Böhm & H. Schuh (Eds.), *Atmospheric Effects in Space Geodesy*. Springer.

Nothnagel, A. (2019). Very Long Baseline Interferometry. In W. Freeden & R. Rummel (Eds.), *Handbuch der Geodäsie: 6 Bände* (pp. 1–58). Springer Berlin Heidelberg. https://doi.org/10.1007/978-3-662-46900-2_110-1

Nothnagel, A. (2023). *Elements of Geodetic and Astrometric Very Long Baseline Interferometry*. Retrieved October 23, 2023, from https://www.vlbi.at/data/publications/Nothnagel_Elements_of_VLBI.pdf

Petit, G., & Luzum, B. (2010). IERS Conventions (2010).

Saastamoinen, J. (1972). Atmospheric Correction for the Troposphere and Stratosphere in Radio Ranging Satellites. In *The Use of Artificial Satellites for Geodesy* (pp. 247–251). American Geophysical Union (AGU). https://doi.org/10.1029/GM015p0247

Schartner, M., & Böhm, J. (2019). VieSched: A New VLBI Scheduling Software for Geodesy and Astrometry. *131*(1002), 1–12. https://doi.org/10.1088/1538-3873/ab1820

Schuh, H., & Böhm, J. (2013). Very Long Baseline Interferometry for Geodesy and Astrometry. In G. Xu (Ed.), *Sciences of Geodesy - II: Innovations and Future Developments*

(pp. 339–376). Springer Berlin Heidelberg. https://doi.org/10.1007/978-3-642-28000-9_7

Spicakova, H., Böhm, J., Böhm, S., Nilsson, T., Pany, A., Plank, L., Teke, K., & Schuh, H. (2010). Estimation of geodetic and geodynamical parameters with VieVS. *Proceedings of IVS General Meeting 2010*.

Subirana, J. S., Zornoza, J. J., & Hernández-Pajares, M. (2011). *Transformations between ECEF and ENU coordinates*. Retrieved February 8, 2024, from https://gssc.esa.int/navipedia/index.php/Transformations_between_ECEF_and_ENU_coordinates

Teke, K. (2011). *Sub-daily parameter estimation in VLBI data analysis* [Doctoral dissertation, Technische Universität Wien]. https://repositum.tuwien.at/handle/20.500.12708/982

Thayer, G. D. (1967). A Rapid and Accurate Ray Tracing Algorithm for a Horizontally Stratified Atmosphere. *Radio Science*, *2*(2), 249–252. https://doi.org/10.1002/rds196722249

Vandenberg, N. (1999). *sked: Interactive/Automatic Scheduling Program* (tech. rep.). NASA/Goddard Space Flight Center.

World Meteorological Organization. (1992). *International Meteorological Vocabulary* (2nd ed.).